FSC-ESD-217/89/450A

MARS ROVER RTG STUDY

Updated November 27, 1989

Principal Investigator & Author:

A. Schock

Contributors:

T. Hamrick
T. Or
V. Sankarankandath
M. Shirbacheh (JPL)
E. Skrabek

FAIRCHILD
SPACE COMPANY
GERMANTOWN, MARYLAND 20874-1181

ABSTRACT

The paper describes the design and analysis of Radioisotope Thermoelectric Generators (RTGs) for powering the Mars Rover vehicle, which is a critical element of the unmanned Mars Rover and Sample Return mission (MRSR). The RTG design study was conducted by Fairchild Space Company for the U.S. Department of Energy, in support of the Jet Propulsion Laboratory's MRSR project.

The paper briefly describes a reference mission scenario, an illustrative Rover design and activity pattern on Mars, and its power system requirements and environmental constraints, including the RTG cooling requirements during transit to Mars. It identifies the key RTG design problem, i.e. venting the helium generated by the fuel's alpha decay without intrusion of the Martian atmosphere into the RTG, and proposes a design approach for solving that problem. Using that approach, it describes and analyzes a variety of RTG designs, all based on the proven and safety-qualified General Purpose Heat Source module.

The first RTG option described is a very conservative baseline design, employing standard thermoelectric unicouples whose reliability and performance stability has been extensively demonstrated on previous space missions. The heat source of the 250-watt RTG consists of a stack of 18 separate modules that is supported at its ends but not along its length. The paper describes and analyzes the structure that holds the stack together during Earth launch and Mars operations, but allows it to come apart in case of an inadvertent reentry.

It then summarizes the baseline RTG's mass breakdown, and presents a detailed description of its thermal, thermoelectric, and electrical analyses. It examines the effect of different operating conditions (beginning versus end of mission, water-cooled versus radiation-cooled, summer day versus winter night) on the RTG's performance. Finally, the paper compares the RTGs' specific powers for different power levels (250W versus 125W), different thermoelectric element designs (standard versus short unicouples, versus multicouples) and different thermoelectric figures of merit ($0.00058K^{-1}$ to $0.00140K^{-1}$).

The results presented show the RTG performance achievable with current technology, and the performance improvements that would be achievable with various technology developments. It provides a basis for selecting the optimum strategy for meeting the Mars Rover design goals with minimal programmatic risk and cost.

CONTENTS

1.0 SCOPE AND OBJECTIVES OF STUDY

In December 1988 the U.S. Department of Energy's Office of Special Applications (DOE/OSA) asked Fairchild Space Company to investigate RTG (Radioisotope Thermoelectric Generator) design options for powering a Martian Rover vehicle. That vehicle is a critical part of the Mars Rover and Sample Return (MRSR) mission, which is under preliminary study by NASA's Jet Propulsion Laboratory (JPL) with the support of the Johnson Space Center (JSC). JPL is responsible for the overall MRSR study and, among other items, for the design of the Rover vehicle.

The MRSR mission also requires a lower-power RTG for its stationary lander. However, work on this was deferred in our study, because the basic solutions worked out for the more difficult Rover application will also be applicable to the less demanding stationary lander application.

The purpose of the DOE-sponsored Fairchild study is to support JPL and JSC by providing the mission planners with information about the RTG masses and sizes for a conservative baseline design and for various advanced options of differing technology readiness. The various RTG design characterizations must be accurate and consistent, to permit meaningful comparisons among the different design options.

One of the primary aims of the study is to quantify the performance improvements achievable if new technologies are successfully developed, to estimate the required time, effort, success probability, and programmatic risk in developing those new technologies, and thus to help identify the best strategy for meeting the MRSR system goals.

In addition, the Fairchild study is useful in specifying critical design and operational requirements for integrating the RTG with the Rover and the launch vehicle (particularly cooling during orbit transfer), and in identifying what additional information JPL and JSC will need to furnish before the RTG design can be finalized.

2.0 MISSION

2.1 BACKGROUND

The long-term goal of the National Aeronautics and Space Administration is to expand human presence beyond Earth and into the Solar System [1]. Mars, with its potential for eventual habitability, is targeted for human exploration and colonization. A manned mission to Mars must be preceded by robotic exploration of Mars, to bridge the gap between the knowledge gained by the 1976 Viking Mission and the knowledge required for a safe and effective human journey to Mars.

The Jet Propulsion Laboratory and Johnson Space Center are jointly studying such a mission, called Mars Rover Sample Return. That study is focused on understanding the system requirements and generating the first-order system design that meets these requirements [2,3]. The mission requires orbiters, landers and a Rover in Mars orbit and/or on the Mars surface.

RTGs have been selected as the primary power source for the surface elements of the MRSR system. They have a long and successful history of space flight, and their reliability and performance have been demonstrated in missions such as Pioneer, Viking, and Voyager [4]. The current-generation RTGs, however, are designed for space operation and must be modified for Mars surface operation.

2.2 MRSR OBJECTIVES AND SYSTEM ELEMENTS

The objective of the MRSR mission is to determine the geological, climatological and biological history of the planet Mars, and to characterize its near-surface materials. The mission will also provide information on the Mars environment, and test key technologies for human exploration of the planet. The mission objectives are achieved by making in-situ analyses and returning selected samples to Earth for extensive studies.

A spectrum of possible missions and system designs has been examined against the broad science requirements [5]. These missions, which varied in launch configuration, launch date, and the various elements that constitute the mission, have been narrowed down to a reference mission that consists of five system elements: an Imaging Orbiter (IO), Communications Orbiter (CO), Rover, Sample Return Orbiter (SRO) and Mars Ascent Vehicle (MAV). The reference MRSR mission scenario and possible mission time-line envisioned by the JPL project team are summarized in Figures 1 and 2, respectively. As shown, the five system elements under this scenario are launched in four separate launch segments.

The Imaging Orbiter is launched aboard a Titan IV/IUS in October-November 1996, with Mars arrival in August-October of 1997. It maps the surface of the planet within 39 degrees of the Martian equator for landing site selection and Rover Traverse Planning [6]. A total of ten 10 x 10 km sites are mapped for selection of the landing site, and an area of 20 x 20 km at that site is further mapped for Rover Traverse planning.

The Communication Orbiter provides the communication link between the Mars surface elements and Earth [6]. It is launched in November-December 1998 aboard a Titan IV/IUS, and is placed in a stationary orbit such that the region between 65.7^{o} south and north of the equator is covered continuously. The Rover-to-Earth link is available at least 95% of every Mars Sol.

The Rover element is launched aboard a Titan IV/Centaur in December 1998, with arrival at Mars in October 1999-January 2000. The Rover traverses the surface of Mars, performs in-situ analyses, deploys science packages, selects samples and returns them to the ascent vehicle for delivery to Earth. Right after arrival, the Rover also selects a landing site for the MAV. The Rover design and its requirements are described in more detail in the next section.

The Sample Return Orbiter (SRO) and Mars Ascent Vehicle (MAV) are launched together onboard a Titan IV/Centaur in December 1998-February 1999, with arrival on Mars in October 1999-February 2000. The SRO/MAV flight segment is aerocaptured into a circular orbit around Mars [7]. After site certification by the Rover, the MAV descends to the Mars surface, where it deploys a meterological-geophysical science package and collects contingency

samples from its local environment. The SRO remains in orbit awaiting the return of the MAV and Mars samples. The Rover transfers its collected samples to the MAV from time to time, until MAV's ascent from Mars surface around December 2000. After liftoff from Mars, the MAV docks with the SRO and transfers the collected samples to it. The Earth return vehicle is then separated from the SRO to bring the samples back for aerocapture into low-Earth orbit, where its Martian samples are picked up by the shuttle.

Figure 1. MRSR Reference Mission Scenario

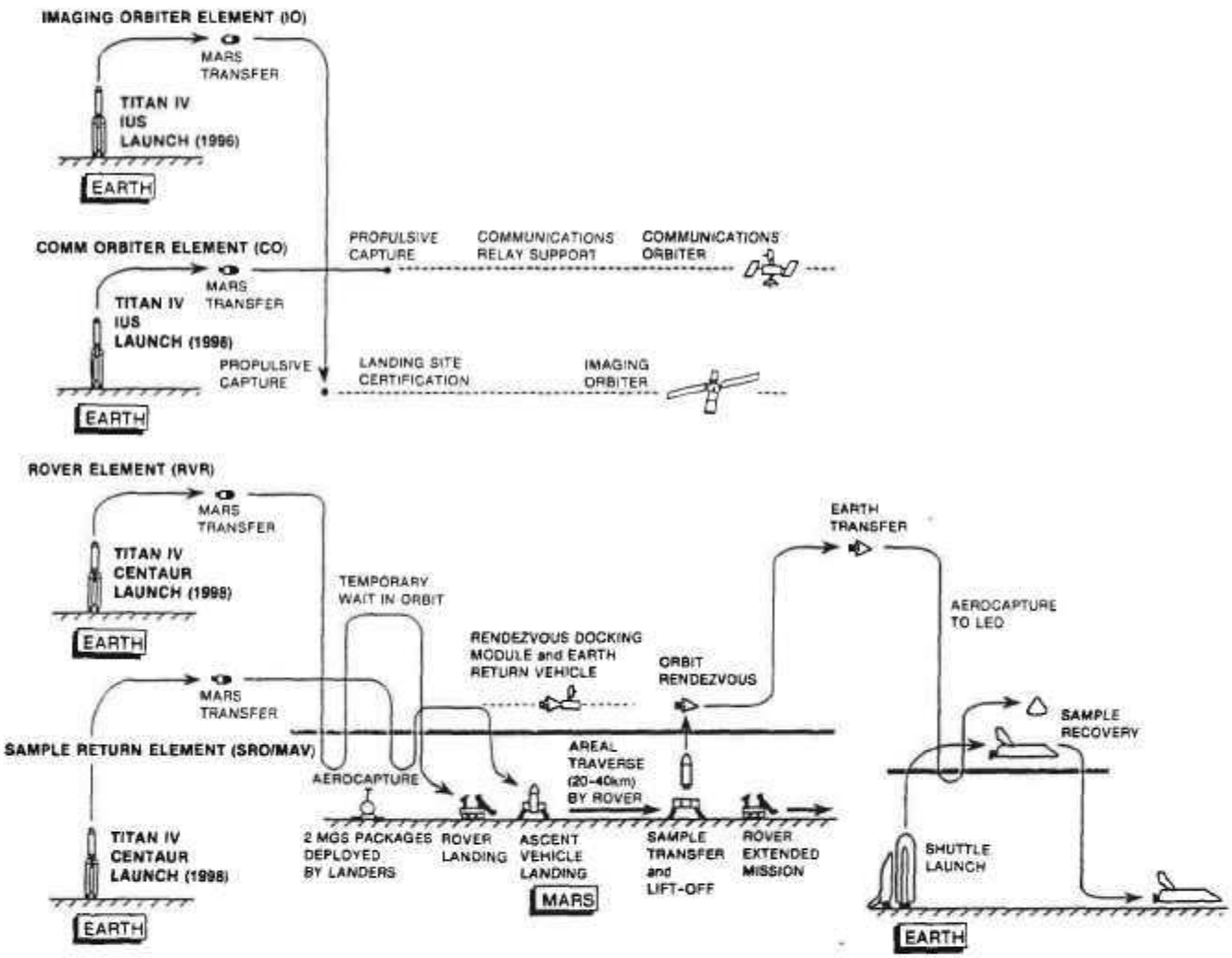

Figure 2. MRSR Reference Mission Timeline

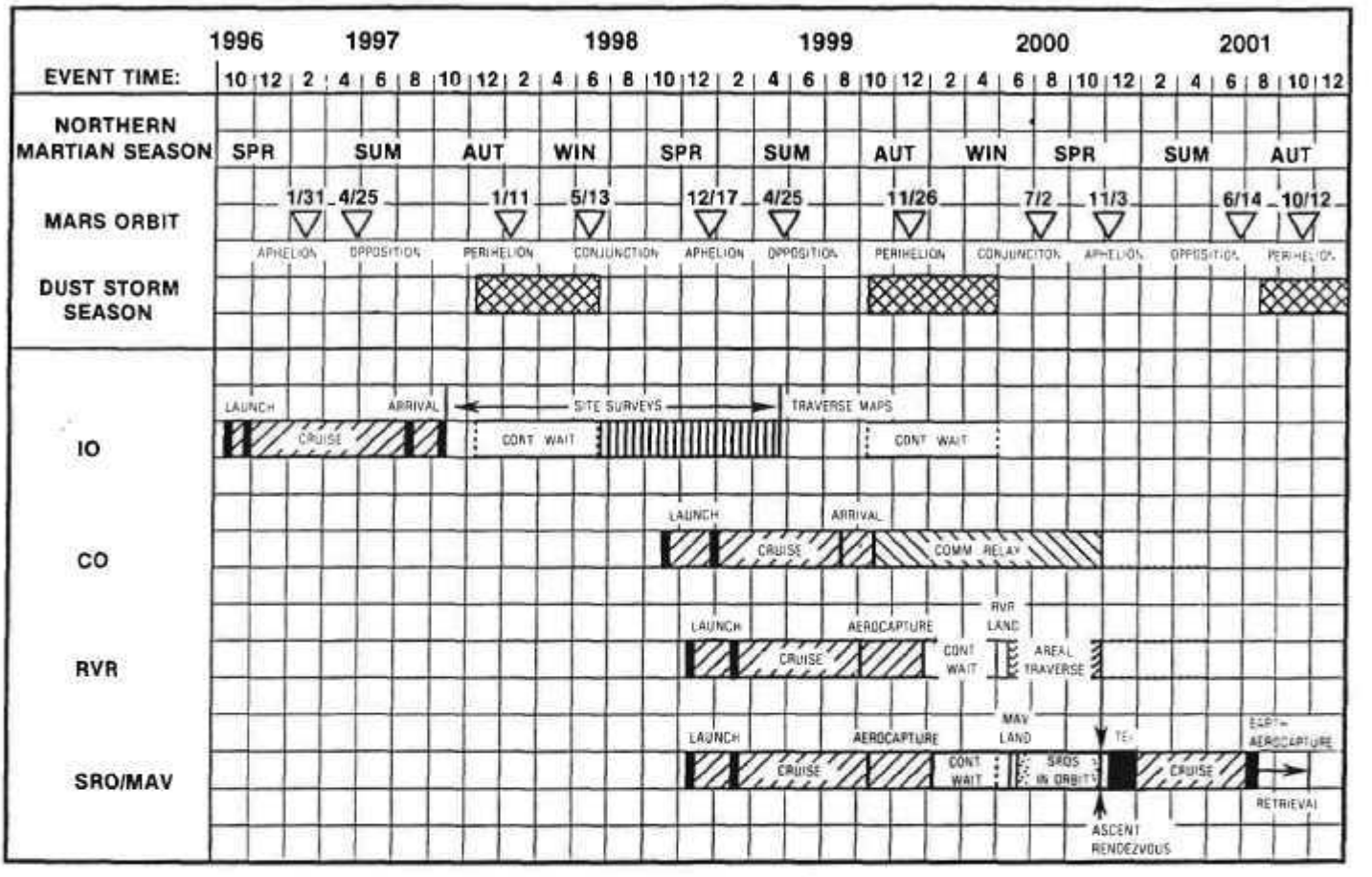

2.3 MARS ROVER

The Rover element of the Mars Rover Sample Return mission for which the RTG study was performed is required to traverse more than 40 kilometers and collect 100 samples from several geologically distinct sites [8]. The Rover is equipped with semi-autonomous navigation capability, which means it can compare its surroundings with a stored map of the orbital view obtained by the Imaging Orbiter, and plan and execute a local path toward a designated point. This autonomy greatly increases the Rover's range, since it reduces the need for frequent commands from Earth. Theoretically, the Rover can go several kilometers without requiring intervention from Earth.

The Rover will return with samples to the Mars Ascent Vehicle (MAV) several times. Each time the distance traveled expands as the confidence in the Rover is increased. A typical activity pattern as envisaged by JPL [9] is depicted in Figure 3.

Figure 3. Illustrative Rover Activity Pattern

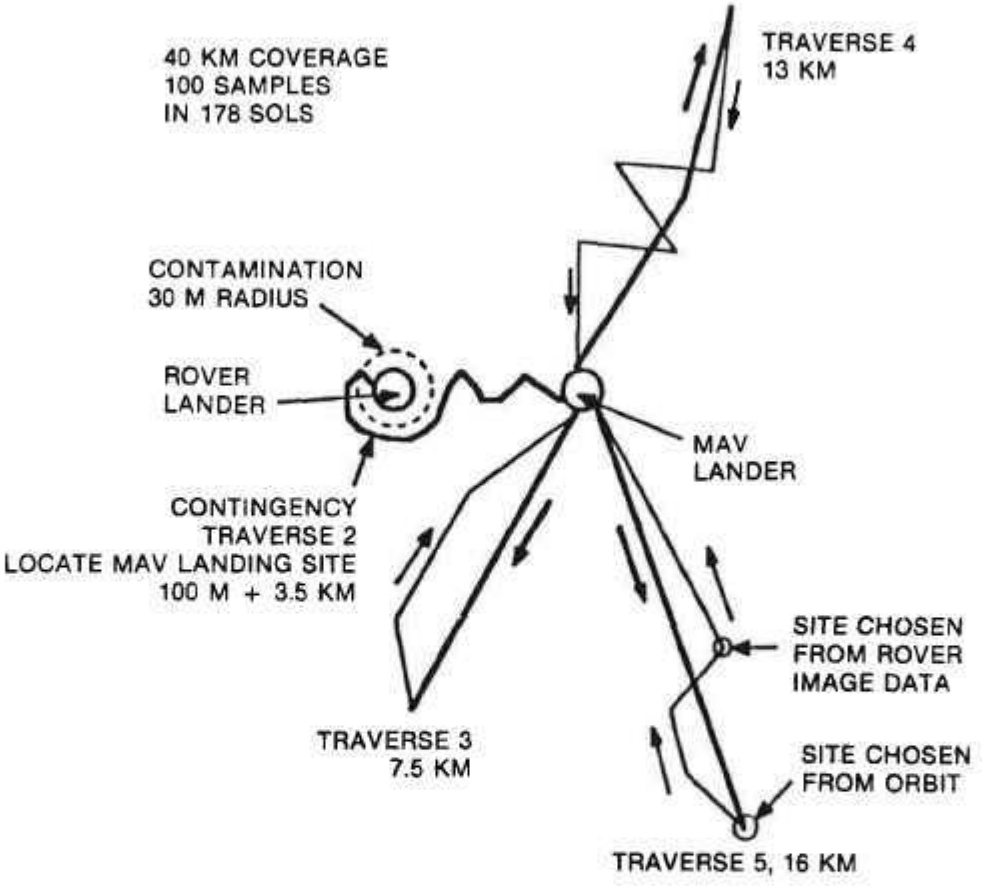

The Rover is equipped with an imaging camera, multispectral imaging for science and navigation, optical microscope, spectrometers (alpha, proton, neutron, and x-ray), electromagnetic sounders, gas analyzer, and differential scanning calorimeter. The sample acquisition by the Rover will be accomplished in several stages: remote sample characterization, location and designation of interesting samples, positioning and manipulation of the Rover to acquire the sample, and preserving the samples for return to the MAV.

Several different Rover designs and mobility systems are under investigation. One possible mobility system is illustrated in Figure 4. It employs a six-wheeled pantograph, with one-meter wheels that can move across rough terrain. This design was developed by a JPL in-house study.

Figure 4. Illustrative Wheeled-Vehicle Option Rover Design

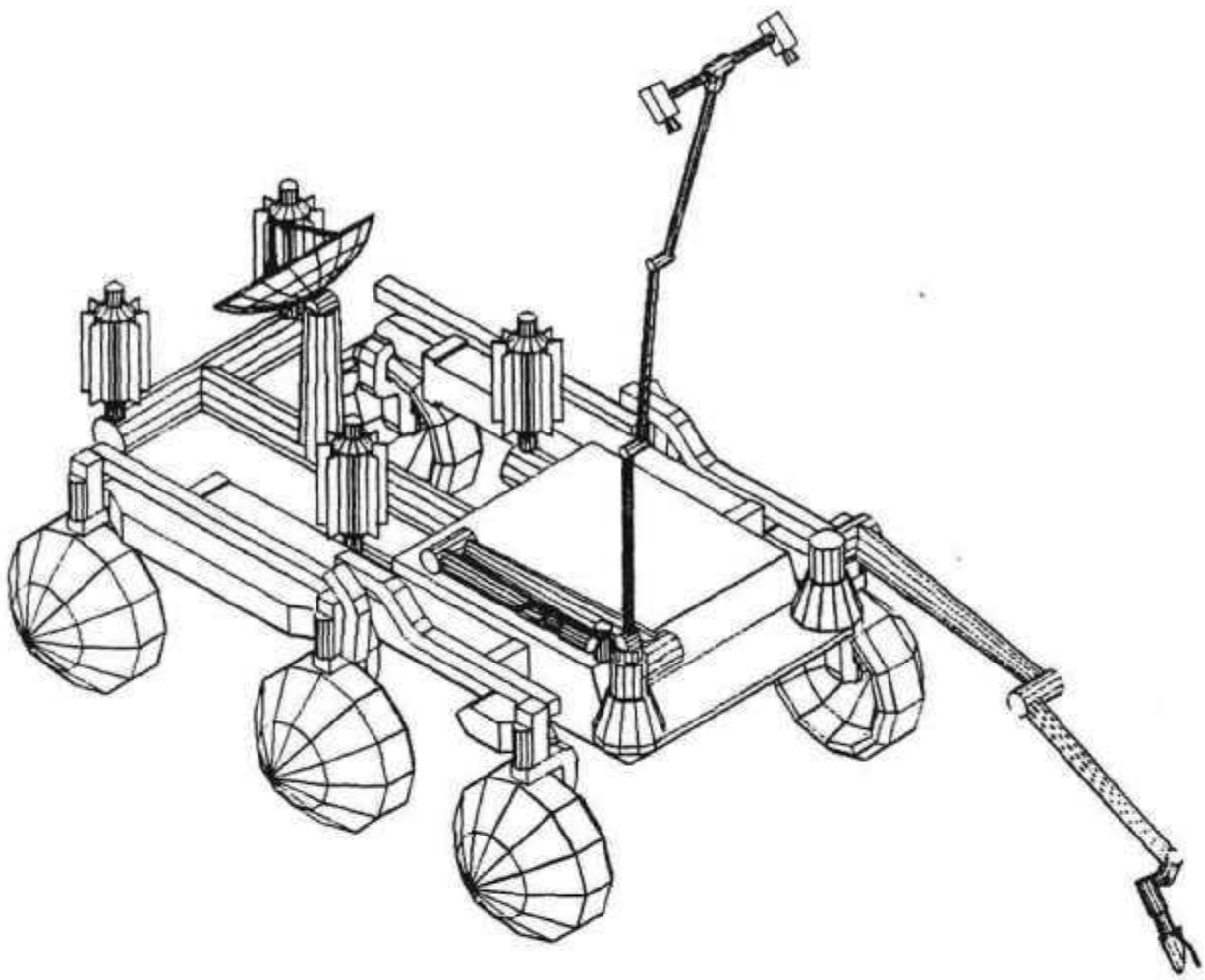

An alternative Rover design is illustrated in Figure 5. This "walking beam" design was developed by the Martin Company, under contract to JPL. In the illustrated version, it employs two tripods, linked by a tracked beam. During movement, one tripod rests on the ground, and the legs of the other are raised, enabling it to move along the tracked beam. During the next step, the position of the two tripods are reversed. Directional changes are accomplished by using a turntable to pivot the raised tripod about the point where it the joins the grounded tripod.

Figure 5. Illustrative Rover Design Walking-Beam Option

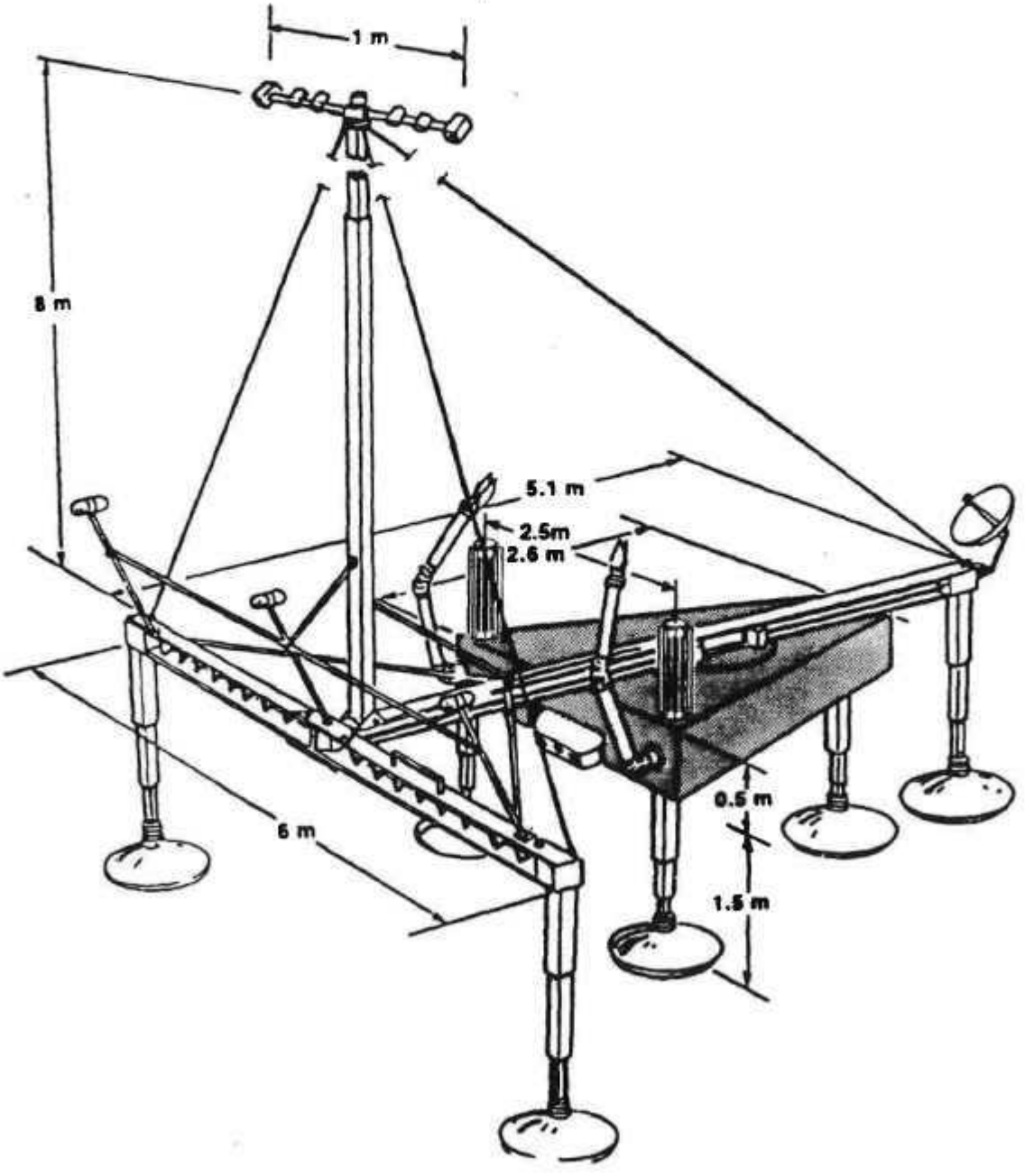

3.0 ROVER POWER SYSTEM

3.1 RTG REQUIREMENTS

The MRSR mission calls for the Rover to operate for four years after launch. The launch is assumed to occur three years after fuel encapsulation, and to be preceded by one year of full-temperature operation of the thermoelectric converters. Thus, by the end of the mission the RTG's fuel will have decayed for seven years, and its converters will have degraded as a result of operating at full temperature for five years.

As illustrated in Figure 6, the Rover has an average power requirement of 500 watts, with peak power demands of over one kilowatt when the Rover is climbing a slope or in the process of sample acquisition. The RTGs will be designed to provide continuous power with an output of 500 watts at the end of the mission, and will be supplemented by high-power-density rechargeable batteries for meeting power demand peaks that exceed the output of the RTGs. These batteries will be recharged by the RTGs during the periods of low power demand.

Figure 6. Power Demand Profile for Typical Mars Rover Activities

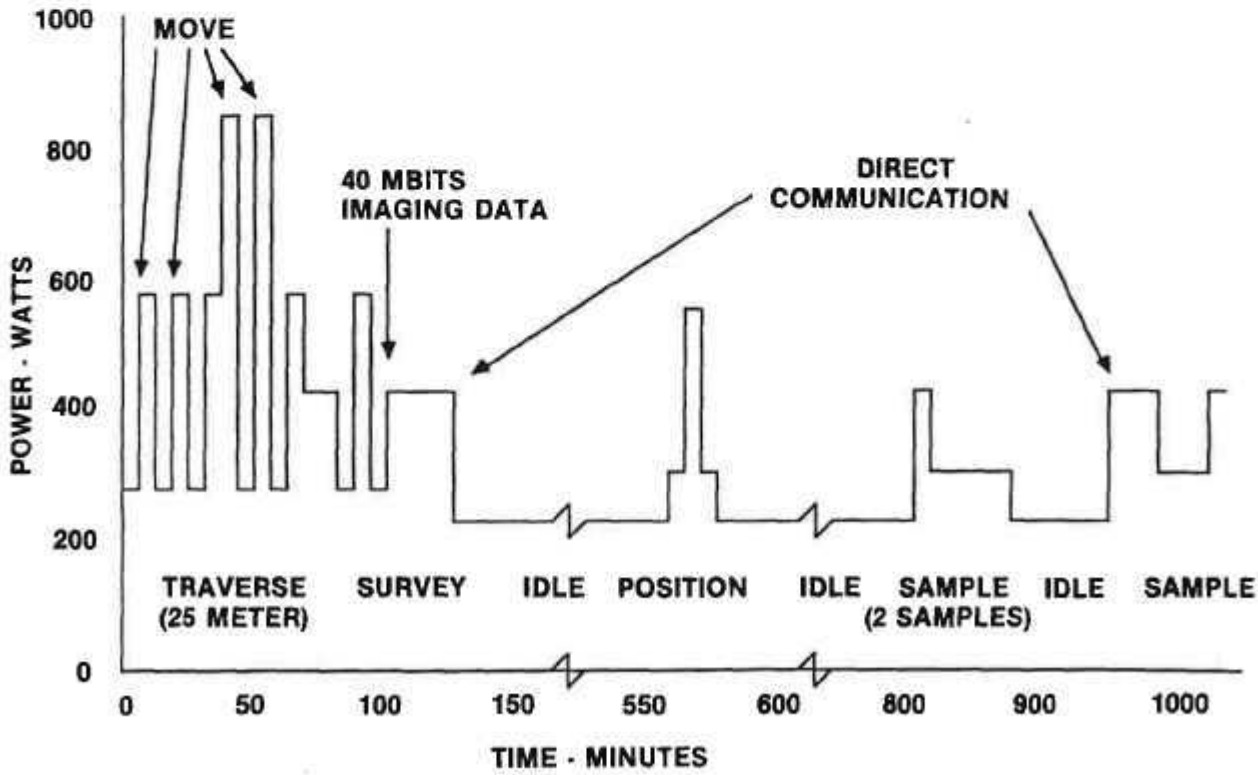

The number and location of RTGs on the Rover are critical and require trade-off analysis. The Rover designers may prefer several small RTGs distributed around the vehicle, since this arrangement can help in the load distribution and facilitate the use of the RTGs' waste heat for thermal management of the Rover body and electronics bays. Also, shorter RTGs are less likely to block other Rover instruments and/or antennas. On the other hand, longer RTGs offer a higher specific power, because of decreased end losses and weights. They also are less likely to obscure the view of each other's radiators to space. At present, two concepts for integrating the RTGs with the Rover are undergoing evaluation, one employing two 250-watt RTGs, and one employing four 125-watt RTGs mounted on top of the Rover. The four-RTG option was illustrated in Figure 4, and the two-RTG option was shown in Figure 5. Either option could be used with either type of vehicle. Note that the RTGs are mounted vertically, to prevent build-up of sand on their heat rejection surfaces during Martian storms.

3.2 RTG ENVIRONMENT

Both the Rover and Mars environments present new challenges to the RTG designer. Previous RTGs (MHW, GPHS) were designed primarily for operation in microgravity and in a high vacuum after launch. The Rover and Mars environments are more difficult, mechanically, thermally, and atmospherically.

From the dynamic-environment point of view, the Rover RTG has to withstand launch, entry, landing, and traverse loads that occur at different times in the life of the mission. These loads cannot be accurately determined until the spacecraft and Rover structures are better defined. In the absence of such definition, the RTG design study was conservatively based on 3-axis design loads of 25 G during Earth launch and 15 G during and after Mars landing, for the duration of the mission.

During entry into the Martian atmosphere, the Rover-mounted RTGs are enclosed in a protective aeroshell, as illustrated in Figure 7. While they are enclosed in that aeroshell, they are unable to radiate their waste heat to space, and will therefore require an auxiliary cooling loop. For short periods, during Earth launch and Mars entry, a water boiler dumping steam overboard could be used as the loop's heat sink. But for the much longer orbital transit period, a steady state-heat rejection system is required. Therefore, during the cruise to Mars, the RTGs will either require a mechanism for their temporary deployment outside the aeroshell, to permit radiative cooling; or will require continuous operation of the auxiliary cooling loop to transfer their waste heat to radiators located on or outside the Rover's aeroshell. The latter option is probably preferable, because it avoids the mechanical complexity and potential unreliability of a deployment mechanism. The necessary reliability of the auxiliary cooling loop can be achieved by the use of redundant coolant pumps.

Figure 7. Rover with RTGs and Lander Enclosed in Aeroshell

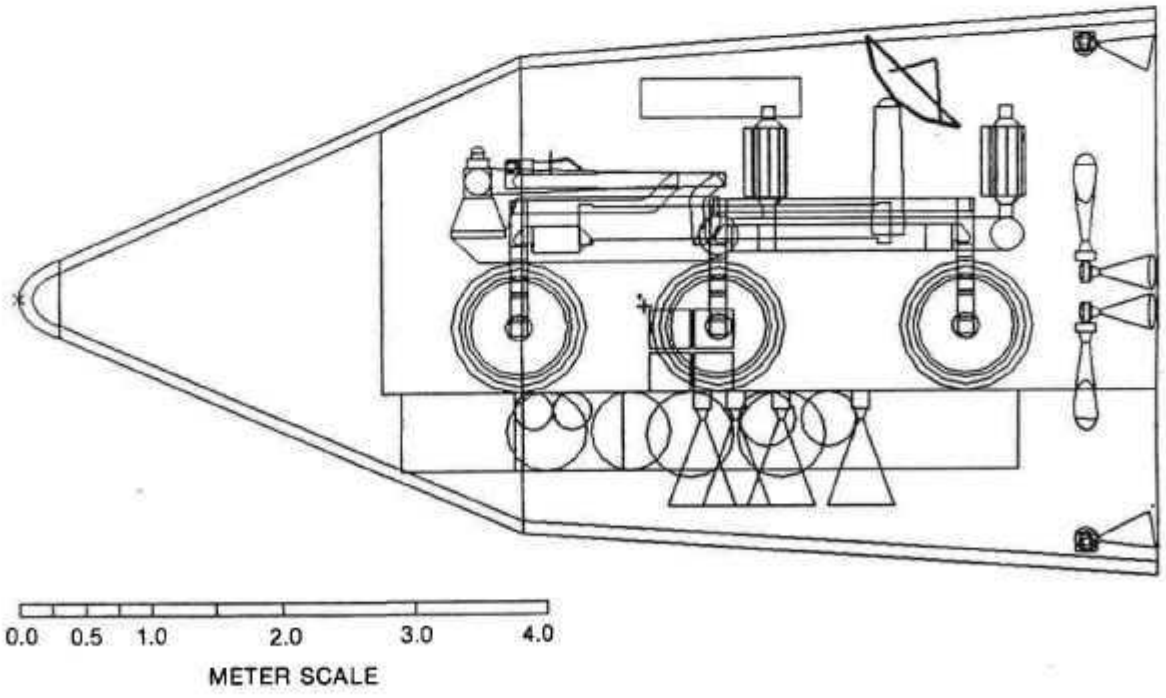

The most difficult problem imposed by the Mars surface environment is the presence of an external atmosphere [10]. The thermoelectric converter elements in the RTG are embedded in multifoil thermal insulation, to minimize heat losses from the hot heat source to the cool generator housing. Thus, the insulation forces most of the heat to flow through the thermoelectric legs.

Multifoil insulation performs well in the absence of conducting gases, but degrades rapidly when such gases are present. Moreover, at the projected operating temperatures even small amounts of some of the Martian gases would react with the converter's materials and degrade its performance. Therefore, both inleakage of Martian gases and buildup of alpha-generated helium in the converter must be prevented.

4.0 DESIGN APPROACH

The present report is focused first of all on a detailed description of a "baseline" RTG and its design rationale. The baseline design employs proven components and performance parameters. To minimize the need for new developments, the baseline design is conservatively based on: standard General Purpose Heat Source modules, which have been developed and safety-qualified for the Galileo mission; standard SiGe unicouples, developed and extensively lifetested for the Voyager and Galileo missions; and thermoelectric performance parameters and degradation rates that have been demonstrated in extended ground tests and space missions.

The report presents a detailed description of the baseline RTG's design, mass breakdown, and of its structural, thermal, thermoelectric, and electrical analyses, for a variety of environmental conditions. It then presents RTG designs and analytical results for a number of alternative design options, including more advanced (and less developed) converter configurations and thermoelectric materials.

4.1 THERMOELECTRIC MATERIAL

The first design decision is the selection of the thermoelectric materials. The basic choice is between TAGS (Te-Ag-Ge-Sb) and SiGe (with or without GaP additives). TAGS was used on earlier missions, including the 1976 Viking mission to Mars. SiGe is used in all recent and current space RTGs, including LES-8/9, Voyager, Galileo, Ulysses, and the more advanced Mod-RTG under development by DOE.

TAGS thermoelectrics operate at lower hot- and cold-junction temperatures than SiGe. Their hot-junction temperatures are far below the temperature capability of current radioisotope heat sources. Therefore they would not take proper advantage of that capability. SiGe elements come much closer to matching the heat source temperature limits.

Since TAGS elements operate at much lower hot-junction temperatures than SiGe, they also demand correspondingly lower cold-junction temperatures for efficient operation. This would require relatively large and heavy radiators. The lower cold-junction temperatures would be particularly disadvantageous in the present application, because they would make the RTG power output more sensitive to the large seasonal and diurnal temperature fluctuations on the Martian surface.

TAGS thermoelectric elements have only been used in spring-loaded RTGs. Such RTGs tend to be much heavier than radiatively coupled RTGs, particularly since they use relatively bulky and inefficient fibrous insulation. By contrast, the thermoelectric elements in SiGe RTGs are heated radiatively. Thus, they do not contact the heat source, and no spring loading is required. They are insulated with lighter, more compact, and more efficient multifoil insulation.

For these reasons, the Rover RTG design study is based on the use of SiGe rather than TAGS elements.

4.2 HEAT SOURCE

DOE has spent approximately ten years and $40-50M on the development [11] and safety qualification [12] of the General Purpose Heat Source (GPHS), for initial deployment on the Galileo and Ulysses space exploration missions. As a result of that effort, this heat source is extremely well characterized, much more so than radioisotope heat sources used on previous space missions.

The heat source is modular, and a sectioned view of a standard 250-watt module is shown in Figure 8. Viewed from the outside, each GPHS module is a graphite brick of roughly 2 x 4 x 4 inches. This module was used as the building block for all RTG designs presented in this report.

Each GPHS module contains passive safety provisions to prevent or minimize fuel release under all credible accident conditions. As shown, each module contains four iridium-clad $Pu^{238}O_2$ fuel capsules surrounded by graphitic components, including an aeroshell designed to withstand reentry ablation, an impact shell to help absorb impact energy and reduce fuel capsule deformation during earth impact, and a thermal insulator between them. The thermal insulator is designed to avoid embrittlement of the iridium capsule, by preventing excessively high clad temperatures during the hypersonic reentry heat pulse, which would cause excessive grain growth; and by preventing excessively low clad temperatures during the module's subsonic atmospheric descent, which would drop the temperature of the iridium capsule below its ductile-brittle transition point.

Figure 8. General-Purpose Heat Source Module (250 Watt)
Sectioned At Midplane

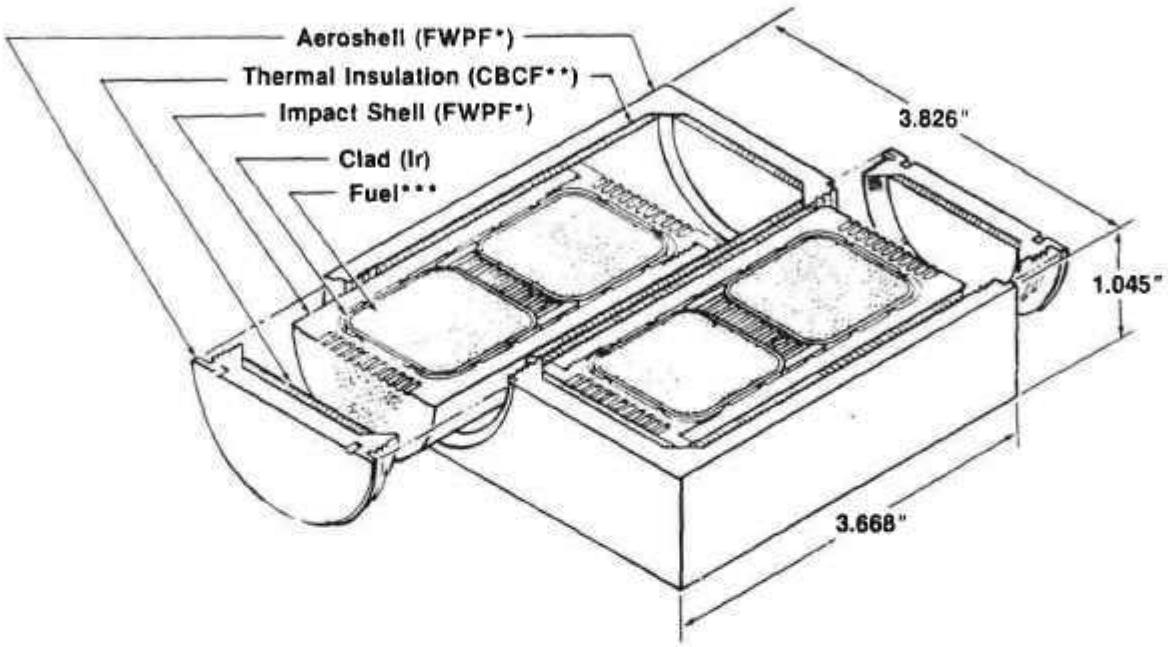

*Fine-Weave Pierced Fabric, a 90%-dense 3D carbon-carbon composite
**Carbon-Bonded Carbon Fibers, a 10% dense high-temperature insulator
***62.5-watt $^{238}PuO_2$ pellet

4.3 THERMOELECTRIC UNICOUPLES

The baseline RTG design employs standard SiGe unicouples and is based on demonstrated thermoelectric performance levels and degradation rates. A very extensive experimental data base exists for such unicouples. Large assemblies of SiGe unicouples have operated successfully in the MHW RTGs flown on the Voyager and LES 8/9 missions and in the GPHS RTGs for the Galileo and Ulysses missions. They have demonstrated stable performance with moderate and predictable degradation rates for periods in excess of 100,000 hours, most recently on the Neptune flyby twelve years after Voyager's launch.

The design of the standard unicouple is depicted in Figure 9. The p- and n-doped SiGe legs are 0.8" long, and the 1"-square hot-shoe collects the heat radiated by the heat source and delivers it to the TE legs. The cold end of the unicouple is bolted to the RTG housing, and the electrical connections between couples are made on the inside of the housing. There is no physical contact between the cantilevered unicouples and the heat source.

Figure 9. Unicouple

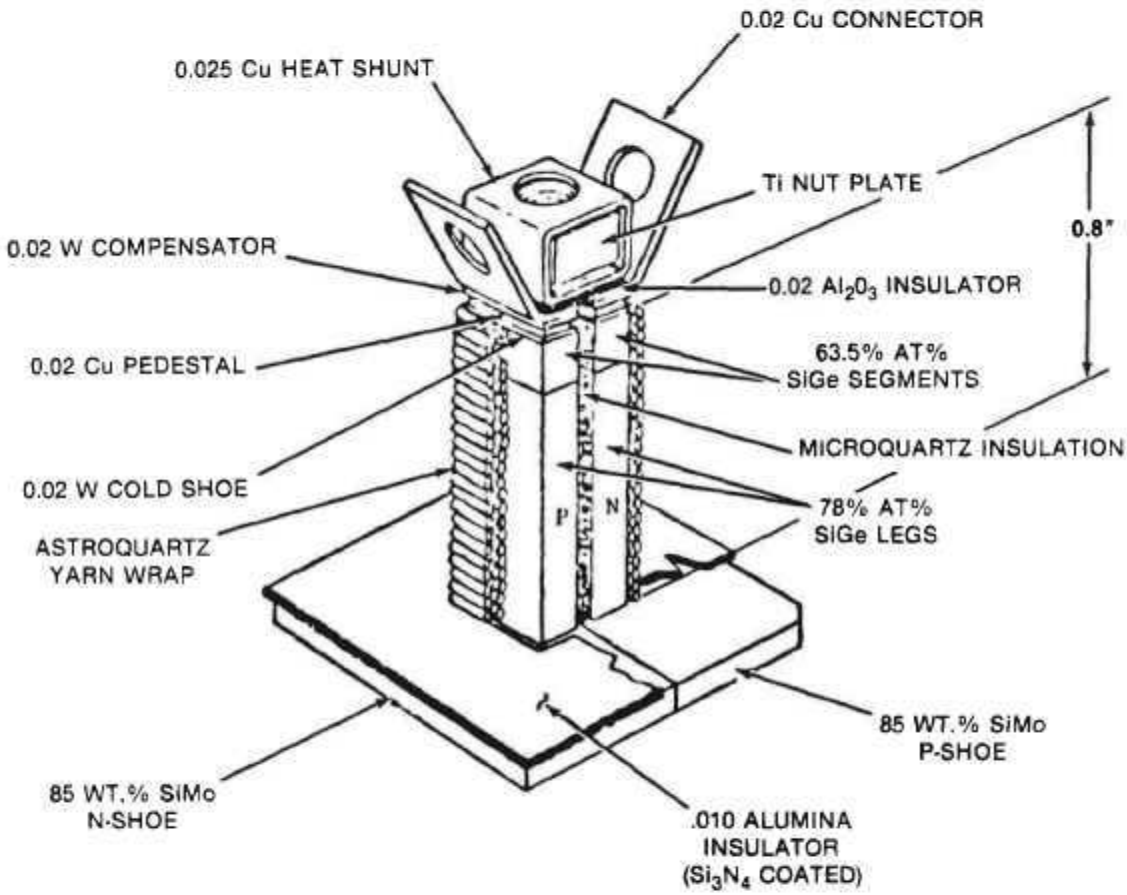

5.0 KEY DESIGN ISSUE

5.1 PROBLEM

The key problem in designing an RTG for Mars surface operations is the need to vent the helium generated by the fuel's alpha decay to the outside without allowing the Martian atmosphere to enter into and build up harmful quantities of gases within the RTG. In the 1976 Viking mission to Mars, the 35-watt RTGs used fibrous insulation, which is much less effective than multifoil and leads to a substantially higher system mass. However, the more efficient and compact multifoil insulation used in the present study is only effective in a good vacuum (<1 torr). But the existing GPHS-RTG and Mod-RTG both use a large number of metal C-ring seals. Such seals are adequate for retaining the inert cover gas during the short launch period, but not for preventing intrusion of the Martian atmosphere during extended Mars operations.

To prevent helium pressure buildup inside the RTG above 1 torr, the use of a selective vent has been considered. But to maintain an internal helium pressure of less than one torr, such a vent would have to have a very low flow resistance. However, a low-flow-resistance vent would allow appreciable back diffusion of Martian gases into the RTG. This would be unacceptable unless these Martian gases were effectively gettered as soon as they entered the RTG. Even small quantities of Martian gases (CO, CO_2, O_2) would result in deleterious reactions with the RTG materials.

5.2 PROPOSED SOLUTION

Since the system of selective vent and effective getter has not yet been demonstrated, the Fairchild study was based on RTG designs with an evacuated annular converter, sealed off from the both the internal helium and the external Mars atmosphere.

This is illustrated in Figure 10, which shows a horizontal cut through the active region of the baseline RTG; i.e., through the midplane of a heat source module and through the midplane of a ring of thermoelectric unicouples. Different shading patterns are used to designate the helium volume inside the heat source canister and the Martian atmosphere outside the RTG housing. As shown, the intervening annular converter is evacuated, and is separated from the helium by the heat source canister and from the Martian atmosphere by the RTG housing.

Figure 10. Horizontal Cut Through Baseline RTG

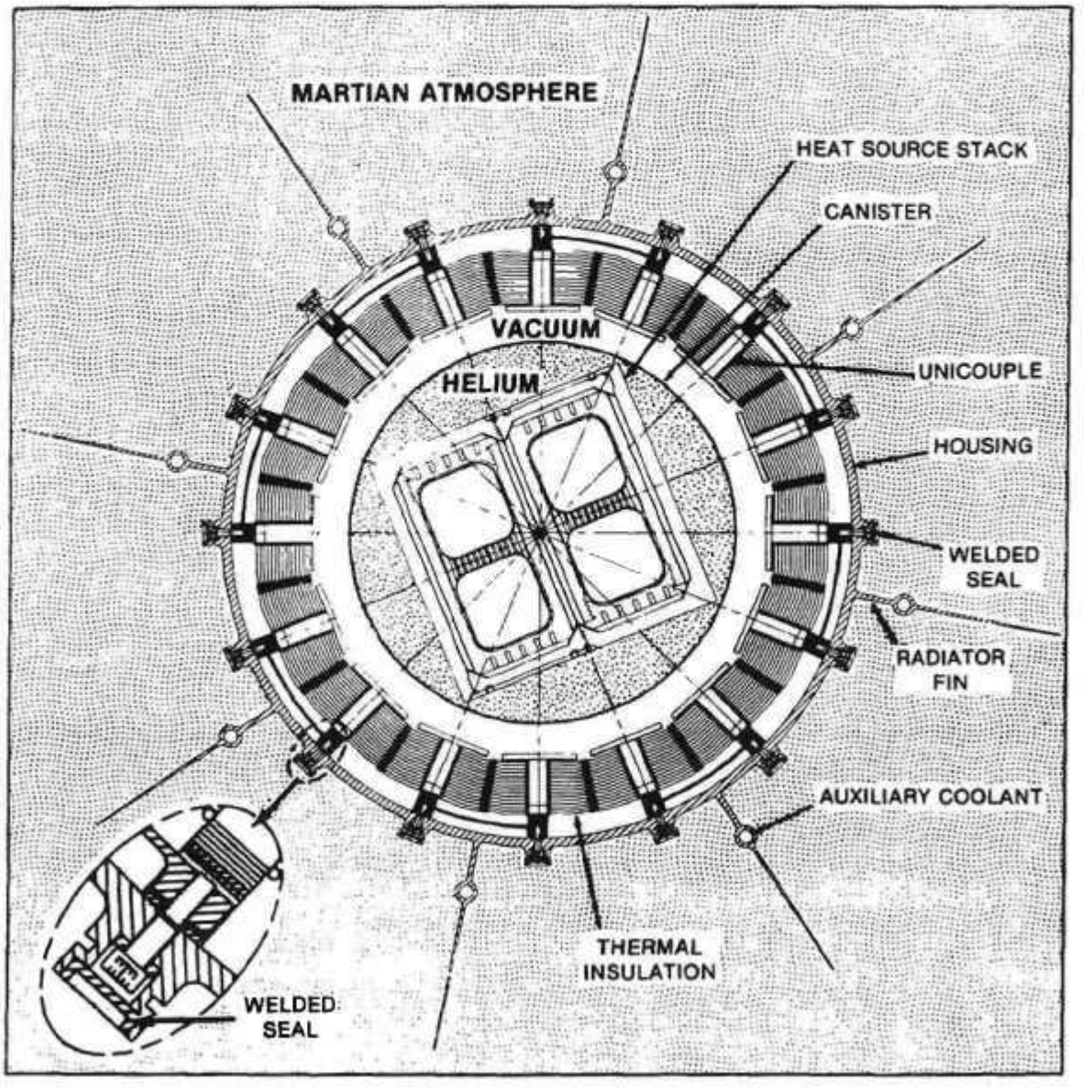

6.0 BASELINE RTG

6.1 DESIGN DESCRIPTION

6.1.1. Horizontal Cross-Section: In Figure 11 Section AA shows a horizontal cut through the active region of the RTG, and Section BB depicts the support structure at the top of the heat source.

As in the Galileo RTG, there are 16 unicouples in each layer, and these are bolted to the housing at 22.5° intervals. The unicouples reject their waste heat to the RTG housing.

In the Galileo RTG the mounting bolt holes of its 572 unicouples are sealed by metal C-rings, but these would be inadequate for preventing inflow of the Martian atmosphere over the mission life. In the present design, the bolt holes are hermetically sealed by 16 aluminum cover strips welded to the aluminum housing ribs, as illustrated in the enlarged inset in Figure 10.

The unicouples in the baseline RTG are embedded in a 0.8″-thick layer of thermal insulation, consisting of 60 alternating layers of 0.0003″-thick molybdenum foil and quartz cloth. This type of insulation, which was used in the MHW and Galileo RTGs, is considerably heavier than multifoil insulation with zirconia-particle spacers used in the Mod-RTG.

As in the Galileo RTG, the housing has eight radiator fins and each fin contains an auxiliary cooling tube. The auxiliary coolant (e.g., water and anti-freeze) is used to control the RTG housing temperature during launch and during transit to Mars, while the RTG is enclosed in the aeroshell that protects the Rover and lander during their entry into the Martian atmosphere.

After aerocapture and entry into the Martian atmosphere, the aeroshell is jettisoned, the auxiliary cooling is discontinued, and the RTG is cooled primarily by radiation from the fins. Convective cooling by the Martian atmosphere, even on a cold windy day, makes only a relatively minor contribution to heat rejection.

The trapezoidal radiator fins shown in Figure 11 have a root thickness of 0.066", a tip thickness of 0.015", and a root-to-tip height of 3". These dimensions are merely illustrative. Increasing the fin height and/or the root thickness raises the conversion efficiency but also increases the radiator mass. For a given RTG design, there is an optimal combination of fin height and thickness which maximizes the generator's specific power. This will be determined by a detailed radiator design optimization.

Figure 11. Horizontal Sections Through Baseline RTG

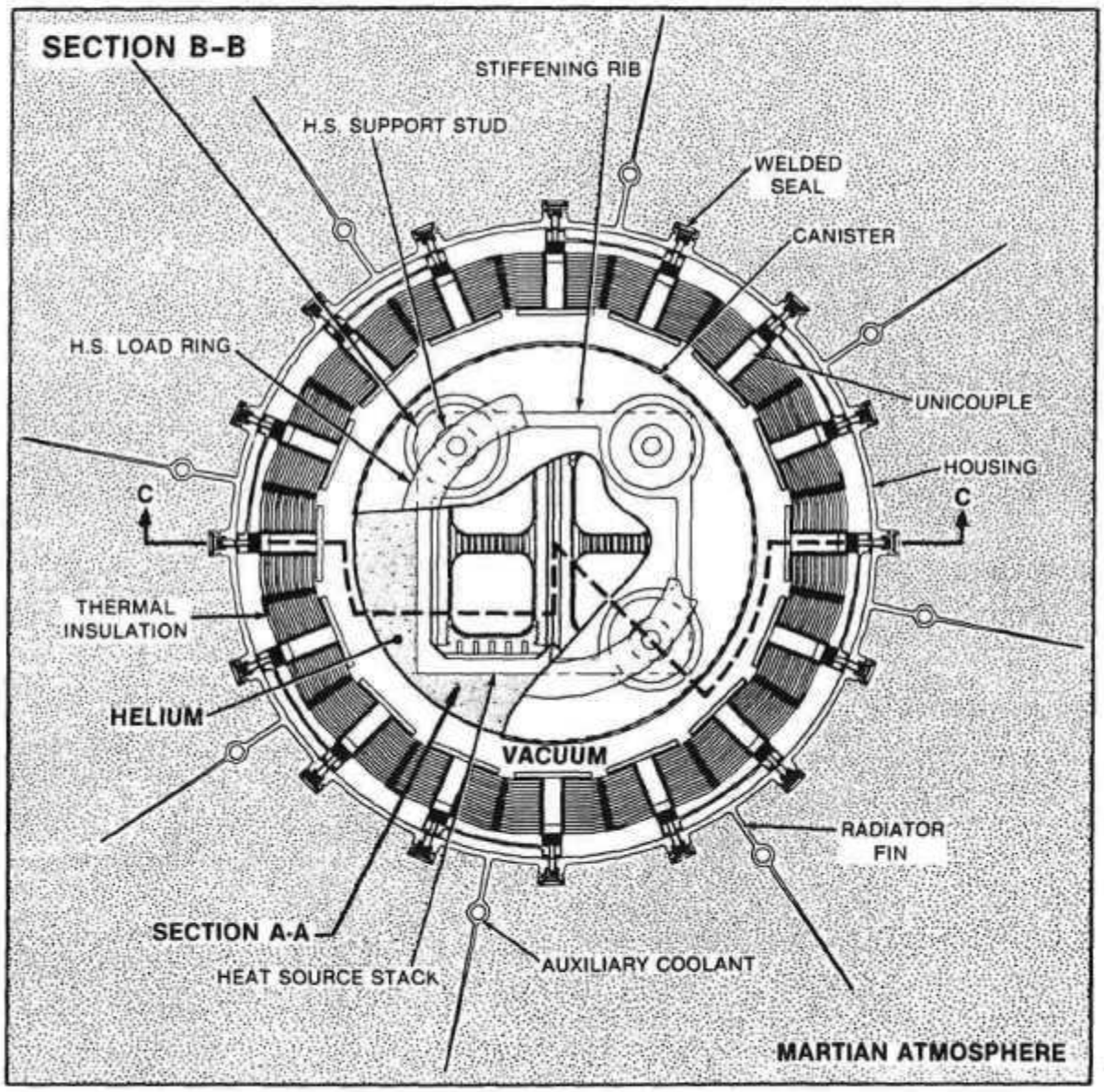

6.1.2 Converter Layout: Figure 12 shows a cutaway view of the top of the thermoelectric converter, before insertion of the radioisotope heat source. The converter contains 576 SiGe unicouples. These are arranged in 36 horizontal rings, each consisting of 16 equispaced unicouples, depicted earlier in Figure 9. Each unicouple has a ~1"x1" heat collector, which concentrates the heat radiated from the heat source and delivers it to the couple's n- and p-legs. Heat transfer from the heat source canister to the unicouples is by radiation across a vacuum gap, without any physical contact. The RTG design is based on a maximum hot-junction temperature of 1000°C, which is the temperature at which unicouple assemblies have demonstrated long-term reliability and performance stability in extended ground tests and space operations.

As indicated in Figure 12, the 576 thermoelectric couples are embedded in 0.8"-thick thermal insulation, to minimize heat loss to the cooler RTG housing. The insulation consists of 60 layers of 0.0003" molybdenum foils separated from each other by alternating layers of quartz cloth. This is a very conservative insulation design, whose reliability has been demonstrated in long-term ground tests and space operations. The alternative of separating the molybdenum foils with zirconia particles instead of quartz cloth, which has been successfully used in more recent thermoelectric converter assemblies, would lead to considerably lighter and more compact insulation packages.

The unicouples deliver their waste heat to the RTG's aluminum housing. The housing and its eight fins serve to reject the RTG's waste heat, either by radiation to space or (when direct radiative cooling is not possible) by convection to the auxiliary coolant in the fins' integral cooling tubes.

Figure 12 also shows the electrical series and parallel connectors between unicouples. The copper connectors are located between the multifoil insulation and the RTG housing. The connection scheme is explained in the next section.

Figure 12. Unfueled Converter

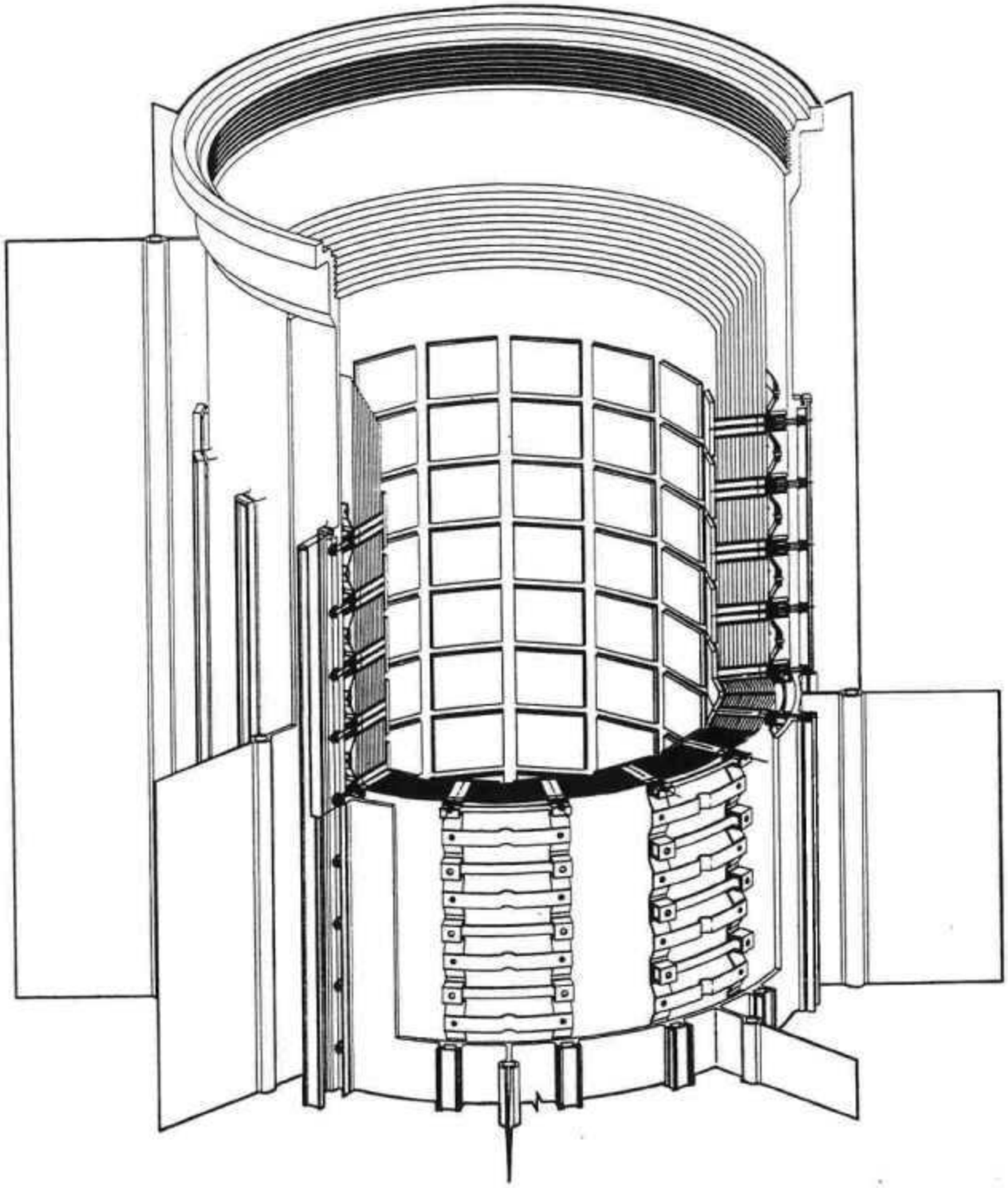

6.1.3 Electrical Circuit: As shown in Figure 13, the 576 couples in the baseline RTG are connected in two identical (180-degree) series-parallel networks. There are 144 couples in series, to generate the desired 30-volt output. The couples in each network are parallel-connected in groups of two, to eliminate the risk of single-point failures. If any couple were to experience open-circuit failure, its partner would carry the increased current, permitting continued RTG operation. Alternatively, the 576 couples could be connected in a single 144 x 4 series-parallel network for even higher reliability.

The thermoelectric circuit floats with respect to the grounded RTG housing. This is done to eliminate the risk of a short to ground causing a single-point failure of the RTG.

Figure 13. Schematic Circuit Diagram of Baseline RTG

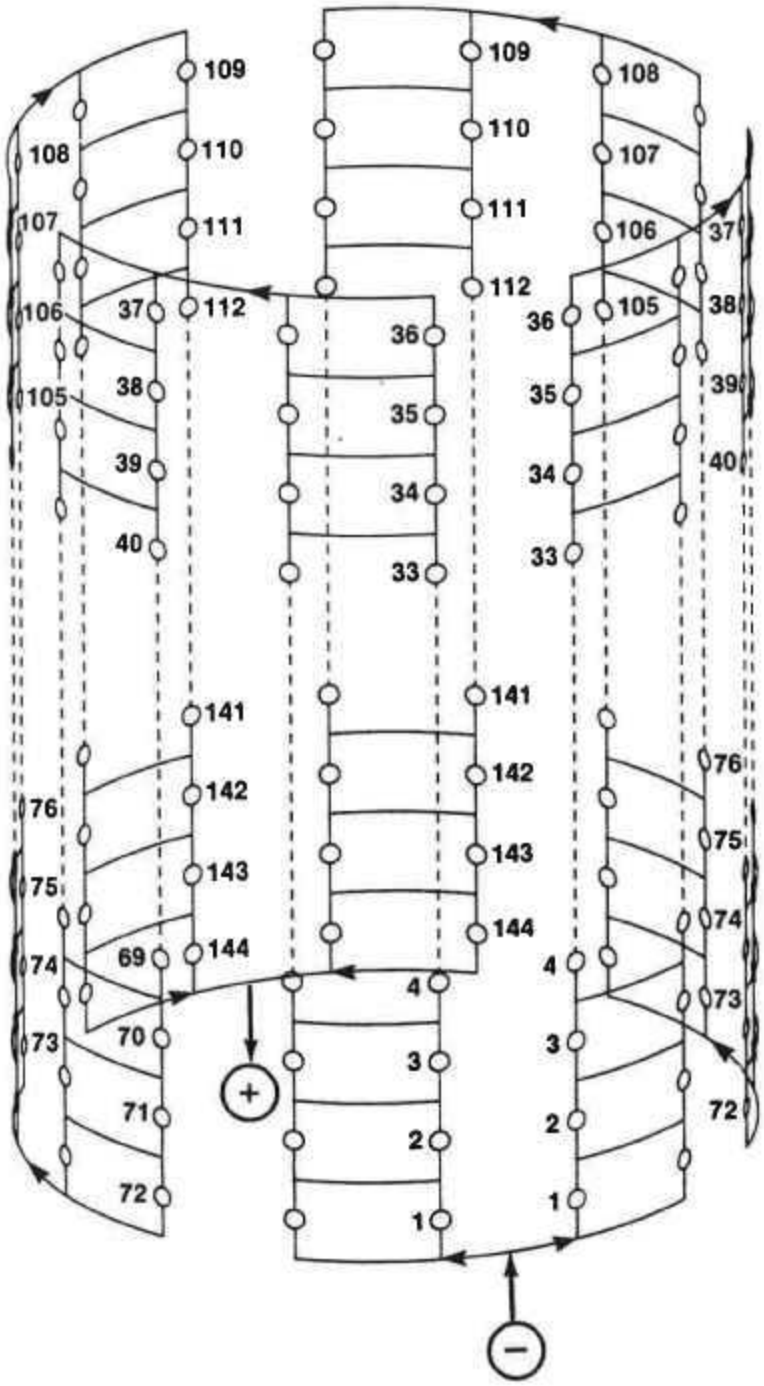

Figure 14 shows a partially exploded cutaway view of the top of the RTG, after fueling. At its center is the heat source, consisting of a stack of 18 GPHS modules. The heat source stack is contained in a cylindrical molybdenum canister which acts as a helium container. The canister's end caps serve to provide the lateral support and axial compressive load to the ends of the heat source stack. The stack does not touch the canister along its length, and does not have any midspan supports.

The conservative baseline RTG, designed to produce 250 watts(e) at the end of the 4-year MRSR mission (i.e., 7 years after fuel encapsulation), has an overall height of 45.9 inches, a housing diameter 9.1 inches, and a tip-to-tip span of 15.2 inches.

6.2 HEAT SOURCE SUPPORT

One of the most critical issues in designing an RTG with stacked heat source modules is the scheme for supporting that stack.

The GPHS module design is primarily driven by safety considerations. The modules are designed to survive hypersonic reentry and subsequent ground impact without fuel release. To maximize the impact safety margin, one wishes to minimize the impact velocity. Individual modules have a much lower impact velocity (49 m/s) than the stacked heat source (74 m/s). Therefore, it is desirable to support the heat source stack in such a manner that the individual modules separate in case of inadvertent reentry into the Earth's atmosphere. Automatic separation is accomplished by structurally supporting the heat source stack from the RTG's aluminum housing, which melts during reentry, releasing the modules. But the same support structure must hold the stacked modules together during launch and operational vibration and shock loads.

Figure 14. Fueled RTG

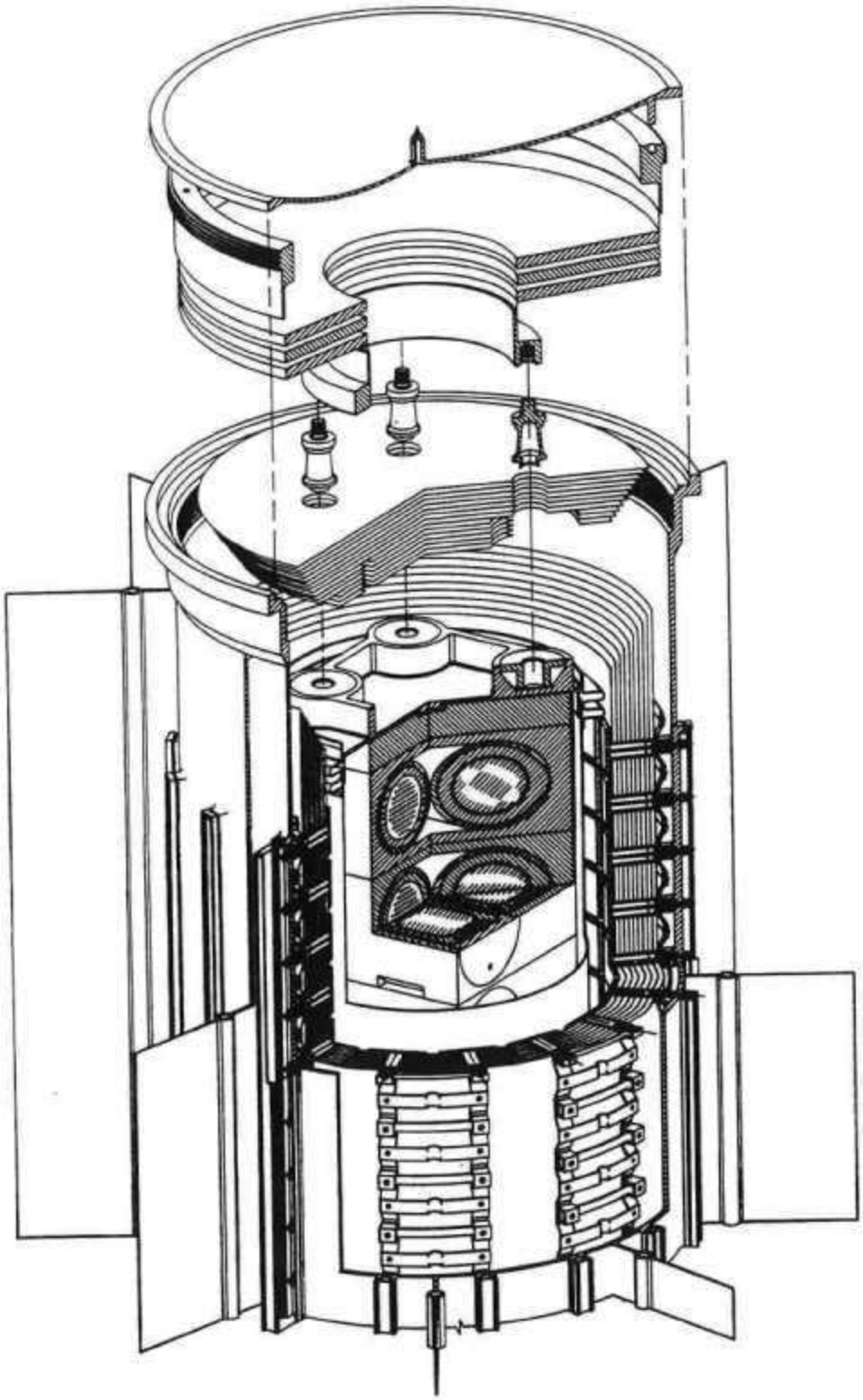

6.2.1 Description of Support Structure: The heat source support arrangement will be described in detail with respect to the baseline RTG design. The same basic arrangement applies to the alternative RTG designs discussed in the subsequent sections.

Since the heat source stack is only supported at its ends and there are no midspan supports, a large (5500-lb) axial preload is required to hold the stack together during launch under the assumed 25-G transverse load. The axial preload is applied directly to the ends of the stack, via the canister's end caps. The canister's side wall plays no structural role; it is merely a helium container, and is thin enough to burn off during reentry.

Figure 15 presents an exploded closeup of the support structure at the top of the heat source stack. As shown, the top of the heat source stack is followed by a graphite transition section which bears against the top cap of the molybdenum canister via a thin iridium sheet that serves as a reaction barrier between the graphite and the molybdenum.

On the outside of the canister end cap is a set of integral stiffening ribs and load stud seats. These form a square structure, to spread the axial load from the four load studs to the four edges of the heat source end face. The four studs at each end are similar to those used in the Galileo RTG. They are made of low-conductivity Inconel, and are separated from the stud seats by zirconia insulators to reduce axial heat losses and to lower the temperatures of the creep-prone Inconel studs and titanium springs. As indicated in Figure 14, the load studs penetrate through the multifoil thermal insulation.

The tops of the four studs are bolted to a titanium load ring, which is laterally supported and axially loaded by a set of three nested Belleville springs made of 0.22"-thick titanium. Three springs are used in order to generate the required preload without exceeding the allowable stress in the springs. The I.D. of the bottom spring bears against the load ring, and the O.D. of the top spring bears against a titanium preload adjustment ring that is threaded to the I.D. of the aluminum housing. After the load is set, rotation of that ring is prevented by pins protruding from the RTG's aluminum cover. That cover serves only as a pressure dome, and has no other structural function.

Figure 15. Exploded View of Support Structure at Top of Heat Source

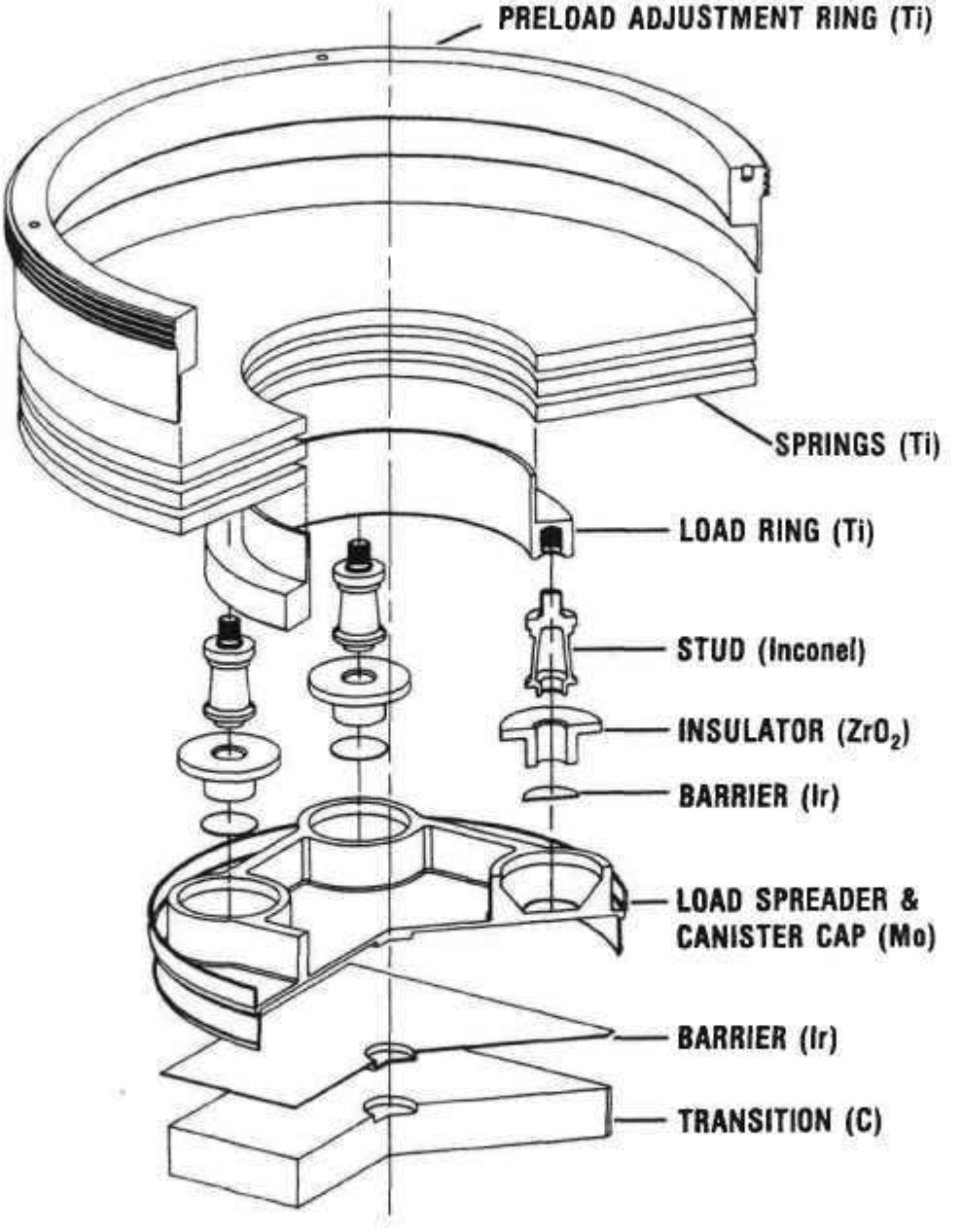

Figure 16 shows an exploded view of the heat source's lower support structure (viewed from below), and Figure 17 shows a cutaway view of the lower end of the assembled RTG. As can be seen, the lower support structure uses an identical set of load spreaders, zirconia insulators and Inconel studs as the upper support structure. But there are no springs, and the studs are mounted directly on the RTG's aluminum base plate. The base plate employs 1″ x 0.25″ radial and circumferential ribs to provide the required stiffness.

Figure 16. Exploded View of Support Structure at Bottom of Heat Source

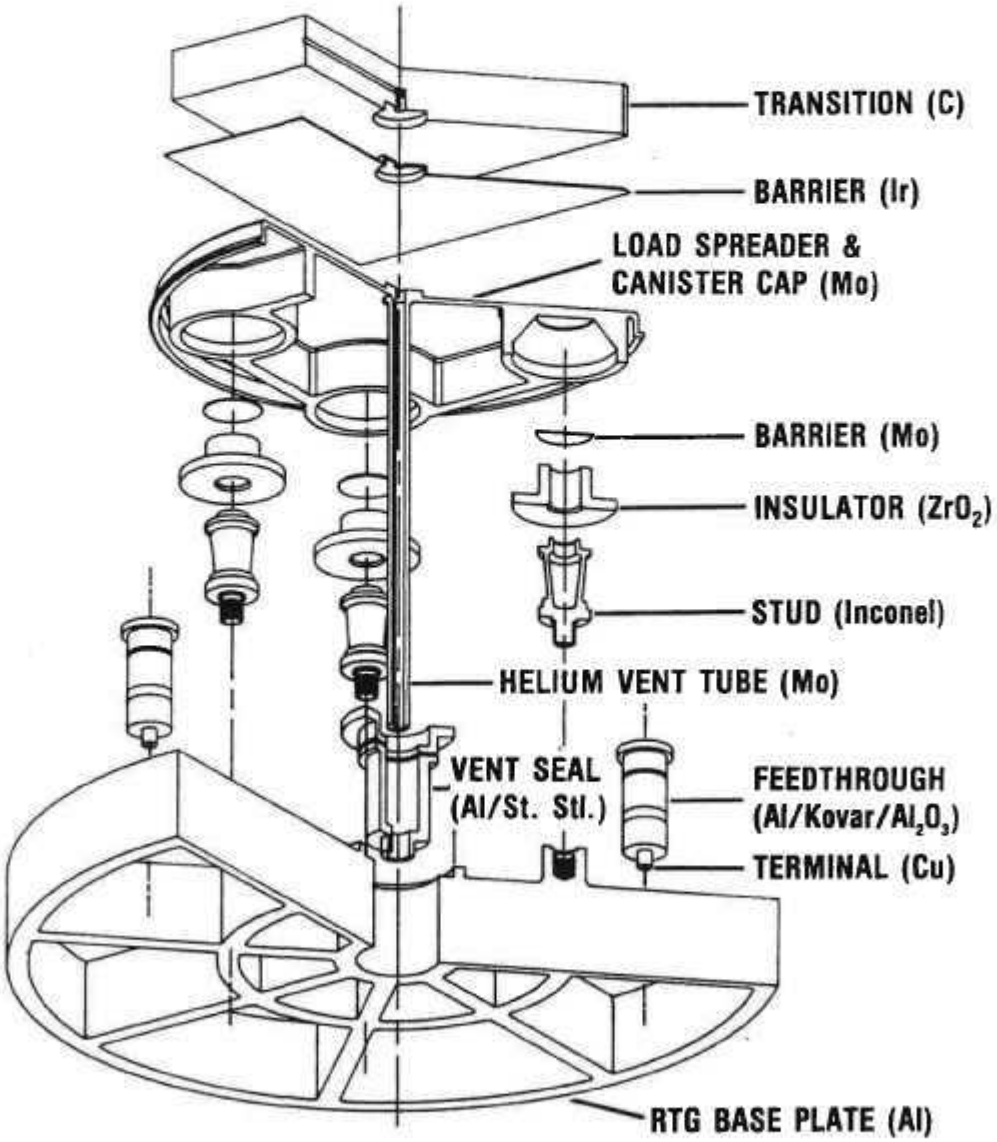

The figures also show the helium vent tube at the center of the canister's base. The vent tube passes through the evacuated converter region and is sealed to the RTG base plate. A bimetallic joint is used to seal the vent tube to the aluminum base plate. Similar bimetallic joints are used to connect the aluminum base plate to the metal-ceramic seals which serve for the electrical isolation of the RTG terminals. The helium generated by the fuel's alpha decay is vented to space, through a semi-permeable Viton seal which prevents inflow of the Martian atmosphere into the heat source canister. In effect, the Viton seal acts as a pressure relief device.

Figure 17. Lower End of Assembled RTG

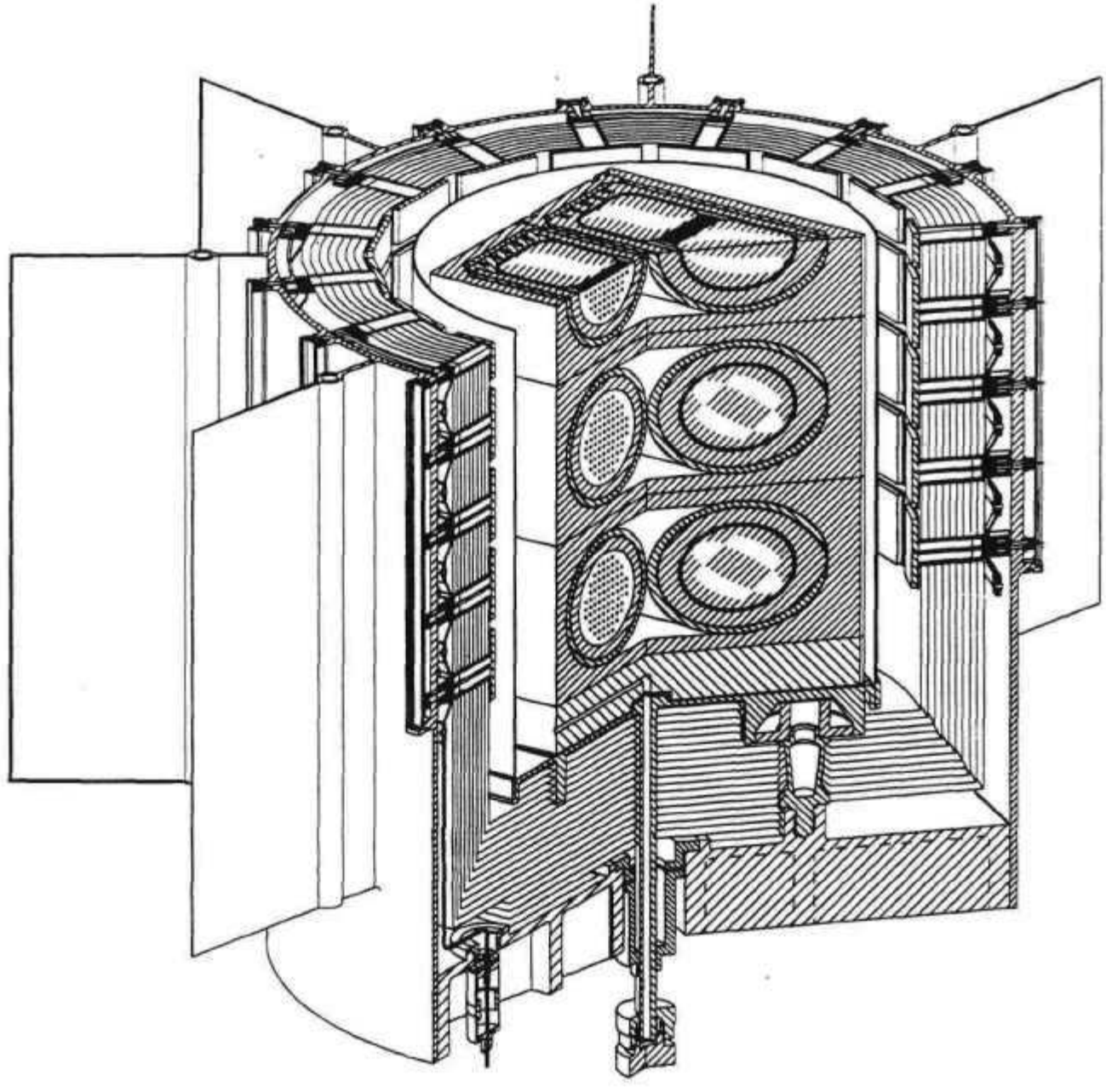

Figure 18 shows the upper and lower ends of the assembled RTG. When sealed, the Belleville springs place the heat source stack under compression and the housing under tension.

Clearly, the heat source stack is ultimately held together by the RTG's low-melting aluminum housing. When that housing and the thin canister burn away during reentry, the heat source modules are free to disperse and impact individually.

As shown, the RTG has an overall height of 45.9″, a housing diameter of 9.1″, and a tip-to-tip span of 15.2″.

Figure 18. Rover RTG, Baseline Design

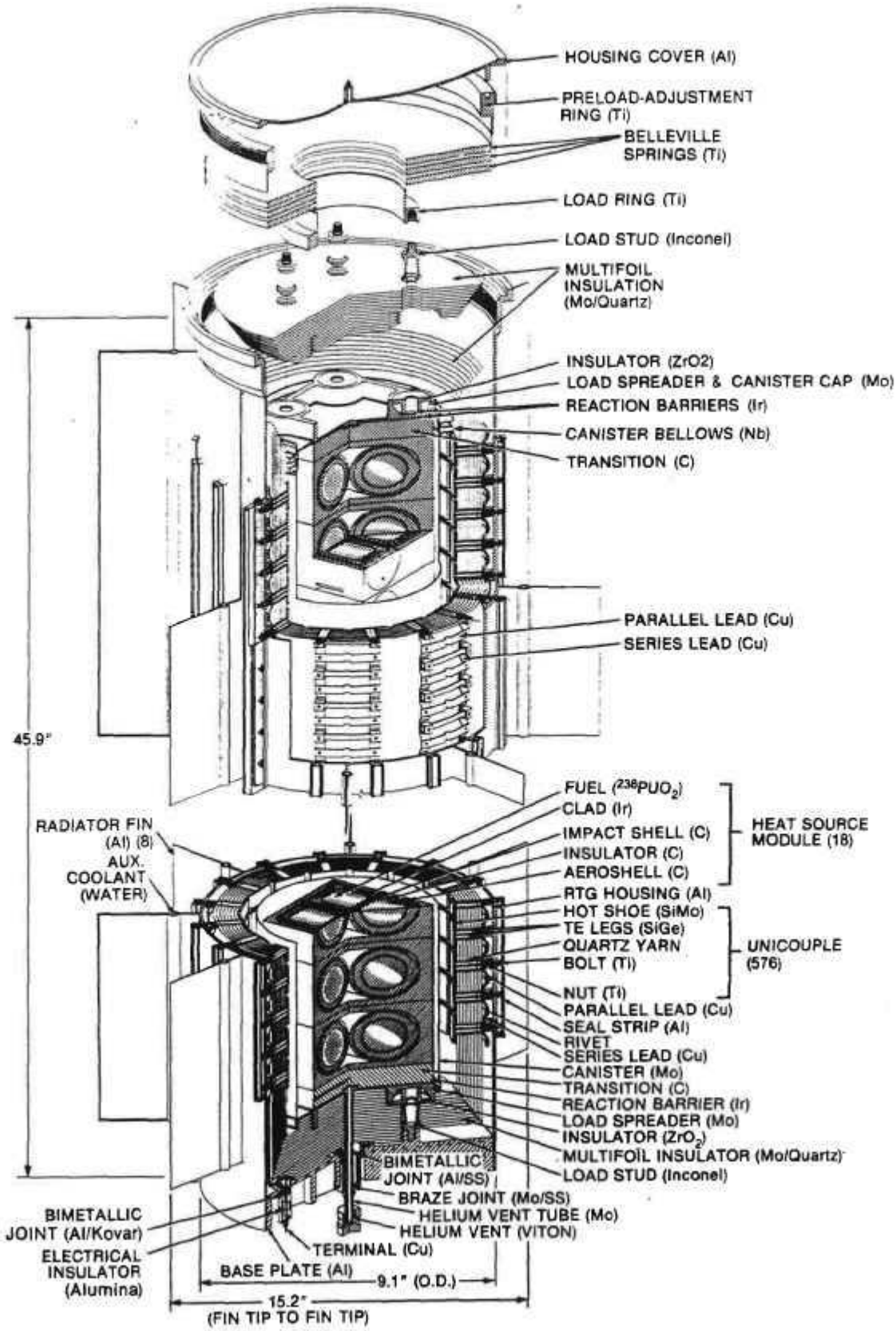

6.2.2 Structural Analysis: The Belleville springs shown in Figures 14 and 15 must supply sufficient force to enable the heat source stack to withstand the lateral G-loads during launch while the RTG fins are water-cooled. Once the Rover aeroshell is discarded after entry into the Martian atmosphere, the RTG is cooled radiatively for the balance of the mission.

When changing from water-cooling to radiation cooling, the RTG housing temperature rises about 100°C (on a summer day). This causes a differential growth of about 0.100" in the length of the high-expansion aluminum housing relative to the low-expansion graphite heat source stack, with a corresponding increase in the Belleville spring length and drop in spring force. In RTGs for other missions, the magnitude of the spring force is only important briefly during launch. In the case of the Rover RTG, the springs must still provide sufficient force after relaxation to hold the heat source together during Mars traverses for the balance of the four-year mission.

The structural analysis and design of the RTG consists of three principal tasks:

1. Determining how large a preload is required to hold the modules together during Earth launch and during Mars operations.

2. Designing the Belleville springs to supply the required spring force and spring travel.

3. Determining the stresses in the heat source modules, and designing the RTG housing to withstand the bending moments on the cantilevered RTG during launch, to be structurally stable against the one-atmosphere external pressure on earth, and to stay below the stresses where long-term creep would occur at the materials' operating temperatures.

These tasks are described in the next three sections.

6.2.3 Required Heat Source Preload Force: The heat source stack may be viewed as a partitioned beam with a distributed side load. If the beam were continuous rather than partitioned, the side load would produce axial compressive stresses on the side to which it is applied, and axial tensile stresses on the opposite side. But a partitioned beam cannot sustain a tensile stress in the axial direction. Therefore, in the absence of an axial preload, the side load would cause the partitioned beam to fall apart.

To hold the heat source stack together in the RTG, the axial preload must be high enough to equal or exceed the maximum axial tensile stress that would be produced by the side load if the beam were continuous rather than partitioned. When this principle was first applied [13], the authors mistakenly treated the GPHS module as though it were a solid block rather than a hollow box. This can lead to a serious overestimate of the required preload, as illustrated below.

Consider the simplified case of a hollow beam having a length L and cross-section bounded by an outer square of side a and concentric inner square of side b. The beam has fixed end supports and a uniform mass m' per unit length. It is subjected to a transverse g-load G and an axial compressive load P. The tensile stress σ in the beam at a distance c from the beam's neutral plane consists of two terms: the tensile stress due to the local bending moment M induced by the g-load, and the compressive stress due to the axial preload P,

$$\sigma = Mc/I - P/(a^2 - b^2) , \qquad (1)$$

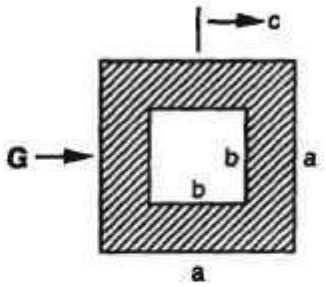

where I is its moment of inertia, given by

$$I = (a^4 - b^4)/12 . \qquad (2)$$

The distance c is a maximum at the beam's outer fibers,

$$c_{max} = a/2 \ . \tag{3}$$

and the bending moment M is a maximum at its axial ends and center,

$$M_{max} = m'GL^2/24 \ . \tag{4}$$

Thus, the maximum tensile stress in the beam is given by

$$\sigma_{max} = \frac{m'GL^2a}{4(a^4 - b^4)} - \frac{P}{a^2 - b^2} \ . \tag{5}$$

Since a partitioned beam cannot sustain a positive tensile stress, we set σ_{max} equal to zero to solve for the minimum required preload

$$P = \frac{m'G\,L^2/4a}{1 + (b/a)^2} \ . \tag{6}$$

Clearly, increasing the size of the cavity in the hollow beam decreases the required preload. Equation (6) shows that in the limit, as b approaches a, the required preload for the hollow beam is only half as large as that for a solid beam (b=0). This principle had been overlooked in Reference [13], but was recognized by Mr. Hamrick during the present study. It can make the difference between requiring or not requiring a midspan support.

The preceding derivation was for the idealized case of a simple hollow box beam. The actual modular heat source stack is more complicated. As shown in Figure 1, each module has top and bottom covers, and a curved cavity resulting in non-uniform side walls. To determine the required preload for such a modular stack, a detailed NASTRAN analysis was carried out, employing three-dimensional solids models of the modules' aeroshells and orthotropic properties of the carbon-carbon composite.

Figure 19 shows the undeformed grid model for half of the aeroshell of a single module. This and subsequent figures are sectioned at the plane of symmetry, the y-z plane. The appropriate number of such models were stacked up, linked to each other, and combined with models of the heat source support structure. The integrated model was then subjected to the axial spring load and to a side load of 25 G.

Figure 19. NASTRAN Model of GPHS Aeroshell

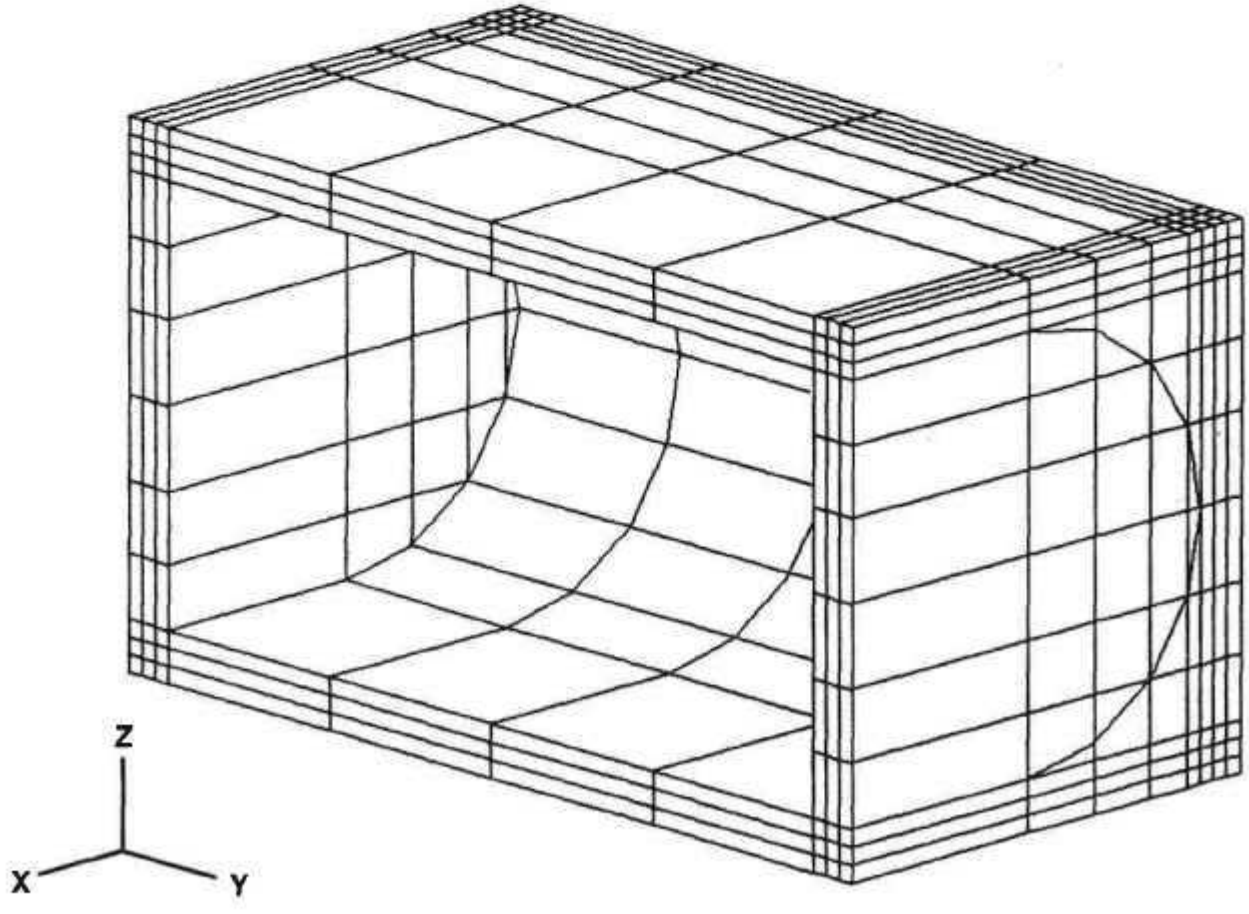

For a preliminary analysis, the heat source stack was analyzed without the effect of the simultaneous deformation of the cantilevered RTG housing. This simplification cuts the problem in half, because it results in identical end supports and symmetry about the heat source's midplane. Therefore, only half the heat source modules need to be modeled.

At the time of the preliminary analysis, we were considering a heat source of 16 instead of 18 modules. Therefore, our preliminary-analysis model consisted of eight heat source modules. The 16-module stack was subjected to a 4000-lb (18 kiloNewton) axial preload and a 25-G side load in the Y direction. The resultant deformation of the upper half of the 16-module stack is shown in Figure 20.

Figure 20. Deformation of Upper Half of Heat Source Stack Under 4000-lb Axial Load and 25G Side Load (Y)

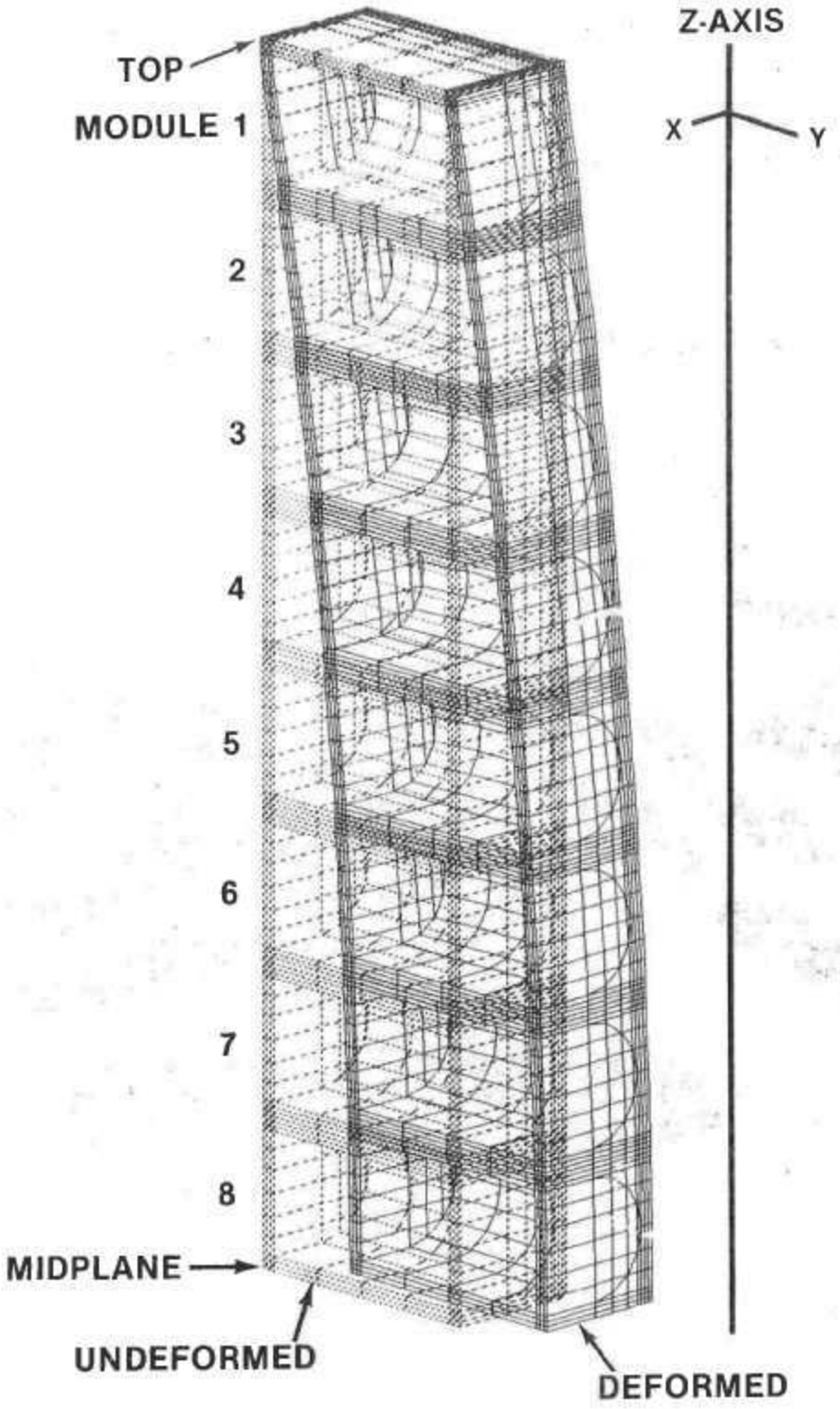

Computation of the normal Z-stresses in the heat source modules showed that all Z-stresses are negative (i.e., compressive) except for one small section in the upper left corner of Module #1. As shown in Figure 21, that corner exhibits a tensile stress of 0.53 ksi. It was therefore concluded that the basic principle illustrated by Eq. (6) had been confirmed, but that the predicted 4000-lb preload is slightly inadequate for the 16-module heat source. Based on these results, it was decided to use a 5500-lb preload for the 18-module heat source in subsequent analyses.

Figure 21. Normal Z-Stresses in End GPHS Modules (in ksi)

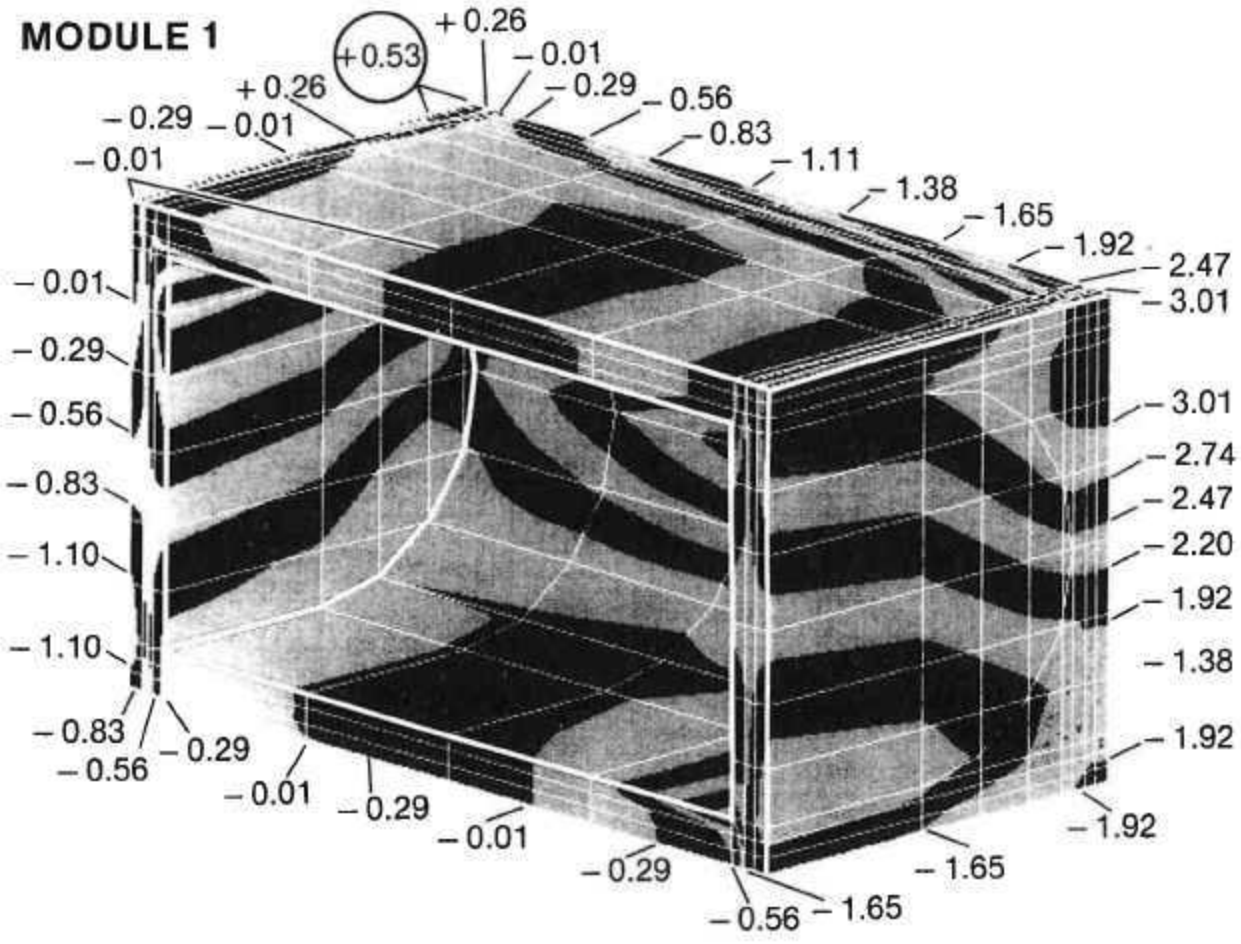

6.2.4 Designing the Belleville Springs: The Mars Rover RTG design differs from other RTGs in that a preload is required not just for a brief period during Earth launch, but also during atmospheric entry and landing on Mars and during Rover activities on Mars for the full four-year duration of the MRSR mission. Although the G-loads during these post-launch operations (15 G) are lower than during launch (25 G), one cannot assume that springs which satisfy the higher requirement will automatically satisfy the lower. This is so because the Rover RTG is water-cooled during Earth launch and radiation-cooled during and after Mars landing, as previously explained.

In switching from water-cooling to radiation-cooling, the RTG's housing temperature rises by about 100°C, causing its length to grow by about 0.1". Since the thermal expansion of the graphite heat source is virtually negligible, the thermal growth of the aluminum housing causes a corresponding expansion of the Belleville preload springs, and consequently a relaxation of the compressive load on the heat source stack.

Therefore, the designer must consider the adequacy of the spring force both during launch and during subsequent Martian operations, at their respective RTG temperatures. At the same time, he must make certain that the maximum stress in the spring material under maximum-load conditions does not exceed the spring material's strength at temperature. Thus, the spring design must satisfy three independent constraints.

Consider the general case of a set of N_p parallel (i.e., nested) Belleville springs and N_s such sets stacked in series. Each spring has an outer diameter D_o, inner diameter D_i, and thickness T. The springs are made of a material with elastic modulus E and Poisson's ration μ. The overall free height of each spring is H + T, and the deflection of each spring from its free height during Earth launch is Y_e. During Martian operations, the deflection of each spring from its free length is given by

$$Y_m = Y_e - \delta/N_s , \tag{7}$$

where δ is the thermal growth of the aluminum housing length due to the change from water cooling to radiation cooling.

The load P_e exerted by the springs during Earth launch is given by [14]

$$P_e = \frac{N_p E Y_e \left[(H - Y_e/2)(H - Y_e) T + T^3\right]}{(1 - \mu^2) C_0 (D_o/2)^2} , \tag{8}$$

the corresponding load P_m during Martian operations is given by

$$P_m = \frac{N_p E Y_m \left[(H - Y_m/2)(H - Y_m) T + T^3\right]}{(1 - \mu^2) C_0 (D_o/2)^2} , \tag{9}$$

and the maximum stress σ (at the inner diameter of the springs) is given by

$$\sigma = \frac{E Y_e \left[C_1 (H - Y_e/2) + C_2 T\right]}{(1 - \mu^2) C_0 (D_o/2)^2} , \tag{10}$$

where C_o, C_1 and C_2 are dimensionless geometric constants defined by:

$$C_0 \equiv \frac{6\,(1 - D_i/D_o)^2}{\pi\ \ln(D_o/D_i)}\ , \tag{11}$$

$$C_1 \equiv \frac{6}{\pi\ \ln(D_o/D_i)}\left[\frac{D_o/D_i - 1}{\ln(D_o/D_i)} - 1\right]\ ,\ \textit{and} \tag{12}$$

$$C_2 \equiv \frac{3\,(D_o/D_i - 1)}{\pi\ \ln(D_o/D_i)}\ . \tag{13}$$

Thus, given the values of N_p, N_s, D_o, D_i, P_e, P_m and δ, the spring design problem comes down to solving three simultaneous equations (8, 9, and 10) for the unknown spring dimensions T, H, and Y_e. Since these are simultaneous cubic equations, a trial-and-error solution is required. This was implemented by means of a Fairchild-generated computer program. The parameters used in the computations for the 18-module baseline RTG are summarized below:

$E = 11 \times 10^6$ psi	$\delta = 0.100$ in
$\mu = 0.31$	$\sigma = 82$ ksi
$P_e = 5500$ lb	$D_o = 8.75$ in
$P_m = 3300$ lb	$D_i = 3.20$ in

The spring's outer diameter D_o is designed to mate with the I.D. of the RTG housing, and its inner diameter D_i is designed to mate with the load ring to which the heat source support studs are bolted. Thus, the springs act as the radial support of the top of the heat source. (See Figures 14 and 15). To retain this benefit, an odd number was always picked for N_s, the number of springs (or nested springs) in series. Thus, the spring set is always loaded on the O.D. at the top and on the I.D. at the bottom.

For a given set of spring parameters, various combinations of N_s and N_p were tested. For some combinations, it was found that no physically real solution exists. But in general, there were several different combinations of N_s and N_p which satisfied the three equations and therefore the three constraints. For example, for the above parameters the equations are satisfied by the alternative solutions listed in Table 1.

Table 1. Spring Design Options Satisfying the Contraints on P_E, P_M, and σ

N_S	1	1	1	3	3	3	3	
N_P	3	4	5	1	2	3	4	
T	.221	.139	.088	.153	.061	.038	.028	inch
H	.230	.357	.414	.792	.896	.921	.933	inch
Y_E	.176	.161	.163	.076	.077	.077	.077	inch
Y_M	.076	.061	.063	.043	.044	.044	.044	inch

Each of the options listed in the table yields a preload of 5500 lbs on Earth, 3300 lbs on Mars, and a maximum stress of 82 ksi (at the spring's I.D.) Thus, any one of these options could be adopted. However, we preferred a single set of nested springs to a multiple stack, because it leads to a simpler and more compact RTG design.

Among the solutions for $N_s = 1$, we selected the one with the least number of springs, $N_s = 3$. Note that there is no physically real solution for $N_s = 1$ and $N_p = 1$ or 2. Thus, the spring design for the baseline RTG consists of three nested springs, with each spring having a thickness T of 0.221″, a free height H + T of 0.451″, and a compressed height ($H + T - Y_e$) of 0.275″ during Earth launch and ($H + T - Y_m$) of 0.375″ during Mars operations.

6.2.5 Von-Mises and Shear Stresses in Heat Source: The same solids model shown in Figure 19 was used to compute the von Mises stresses in the modules. The maximum was found to occur in Module 1. Figure 22 shows the von-Mises stresses in that module.

Figure 22. Von Mises Stresses in Module 1 (in ksi)

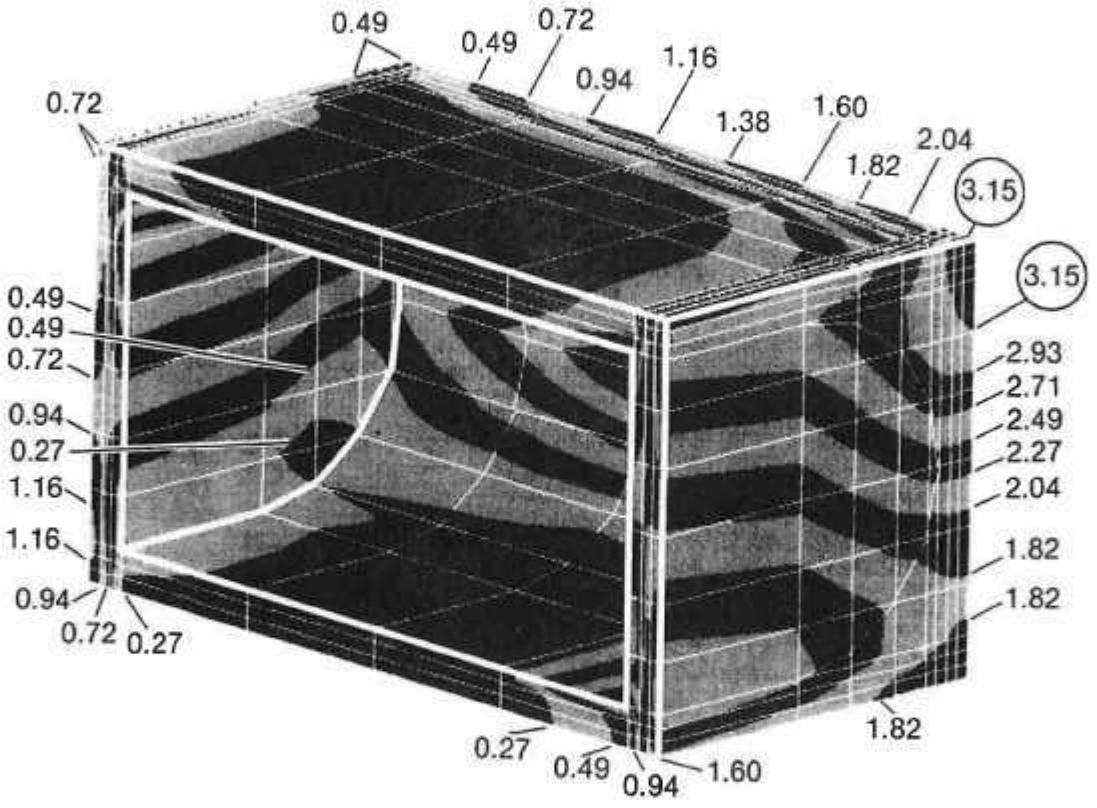

As can be seen, the maximum von-Mises stress, in the upper right corner of Module # 1, is 3.15 ksi.

Table 2 presents the strength of the Fine-Weave Pierced Fabric (FWPF) graphite material, as reported by its manufacturer (AVCO).

Table 2. Composite Strength (ksi) of AVCO Fine-Weave Pierced Fabric

TEMPERATURE:	°F	75	600	1000	2000	3000	4000	5000
	°C	24	316	537	1093	1649	2204	2760
TENSION:	Y	17.74	19.66	20.66	23.86	26.21	27.39	25.20
	X	17.64	19.66	20.66	23.86	26.21	27.38	25.20
	Z	18.17	20.24	21.28	24.57	26.99	28.20	25.95
COMPRESSION:	Y	20.61	20.78	20.85	21.59	23.56	26.49	30.61
	X	20.61	20.78	20.85	21.59	23.56	26.49	30.61
	Z	20.8	21.0	21.11	21.89	23.89	26.66	31.00
SHEAR:	YZ	1.17	1.11	1.07	1.00	0.99	1.26	1.00
	ZX	1.17	1.11	1.07	1.00	0.99	1.26	1.00
	XY	1.17	1.11	1.07	1.00	0.99	1.26	1.00

As can be seen, the previously computed maximum von Mises stress of 3.15 ksi is only 15% of the materials' tensile and compressive strength.

Table 2 shows that FWPF is much weaker in shear than in tension or compression. Therefore, the xy, xz, and yz shear stresses were computed. The maximum shear stress was found to be the yz-stress in Module 1. As shown in Figure 23, the maximum shear stress is 0.138 ksi. This is only 14% of the material's shear strength shown in Table 2.

Figure 23. YZ-Shear Stresses in Module 1 (in ksi)

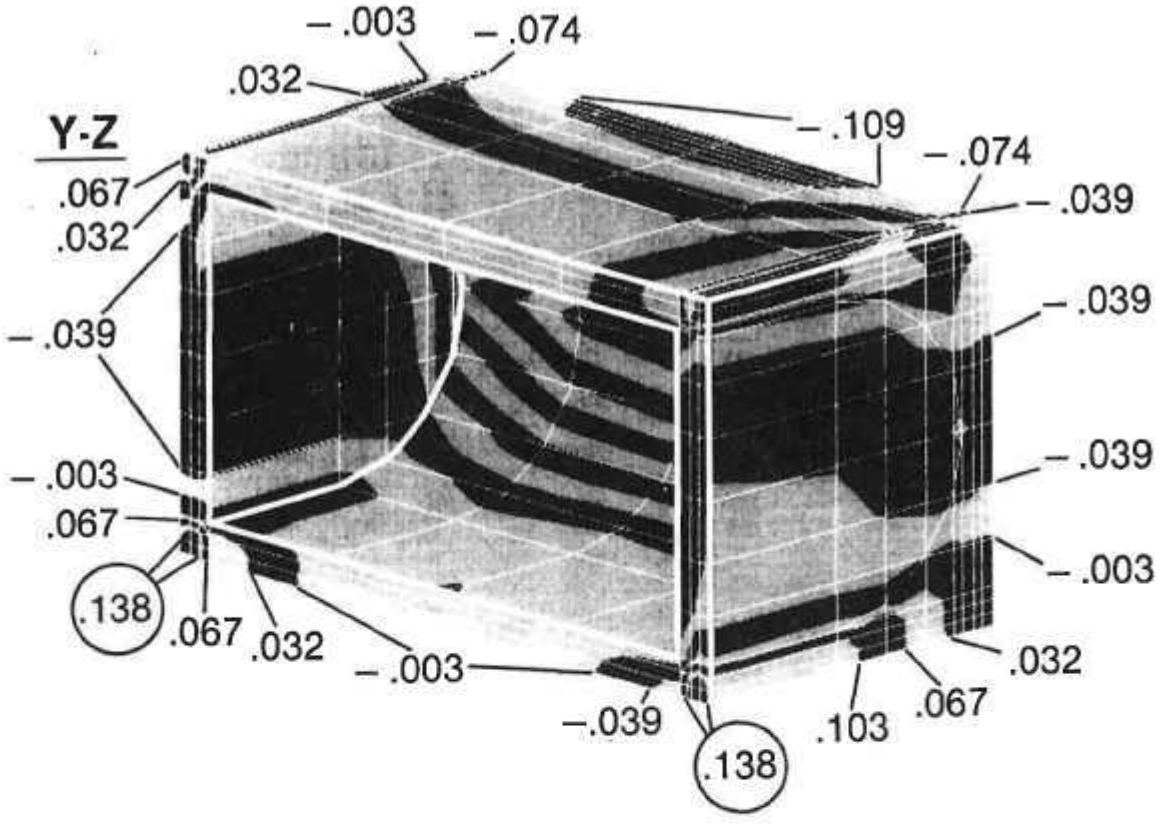

6.2.6 Deformation and Stresses in Full RTG: The preliminary structural analysis described thus far employed a simplified analytical model. The model did not include the RTG housing, which supports the load springs that compress the heat source stack. Instead, the load springs were assumed to have symmetrical fixed-end supports. Because of that symmetry, only half the heat source stack needed to be modeled.

The more complete analysis described in this section did not employ these simplifications. The heat source was supported by the deformable RTG housing. Specifically, the upper springs were connected to the top of the housing side wall, and the lower heat source support studs were mounted on the housing baseplate.

The model of the housing included the fin roots and cooling ducts which act as stiffeners. It also included the radial and circumferential stiffeners of the baseplate. The housing was cantilevered, with only the rim of its baseplate fixed and the rest of the housing free to lean away from the 25-G side load. The resultant angular deflection of the RTG's upper end, shown in Figure 24, results in highly unsymmetrical heat source supports. Therefore, it was necessary to model the whole 18-module heat source.

Figure 24. Deformation of Cantilevered RTG Housing Under 25G Side Load

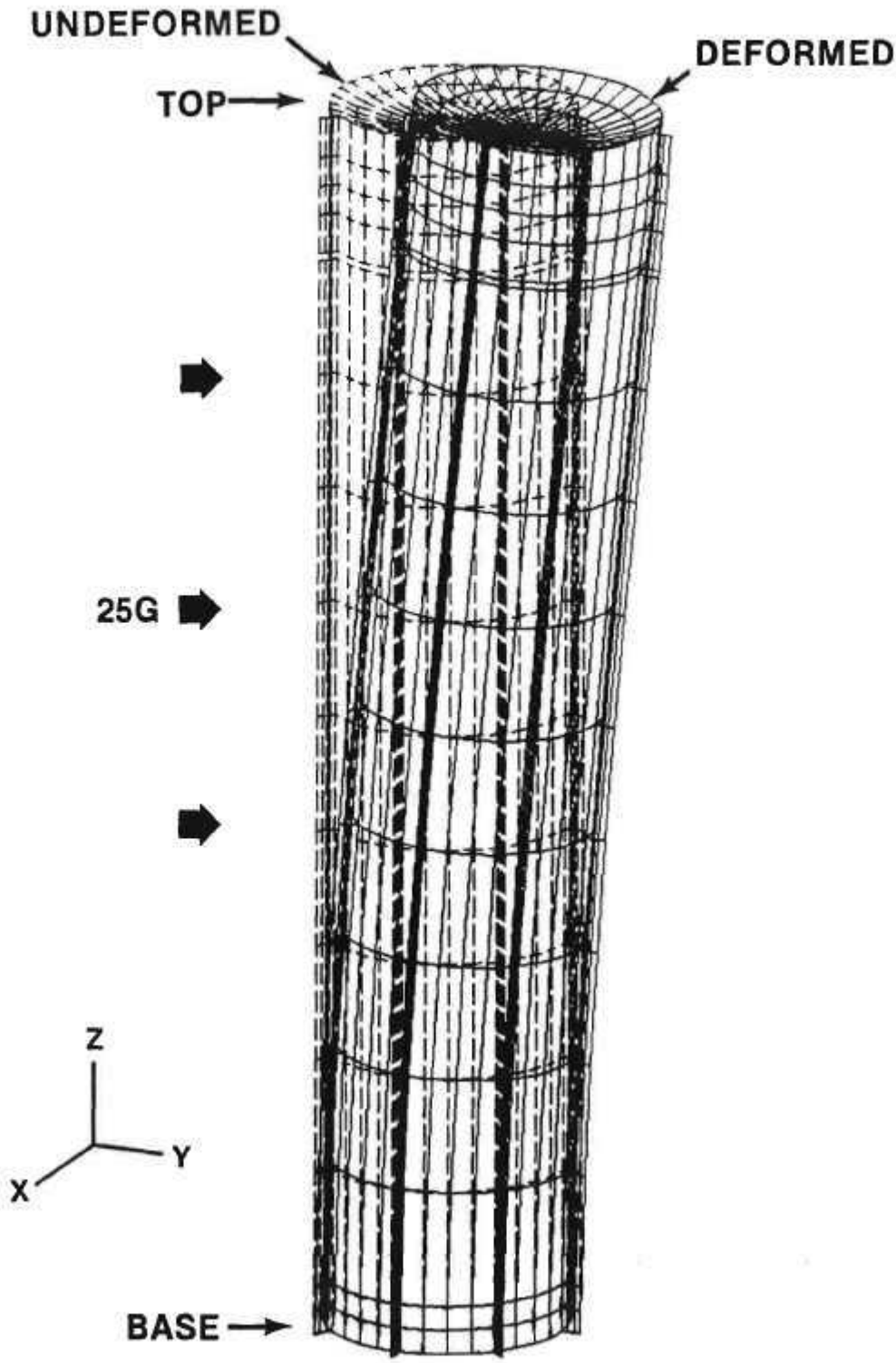

The solids model used for the preliminary analysis of the eight-module half-stack had 10,961 grid points and 26,652 degrees of freedom. Using a similar solids model for the full eighteen-module heat source would have exceeded the available computer time and disk space. To avoid that, the solids model was replaced with a plate model having an equivalent stiffness matrix. Even so, a very large (2140-node) NASTRAN model with 10,611 degrees of freedom was required to represent the heat source, its support structure, and the RTG housing.

Figure 25 depicts the model of the RTG in its undeformed and deformed shapes. The deformation shown includes the effects of the 25-G side load and of the 5500-lb spring force, which produces a compressive load on the heat source stack and a tensile load on the housing.

The deformations shown have, of course, been exaggerated for improved visibility. Note the leaning of the housing and the bowing of the heat source in the y-direction, the axial elongation of the housing due to its tensile load, and the outbowing of the RTG's baseplate due to the downward force exerted by the heat source.

Figure 25. Deformation of Spring-Loaded Heat Source Supported by Cantilevered RTG Housing

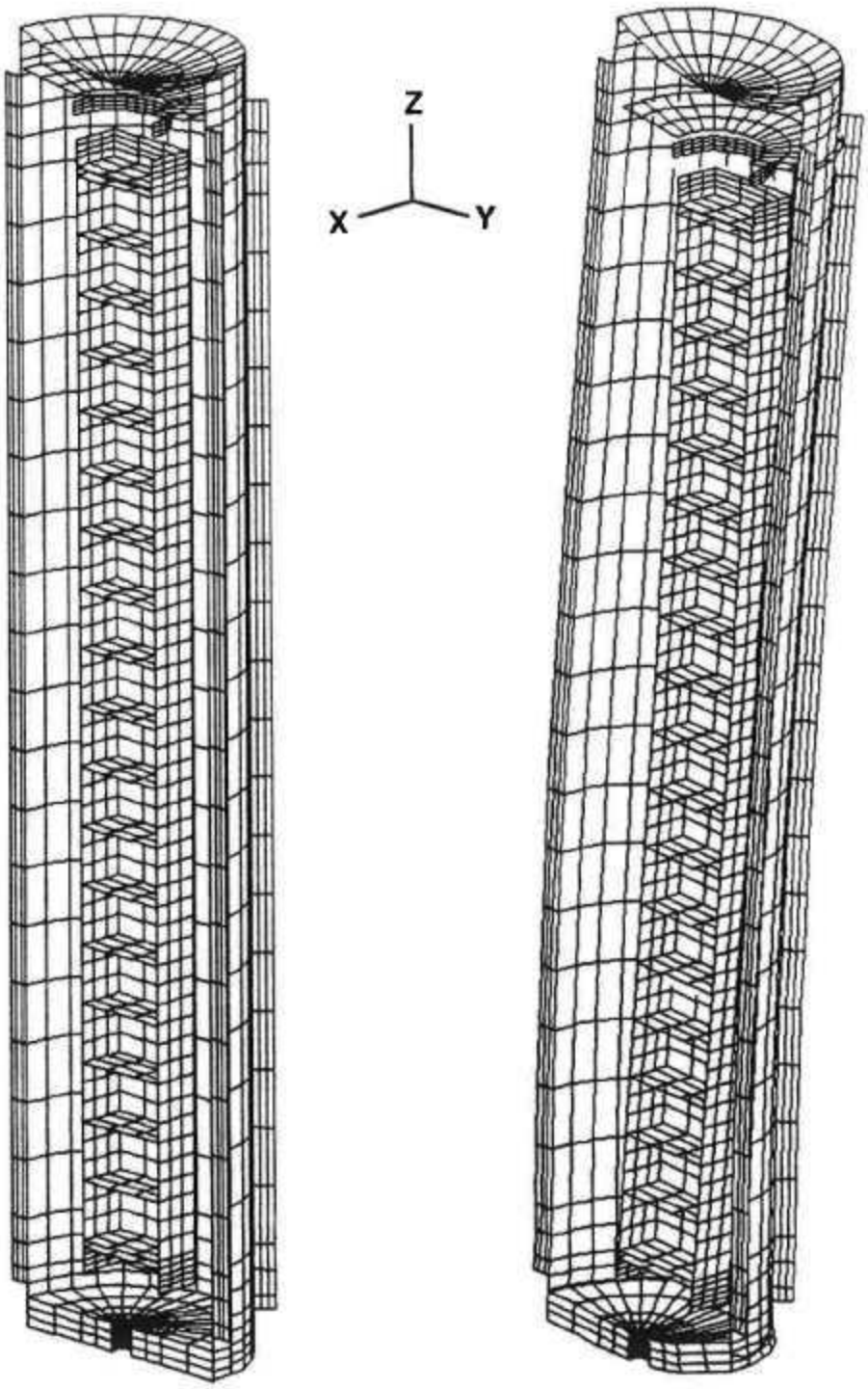

Figure 26 presents the normal-Z stresses and von Mises stresses in the heat source side walls. As can be seen, all of the normal-Z stresses are negative. The highest (i.e., least negative) Z-stress is -1.09 ksi, well within the compressive regime. The computed results suggest that the 5500-lb preload can probably be reduced to 5000-lbs without developing any tensile Z-stresses.

The right half of the figure shows that the maximum von Mises stress, 2.9 ksi, is again far below the strength limit of the FWPF graphite material. (See Table 2.)

Figure 26. Stresses in Heat Source Aeroshells (ksi)

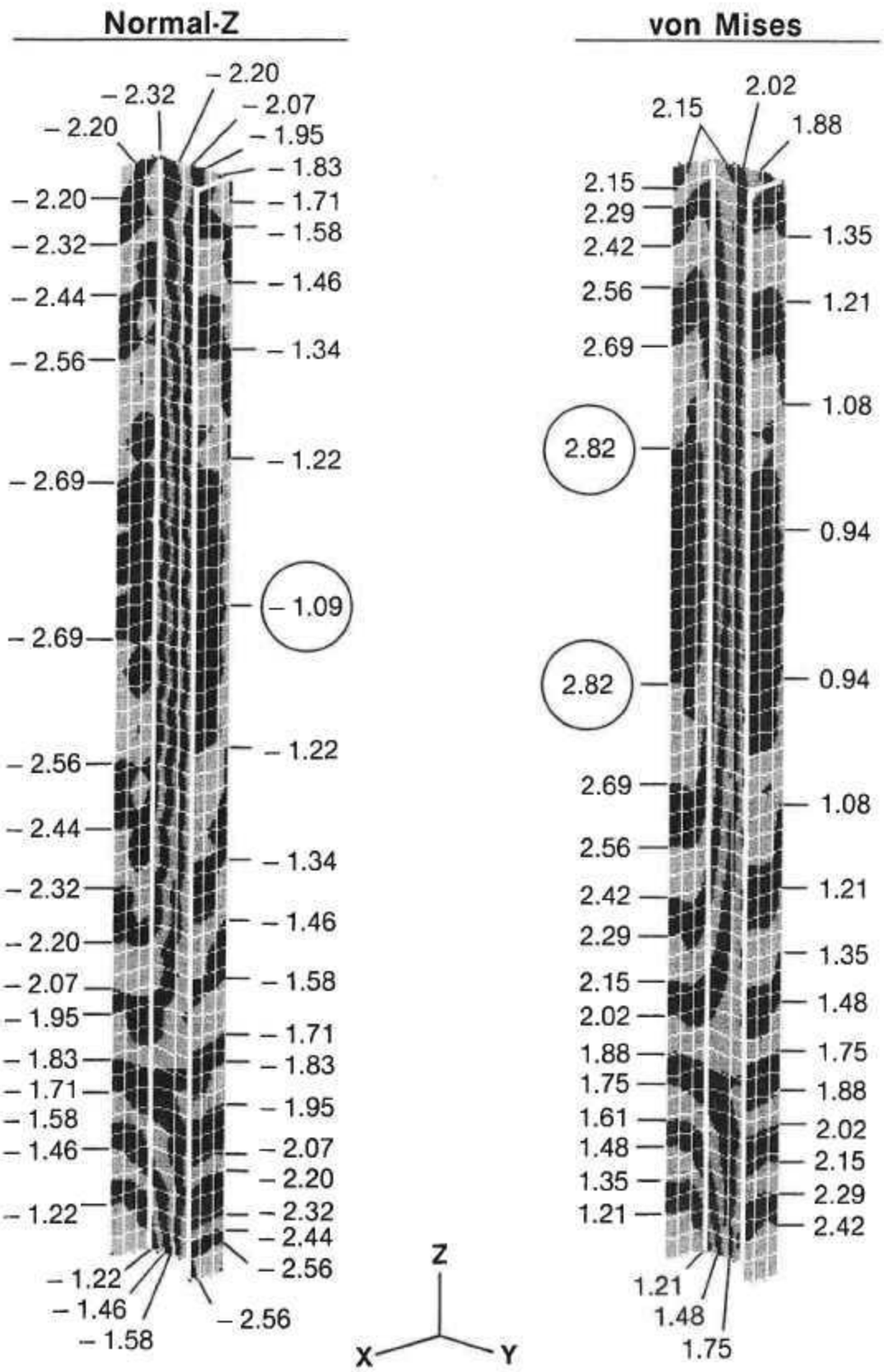

Figure 27 depicts the corresponding von Mises stress distribution in the RTG housing side wall. Two conditions are illustrated: The left half of the figure shows the short-term launch stresses of the water-cooled RTG housing with a 5500-lb spring load and a 25-G side load. The right half of the figure shows the long-term stresses of the radiation-cooled RTG with a 3300-lb spring load and a 15-G side load.

The maximum launch stress, which occurs at the -y side near the base of the RTG, is ~15 ksi. This is well below the 31-ksi yield strength of the aluminum alloy (2219 T851) at its 171°C launch temperature. Similarly, the maximum stress on Mars, 8.5 ksi, is only 53% of the alloy's 16-ksi yield strength at its 272°C maximum operating temperature.

In addition to yield strength, the long-term creep characteristics of the aluminum housing must be considered. The RTG housing, at its thinnest (0.090") section, has a horizontal cross-section of 2.54 in^2. Thus, at its maximum operating temperature, the 3300-lb spring load will produce a steady-state tensile stress of 1.3 ksi. Even if the housing were constantly at its maximum operating Martian temperature of 272°C, this tensile stress would produce only negligible creep during the four-year mission.

Figure 27. Von Mises Stresses in Housing Side Wall (ksi)

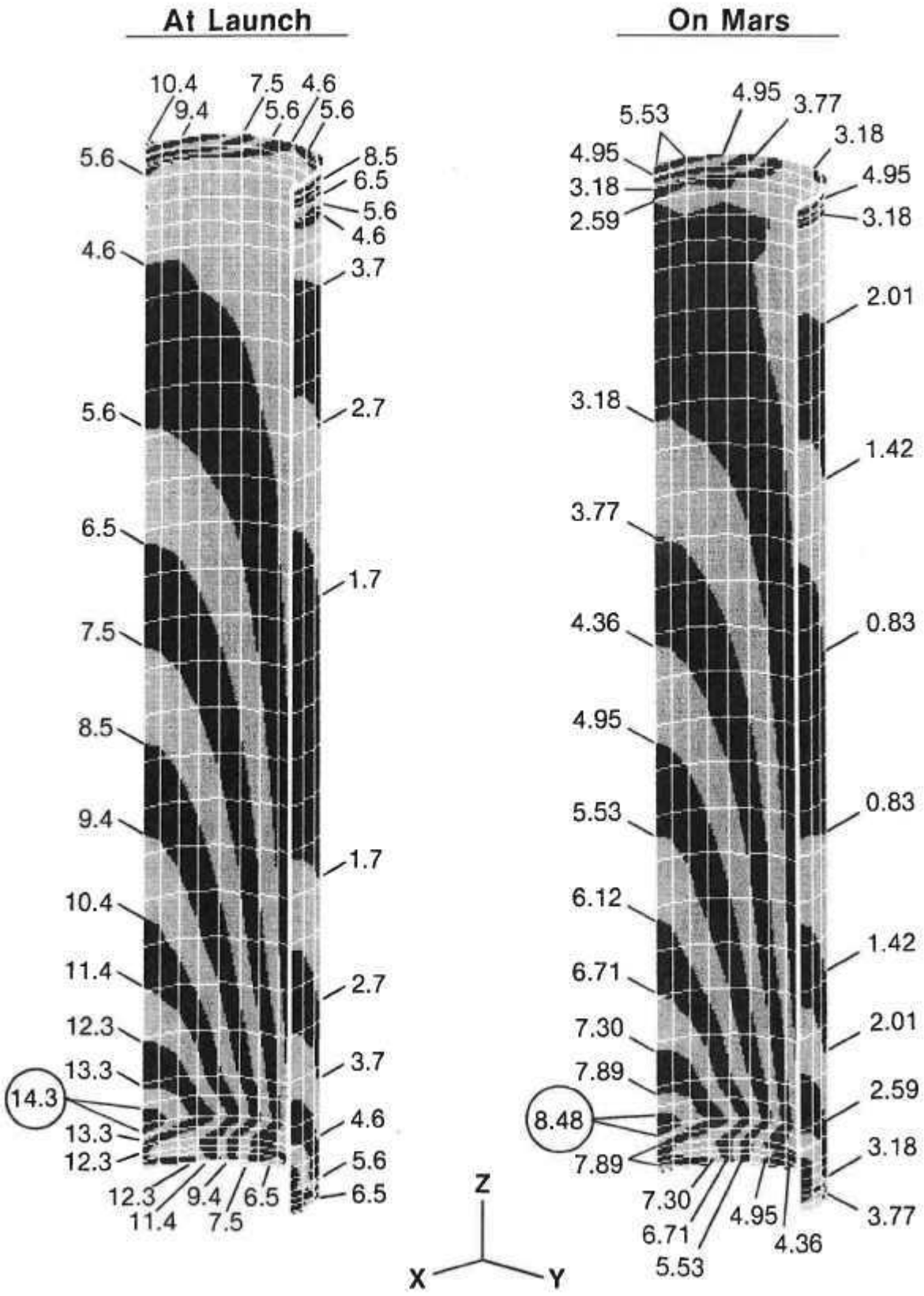

Finally, Figure 28 shows the von Mises stress distributions in the RTG's 0.062″-thick top cap and in its 0.125″-thick baseplate. Before launch, the top cap is subjected to an external pressure of one atmosphere. Its maximum stress, ~5 ksi, is well below the strength of aluminum.

The heavy white lines in the baseplate stress plot show the location of the eight radial and three circumferential stiffening ribs, which are 0.25″ thick and 1″ high. The two white dots in the figure denote the locations of the heat source support studs. As can be seen, the maximum launch stress (18 ksi) occurs at the +y side of the inner stiffening ring. A secondary maximum (14 ksi) occurs at the right side of the middle stiffener ring. This location is directly below one of the two support studs at the +y side of the heat source. The maximum baseplate stress is 42% below the 31-ksi yield strength of the aluminum alloy at its 171°C launch temperature.

Thus, detailed NASTRAN analysis of the spring-loaded heat source supported by the cantilevered RTG housing confirms the feasibility of supporting an 18-module heat source stack without midspan supports, and demonstrates the adequacy of the spring and housing dimensions on which the mass analyses in the next section are based.

Figure 28. Von Mises Stresses in RTG Top Cover and Base Plate

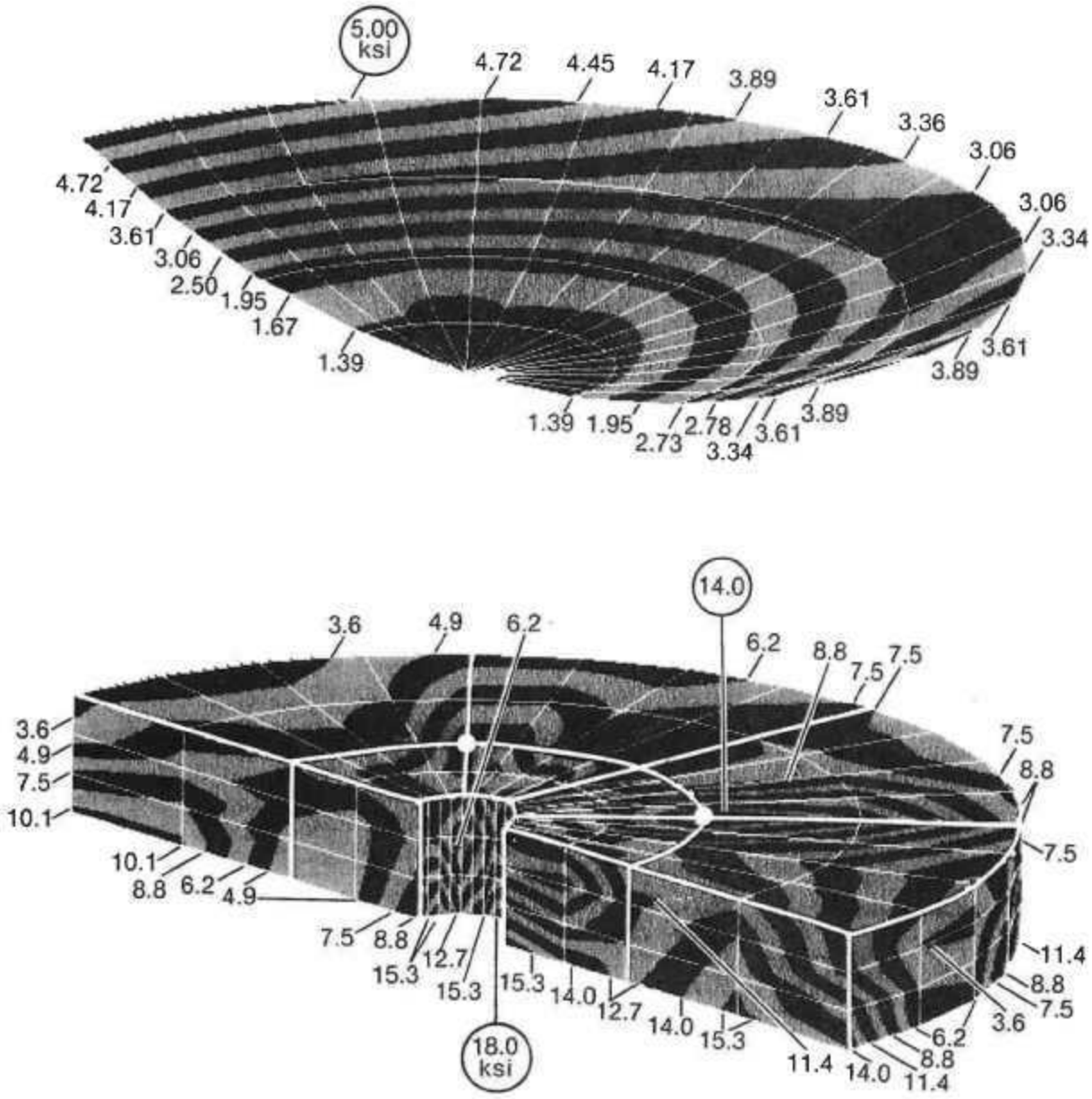

6.3 MASS BREAKDOWN

The mass breakdown of the "baseline" Mars Rover RTG, depicted in Figure 18, is presented in the left half of Table 3. The right half of the table shows the corresponding breakdown for the existing Galileo RTG, to ensure that all required components of the Rover RTG have been properly accounted.

The left column of Table 3 shows that the baseline RTG has a total mass of 58.7 kg. As shown, most (58%) of that mass is in the heat source rather than the converter, and most of that (77%) resides in the heat source modules. It is also noteworthy that the heat source canister, which enables operation of the RTG in the Martian atmosphere, has a mass of 3.8 kg.

The right half of Table 3 shows the corresponding mass breakdown for the existing Galileo RTGs. As seen, the baseline Rover RTG, with its non-optimized radiator fins, is 4.6% heavier than the Galileo RTG. Most of that difference (3.77 kg) is due to the canister needed for Mars operations. The other subsystems have very similar masses in the two RTGs.

Table 3. Mass of Baseline RTG Versus Galileo RTG

RTG MASS BREAKDOWN (kg)	ROVER RTG BASELINE DESIGN		GALILEO RTG	
HEAT SOURCE (33.8/30.1kg)				
GPHS MODULES (18/18)		26.05		26.05
FUEL (PuO_2)	10.73		10.73	
CAPSULES (Ir)	4.21		4.21	
GRAPHITICS	11.11		11.11	
H.S. CANISTER (Mo)		3.77		0.00
SIDE WALLS	2.21		----	
BELLOWS	0.11		----	
END CAPS AND LOAD SPREADERS	1.45		----	
H.S.STRUCTURAL SUPPORTS		3.94		4.05
GRAPHITE PRESSURE PLATES	0.52		0.53	
LOAD STUDS+ZIRCONIA	0.27		0.38	
BELLEVILLE SPRINGS (Ti)	2.31		0.51	
OTHER PRELOAD HARDWARE	0.84		1.69	
MID-SPAN SUPPORT ASSEMBLY	----		0.94	
CONVERTER (24.9/26.0kg)				
ELECTRICAL CIRCUITS		7.74		7.65
TE ELEMENTS (576/572)	5.43		5.40	
TE FASTENERS AND SEALS	1.09		1.08	
ALUMINA INSULATORS	0.88		0.88	
ELECTR. CONNECTORS +TERMINALS	0.34		0.29	
MULTIFOIL INSULATION (Mo/Quartz)		5.94		7.16
SIDES	5.26		5.52	
ENDS	0.68		0.55	
SUPPORT STRUCTURE	----		1.09	
RTG HOUSING (Al)		8.45		8.17
SIDE WALL (0.090"/0.060")	7.01		6.47	
COVERS & BOLTS	0.98		0.81	
RESISTANCE THERMOMETER	0.30		0.30	
GAS MGMT. ASSEMBLY	0.16		0.16	
PRESSURE RELEASE DEVICE	----		0.43	
RADIATOR		2.78		3.00
FINS (8/8)	2.38		1.96	
AUXILIARY COOLANT MANIFOLDS	0.25		0.26	
EMISSIVITY COATING	0.15		0.15	
MISCELLANEOUS ELEMENTS	----		0.63	
TOTAL RTG MASS (kg)		**58.67**		**56.08**

6.4 THERMAL AND ELECTRICAL ANALYSIS FOR BASE CASE

The analysis described in this section consists of three parts (thermal, thermoelectric, and electrical), which must be performed simultaneously and interactively. The analysis uses specialized computer codes generated by Fairchild to compute the heat flows, temperatures, and electrical parameters of each layer of thermoelectric elements. Inputs include the RTG design, the thermal input power (BOM/EOM), the cooling mode (water/radiation, Mars environment), the TE materials and performance, and the desired electrical output voltage.

The required analysis cannot be carried out by a standard thermal analysis code, because the thermoelectric unicouple is not a simple heat conductor. The heat input rate Q_h at the couple's hot junction does not equal the heat rejection rate Q_c at its cold junction, since part of the input energy is converted into electrical power P.

6.4.1 Thermoelectric Analysis: The critical material properties of a thermoelectric couple are the temperature-dependent Seebeck coefficient S', thermal conductivity k', and electrical resistivity ρ' of its n- and p-legs. The first step in the analysis is to use these to compute the temperature-averaged values [15]:

$$S = \int_{T_c}^{T_h} (S_n' + S_p') \, dT / \Delta T \quad , \tag{14}$$

$$k_n = \int_{T_c}^{T_h} k_n' \, dT / \Delta T \quad , \tag{15}$$

$$k_p = \int_{T_c}^{T_h} k_p' \, dT / \Delta T \quad , \tag{16}$$

$$\rho_n = \int_{T_c}^{T_h} \beta \, k_n' \, \rho_n' \, dT / k_n \, \Delta T \quad , \text{ and} \tag{17}$$

$$\rho_p = \int_{T_c}^{T_h} \beta \, k_p' \, \rho_p' \, dT / k_p \, \Delta T \quad , \tag{18}$$

where T_h and T_c are the couple's hot- and cold-junction temperatures, ΔT is the difference between them, and the factor β accounts for the resistances of the contacts and the electrodes. Based on measured contact resistivities and calculated electrode resistances, a value of 1.10 was used for the β of standard-size unicouples.

A thermoelectric couple with n- and p-legs of length L and cross-sectional areas A_n and A_p has a thermal conductance

$$K = [k_n A_n + k_p A_p] / L \tag{19}$$

and an electrical resistance

$$R = [\rho_n / A_n + \rho_p / A_p] L . \tag{20}$$

If the couple operates at a current I, the heat input rate Q_h at its hot junction is given by

$$Q_h = K\Delta T + I S_h T_h - I^2 R/2 - I\mu\Delta T/2 , \tag{21}$$

where the first term represents the zero-current heat conduction, the second term is the Peltier cooling rate of the hot junction, the third term represents one half of the ohmic heat dissipation rate in the couple, and the fourth term is the Thomson effect. The Thomson coefficient μ' is defined by

$$\mu' \equiv T(dS'/dT) \tag{22}$$

and its temperature-averaged value μ is given by

$$\mu = \int_{T_c}^{T_h} T(dS'/dT)\, dT / \Delta T = \int_{S_c}^{S_h} T\, dS' / \Delta T. \tag{23}$$

Following Raag [15], we employ differentiation by parts to obtain

$$\int_{S_c}^{S_h} T\, dS' = S_h T_h - S_c T_c - \int_{T_c}^{T_h} S' dT . \tag{24}$$

Combining Eqs. (14), (23), and (24), we obtain

$$\mu = (S_h T_h - S_c T_c) / \Delta T - S , \tag{25}$$

so that Eq. (21) can be expressed as

$$Q_h = K\Delta T + IS_h T_h - I^2 R/2 - I(S_h T_h - S_c T_c - S\Delta T)/2 . \tag{26}$$

Similarly, the heat rejection rate Q_c at the couple's cold end is made up of the corresponding conduction, Peltier, Ohmic, and Thomson terms:

$$Q_c = K\Delta T + IS_c T_c + I^2 R/2 - I(S_h T_h - S_c T_c - S\Delta T)/2 . \tag{27}$$

Subtracting Eq. (27) from (26), we obtain

$$Q_h - Q_c = IS\Delta T - I^2 R. \tag{28}$$

The couple's output voltage V equals the difference between its open-circuit voltage SΔT and its internal voltage drop IR:

$$V = S\Delta T - I R. \tag{29}$$

Eliminating SΔT between Eqs. (28) and (29), we obtain

$$Q_h - Q_c = I V , \tag{30}$$

which is consistent with the fact that the difference between the couple's heat input and output rates must equal its electrical power output.

The preceding equations and the resultant energy balance are summarized in Figure 29. Clearly, the couples are not simple heat conductors, except in the open-circuit case of zero current. Since the Peltier effect, Ohmic effect, and Thomson effect are all functions of the couple's current, the thermal analysis of the RTG can only be carried out in conjunction with its electrical analysis.

Figure 29. Unicouple Energy Balance

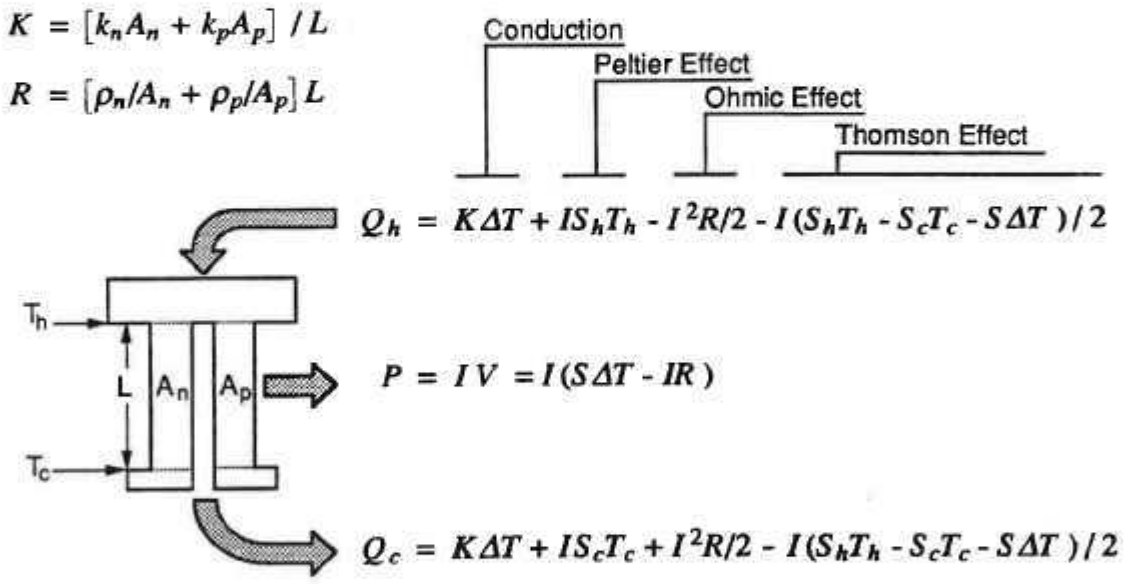

6.4.2 Specialized Computer Code: To apply the above equations, an existing thermal analysis code (SINDA) was modified to include the effects of Peltier cooling and heating and of ohmic heat generation, and to account for the energy converted to electrical power. The Fairchild-generated code also accounts for ohmic heating in the electrodes and inter-couple leads, and for heat losses through the multifoil insulation and the quartz yarn wrapped around the couple legs. The code simultaneously carries out the electrical analysis for each couple in the RTG, including the effects of measured contact resistances and ohmic losses in legs, electrodes, and leads; experimentally determined effects of long-term material degradation of SiGe; and optimized n/p leg area ratios. Other constraints applied are that all TE elements grouped in parallel must operate at the same voltage, and all groups in series must have the same current.

The analysis used temperature-dependent values of the Seebeck coefficient, electrical resistivity, and thermal conductivity for the SiGe n and p legs. Temperature-averaged properties were computed for each unicouple layer for each iteration of the analysis. The temperature-averaged figure of merit (Z) of the couple is defined by Eq. (40) on page 117. For the SiGe unicouples at the center of the baseline RTG, the analysis yielded a value of 0.000583 K^{-1} at BOM and 0.000548 K^{-1} at EOM. The thermal and electrical results were used to compute the material efficiency, couple efficiency, and converter efficiency of each layer of TE elements, and the overall RTG system efficiency.

The thermal analysis of the baseline design was based on an assumed RTG housing wall thickness of 0.090″ and eight radiator fins of a trapezoidal cross-section, with a fin root thickness of 0.060″, a fin tip thickness of 0.015″, a root-to-tip fin height of 3.0″, and a housing and fin emissivity of 0.85. The fins had an axial length of 42.7″. Thus, they extended 2.5″ beyond each end of the active thermoelectric zone. The Belleville spring dimensions used were based on the results of the structural analyses described earlier.

Figure 30 depicts the flow chart of the Fairchild's Thermal-Thermoelectric-Electrical Analysis code (TTEEA). As can be seen, it consists of three nested loops. The analysis starts with initial guesses for the RTG's temperatures T_o, current I_o, and couple area A_o. The thermoelectric subroutine then applies Equations (14) through (20), (26), and (27) to compute the heat input Q_h and output Q_c of each layer of couples in the RTG. These values are then fed into the thermal analysis subroutine, which calculates a new set of RTG temperatures. This inner loop is repeated until the temperatures have converged.

Next, the electrical analysis subroutine is used to compute the voltage of each couple and the output voltage V of the whole RTG. If it has not converged to the desired 30-volt output, the middle loop is repeated with adjusted values of the current I until convergence is achieved.

For the BOM case, the code then searches for the maximum hot-junction temperature T_{max} and repeats the outer loop with adjusted values of the couple area A until T_{max} converges to the design goal of 1000°C. For the EOM case, the outer loop is omitted because the area A has been previously fixed by the BOM analysis.

The Fairchild-generated code was used to carry out the coupled thermal, thermoelectrical, and electrical analyses of the RTGs. A 425-node model of the axisymmetric RTG was used to compute the axial variation of the temperatures of the various RTG components. That axial variation is appreciable, because of unavoidable end losses through the structural supports at the top and bottom of the heat source stack.

Figure 30. Thermal-Thermoelectric-Electrical Analysis Code (TTEEA)

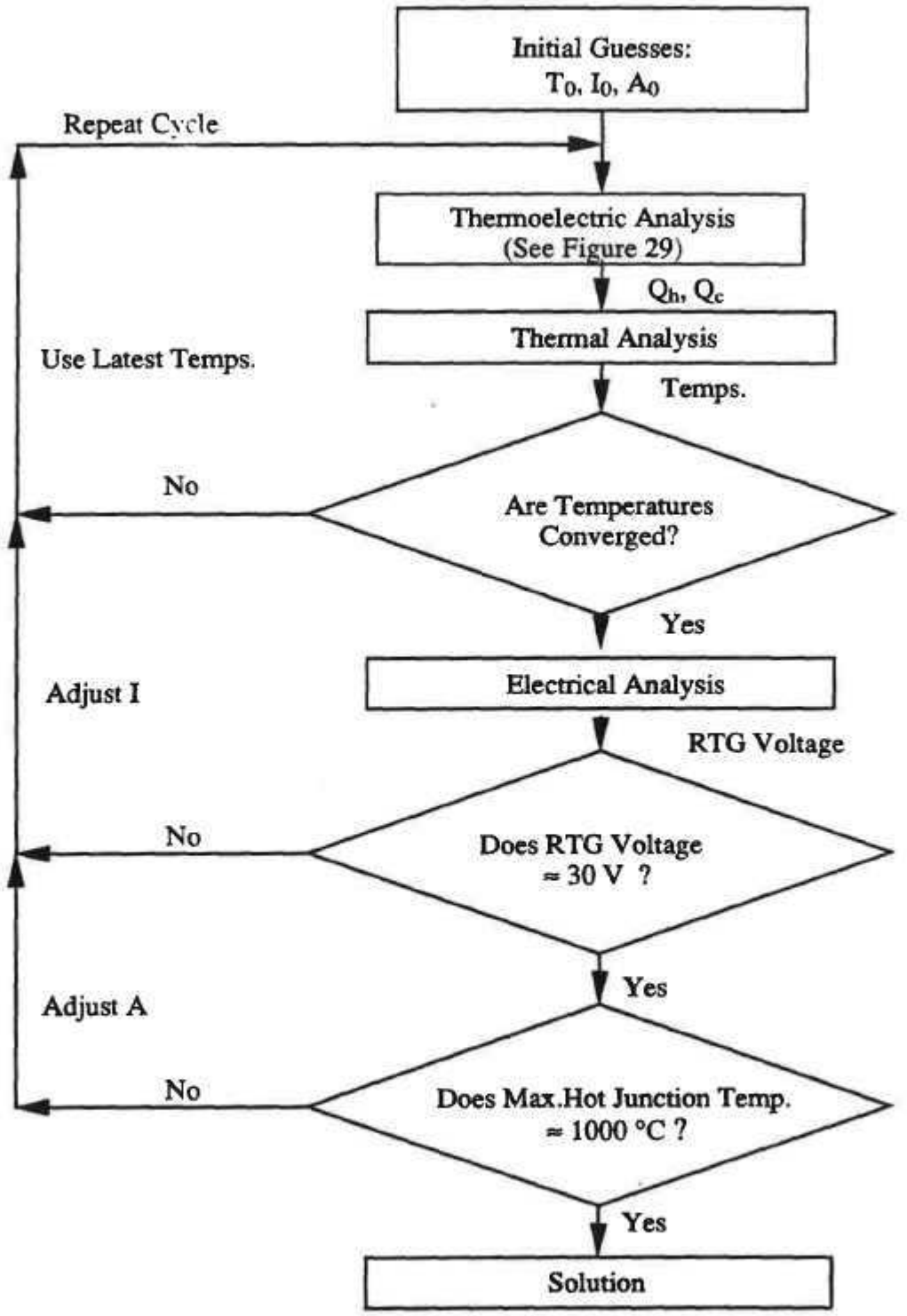

6.4.3 Temperature Distribution: Figure 31 shows the BOM temperature distribution (in ^{o}C) of the radiation-cooled baseline RTG for a 300^{o}K sink temperature. It shows the temperatures of the RTG end regions, and the temperatures at the center of the RTG. The temperatures shown are for an RTG with unicouples of standard dimensions, except that the cross-sectional areas of their SiGe legs have been reduced by 9% from the corresponding values in the Galileo RTG. This was done in order to take full advantage of the unicouples' maximum temperature capability.

The figure shows the maximum temperatures of the iridium capsules (1172^{o}C), the graphite heat source surface (1087^{o}C), the molybdenum canister (1058^{o}C), the SiGe hot junction (996^{o}C) and cold junction (293^{o}C). Of particular interest are the maximum temperatures of the zirconia insulators (1005^{o}C), the Inconel support studs (588^{o}C), the titanium springs (217^{o}C), and the aluminum housing (272^{o}C), since their mechanical properties and creep characteristics are strong functions of temperature. Note that the maximum hot-junction temperature does not exceed its established 1000^{o}C limit, and that the 1172^{o}C maximum capsule temperature is far below its established 1330^{o}C limit. The reason why the capsule temperature is much lower in the Mars Rover RTG than in the Galileo RTG is the presence of helium inside the canister. Helium greatly reduces the internal temperature drops in the heat source module.

To illustrate the approach used in the thermal, thermoelectric, and electrical analyses of the various RTG designs, the BOM results for the baseline RTG radiating to a 300^{o}K sink are presented in detail in Figures 32, 33, and 34. (Similar detailed results were generated for each design option and each environment investigated.)

Figure 31. BOM Temperature Distribution (°C) in Baseline RTG

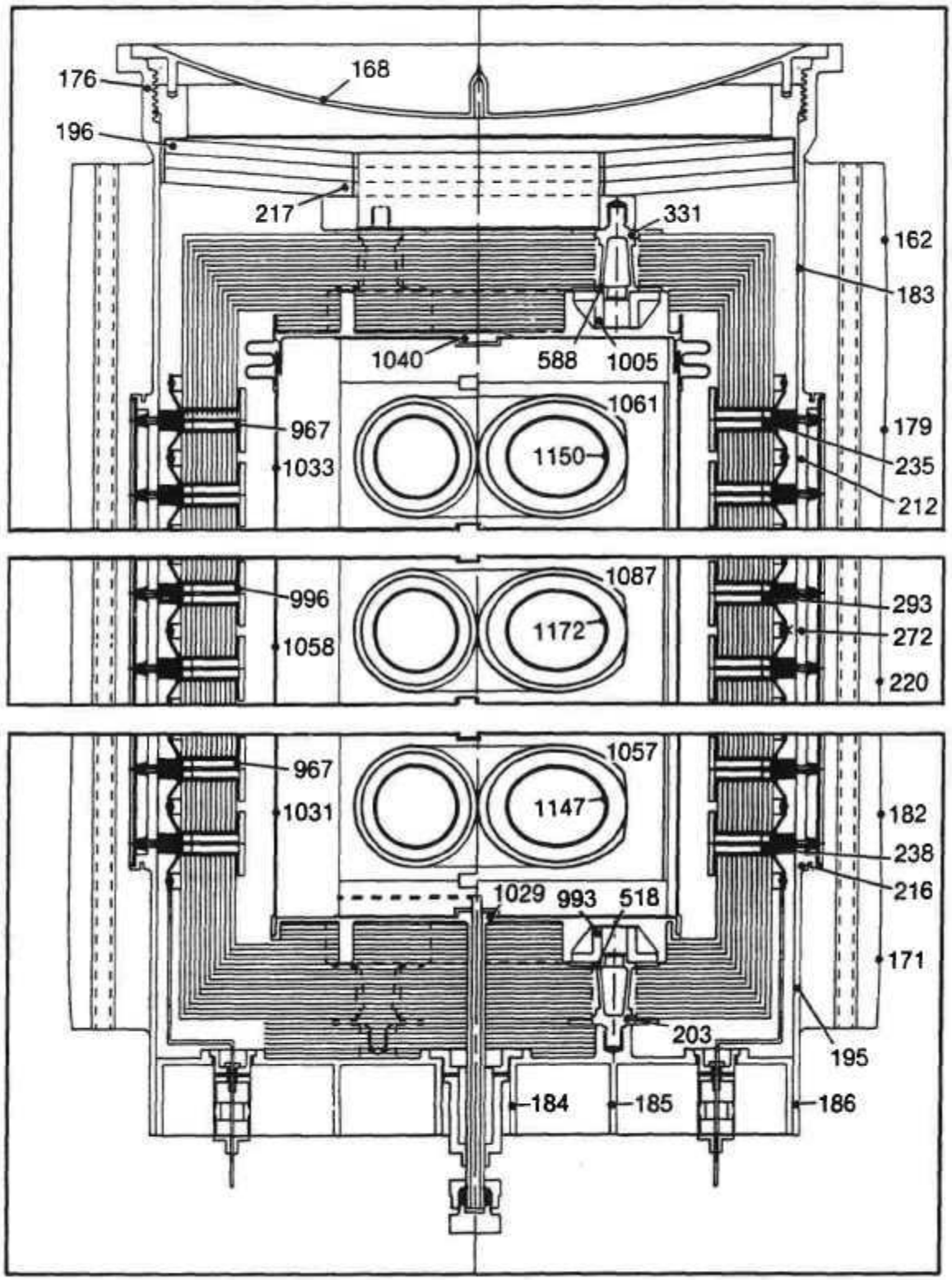

6.4.4. Axial Temperature Profiles: Figure 32 depicts the axial temperature variations in the RTG. The heat losses from the end of the heat source stack result in the depicted temperature profiles of the fuel capsule clads, the modules' aeroshell surfaces, the canister, and the unicouple hot junctions. The figure also shows the axial temperature variations of the cold junctions, the fin root, and the fin tip.

The figure shows six temperature drops between the various curves. The first (~85°C) represents the drops inside the heat source modules, across the graphitics and the helium gaps. The second (~29°C) is the drop across the helium gap to the canister, and the third (~62°C) is across the vacuum gaps and through the TE heat collectors. The fourth (701 to 727°C) is the temperature drop across the SiGe TE legs. As can be seen, this is the largest of the drops. It is the only one that makes a useful contribution in actually generating electrical power. All the other temperature drops represent thermodynamic losses. The fifth drop (~29°C) represents the thermal resistance of the unicouple's cold-end and the loss for circumferential heat transport through the aluminum housing to the nearest fin; and the sixth drop (44°C) is that due to radial heat flow through the fin itself.

The depicted variation of the hot-junction temperatures would result in a significant performance loss, were it not balanced by a similar convex profile of the cold-junction temperatures. This was achieved by extending the radiator fins beyond the active length of the RTG, as mentioned earlier. In fact, the temperature drop-off of the cold junctions near the RTG ends is greater than that of the hot junctions. This explains why the unicouples' heat flow rates, power outputs, and efficiencies are actually higher at the ends of the RTG than at the center, as shown in Figures 33 and 34.

Figure 32. Axial Temperature Profiles (°C)

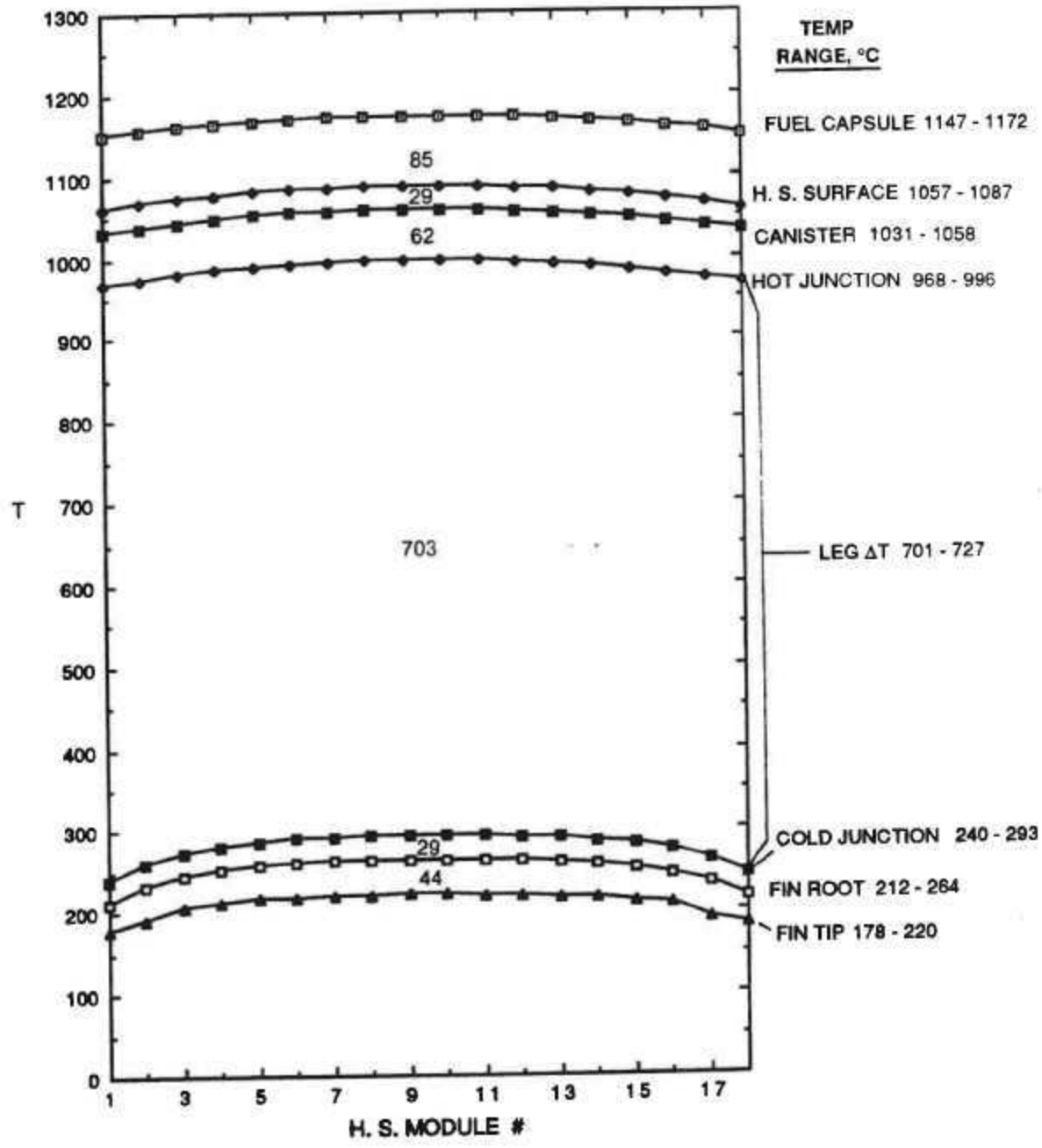

6.4.5 Axial Variation of Heat Flow Rates: The BOM temperatures shown in Figure 32 result in the axial variation of heat flow rates to and from each ring of thermoelectric unicouples and their associated converter sections shown in Figure 33.

The numbers at the right edge of the figure show the summed heat flows for the whole RTG. As can be seen, this RTG design has a thermal efficiency of 3874/4396 = 88%. The 97-watt difference between the 4396 watts generated by the fuel and the 4299 watts flowing to the converter represents the axial heat loss from the ends of the heat source stack; and the 425-watt difference between the heat flow to the converter and the 3874 watts flowing to the TE legs represents the heat losses through the thermal insulation and quartz yarn wraps surrounding the TE elements.

The 292-watt difference between the heat flows to and from the TE legs (curves 4 and 5) represents the gross electrical power output; and the 278-watt difference between the heat flows to and from the converter (curves 2 and 3) represents the net electrical power output, after lead losses.

Figure 33. Axial Variation of Heat Flow Rates

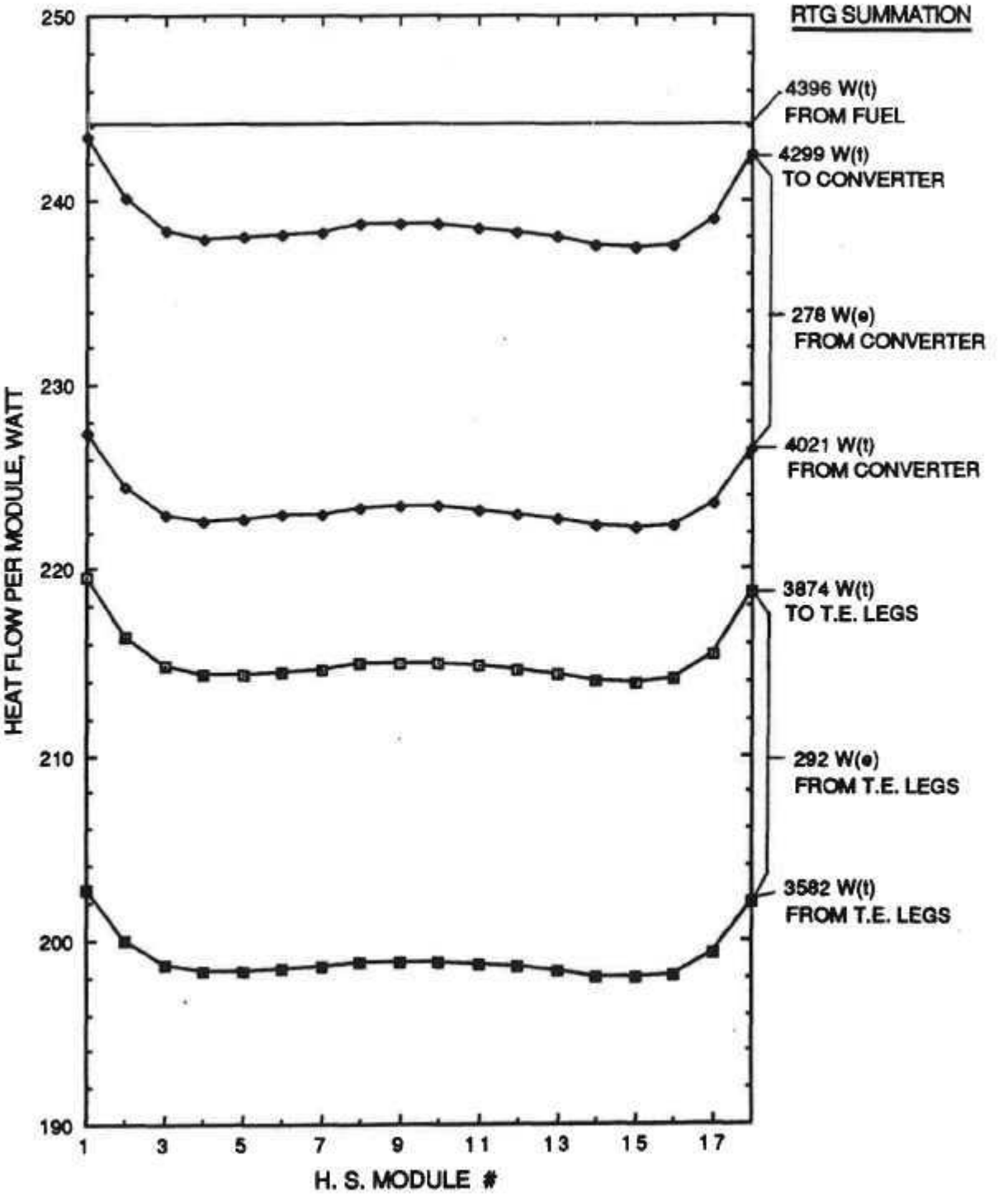

6.4.6 Axial Voltage And Efficiency Profiles: The temperature variations shown in Figure 32 result in the unicouple voltage and efficiency profiles displayed in Figure 34. The averaged values for the RTG are shown at the right edge of the figure. The 0.010-volt difference between the gross and net couple voltages represents the electrical losses in the leads.

The difference between the 7.86% material efficiency and the 7.52% couple efficiency is the effect of contact resistances and ohmic losses in the electrodes. The difference between the couple efficiency and the 6.46% converter efficiency shown in the figure reflects the electrical losses in the leads and the thermal losses through the multifoil side insulation and the quartz yarn wrap. The 0.55-percentage-point difference between the overall converter efficiency and the 6.32% system efficiency reflects the heat losses through the RTG ends.

As seen, the axial variation of the efficiencies is quite small. In fact, the couples near the ends have a higher efficiency because of their lower cold-junction temperatures, which result from axially extending the radiator fins beyond the thermoelectric region.

Figure 34 shows that there are substantial differences between the BOM material efficiency, couple efficiency, converter efficiency, and system efficiency. This highlights the importance of specificity in reporting RTG efficiencies.

Figure 34. Axial Voltage and Efficiency Profiles

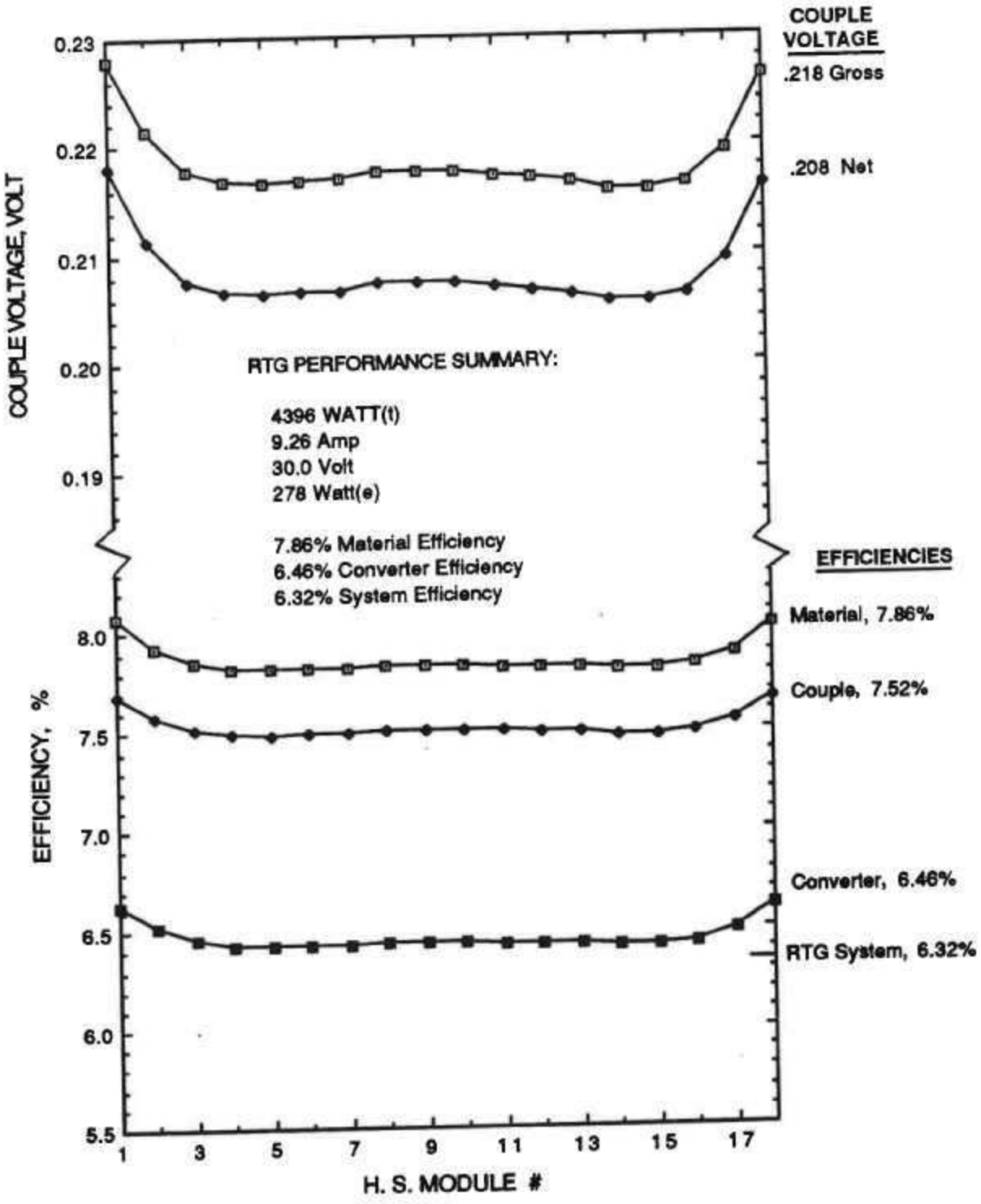

6.5 ENVIRONMENTAL EFFECTS

The preceding four figures showed detailed results for the BOM performance of the radiatively cooled baseline RTG with a 300^{o}K sink temperature. The balance of the paper presents principal results for other environmental conditions and for alternative RTG designs and thermoelectric materials.

6.5.1 Thermal Environments Analyzed: The various RTG designs were analyzed for the following four combinations of thermal power and cooling:

1) Beginning-of-Mission (BOM), assumed to be 3 years after fueling, on a hot (300°K) summer day on Mars, to determine the RTG's maximum hot-junction and clad operating temperatures and to confirm that they did not exceed established limits.

2) End-of-Mission (EOM), assumed to be 7 years after fueling, on a hot summer day on Mars, to compare the EOM power output with the design goal.

3) EOM on a cold (140°K) winter night on Mars, to determine the effect of a cold environment on EOM power.

4) BOM with the RTG contained within the Rover's aeroshell and with its fins cooled by an auxiliary coolant loop, to determine the power output and RTG temperatures during transit to Mars. (The auxiliary cooling tubes were tentatively assumed to have a wall temperature of 100°C).

All the design analyses completed to date were based on the unrealistic assumption that each RTG has an unobstructed view of space and of the Martian ground. In addition, we plan to analyze the case of multiple RTGs mounted in parallel on top of the Rover, to assess the effect of mutual blockage of their radiators.

6.5.2 Effect of Cooling Mode on Performance: Table 4 illustrates the effect of the cooling mode on the BOM temperature distribution, efficiencies, and output of the baseline RTG. The left column shows the results for the water-cooled RTG, representative of the launch and orbital transit conditions; the middle column present the corresponding results for the radiation-cooled RTG, representative of operations on a Martian summer day (300°K); and the right column shows similar results for a Martian winter night (140°K).

Comparison of the three sets of efficiencies and RTG outputs show almost identical results for the three cases. This is because, for a fixed design, changes in the cold-junction temperatures cause similar changes in the hot-junction temperatures; and because the temperature-integrated thermoelectric properties of SiGe are not very sensitive to cold-junction temperature. As a result, the power output of the RTG is quite insensitive to thermal environment, so that the RTG can produce essentially the same power during launch and during transit to Mars as that generated on Mars in either summer or winter. We therefore conclude that the RTG can deliver full operating power during the water-cooled cruise to Mars; and that the power output of the radiatively cooled RTG is essentially independent of the Martian temperature.

Table 4. Effect of Cooling Mode on BOM Performance of Baseline RTG

Cooling Mode	Convective	Radiative	
Auxiliary Coolant Wall Temp., °C	100	—	—
Radiator Sink Temperature, °K	300	300	140
Maximum Temperature, °C:			
Fuel Clad	1089	1172	1166
H.S. Surface	992	1087	1080
Canister	957	1058	1051
TE Hot Junction	888	996	988
TE Cold Junction	155	293	284
Fin Root	117	264	254
Fin Tip	94	220	210
Efficiency, %:			
Material	7.97	7.86	7.88
Couple	7.51	7.52	7.53
Converter	6.50	6.46	6.48
System	6.37	6.32	6.32
RTG Output:			
Current, amp	9.26	9.26	9.26
Voltage	30.2	30.0	30.1
Power	280	278	278
Specific Power, watt/kg	4.77	4.74	4.74

6.5.3 Effect of Mission Time on Performance: Table 5 illustrates the change from BOM (3 years after fuel encapsulation) to EOM (7 years after fuel encapsulation) on the output of the radiation-cooled baseline RTG with a 300°K sink temperature. The left column displays the BOM temperatures and output voltage, current, power, and efficiencies of the RTG, and the right half shows the corresponding EOM values.

The biggest cause of power output change during that period is the decay of the radioisotope fuel, which has a half-life of approximately 89 years. As a result, the original 4500-watt thermal power of the 18-module heat source drops to 4396 watts at BOM and to 4261 watts at EOM. As shown in Table 5, this lowers the maximum clad temperature from 1172°C to 1152°C, drops the maximum hot-junction temperature from 996° to 975°C, and reduces the maximum temperature drop in the SiGe legs from 703°C to 686°C.

This temperature drop reduction lowers the conversion efficiency. The reduced thermal power and reduced efficiency combine to cause a greater-than-proportional reduction in power output. This would be true even if there were no concurrent degradation in thermoelectric properties of the SiGe. But there is a well-characterized material degradation, primarily because of dopant precipitation. As a result, although the thermal power drops only 3.1% during the mission, the system efficiency also drops, by 4.9 percentage points. We therefore conclude that the combined effect of fuel decay and thermoelectric degradation is to reduce the power output by ~8%.

Table 5 shows that the power output of the baseline RTG exceeds the goal of 250 watts EOM, without exceeding the 1000°C hot-junction temperature limit or the 1330°C clad limit.

Table 5. Effect of Mission Time on Performance of Baseline RTG

Mission Time	BOM	EOM
Years After Fuel Encapsulation	3	7
Years of Full-Temperature TE Operation	1	5
Thermal Power, watts	4396	4261
Maximum Temperature, °C:		
Fuel Clad	1172	1152
H.S. Surface	1087	1065
Canister	1058	1037
TE Hot Junction	996	975
TE Cold Junction	293	289
Fin Root	264	260
Fin Tip	220	218
Efficiency, %:		
Material	7.86	7.41
Couple	7.52	7.12
Converter	6.46	6.13
System	6.32	6.01
RTG Output:		
Current, amp	9.26	8.52
Voltage	30.0	30.0
Power, watt	278	256
Specific Power, watt/kg	4.74	4.37

7.0 ALTERNATIVE RTG DESIGNS

7.1 HALF-LENGTH RTG

The preceding design assumed that the Rover's 500-watt power requirement would be met by two 250-watt RTGs. For ease of integration, it may prove preferable to employ four 125-watt RTGs, even though these would have a lower efficiency and lower specific power, because of increased end-section heat losses and masses. To assess that option, the reduction in efficiency and specific power must be quantified, to support the Rover design trade-off.

7.1.1 Mass: Table 6 presents a mass comparison between the two options. For ease of comparison, the table presents masses not for the single RTGs but for the full set of RTGs required to produce 500 watts. The basic design of the half-length RTG is essentially the same as that of the full-length RTG. The only change, besides the 50% reduction in the number of heat source modules and number of unicouple rings, is a decrease in the wall thickness of the RTG housing from 0.090" to 0.060", and a reduction from three parallel Belleville springs to one. These changes from the full-length unit are made possible because the half-length housing is subjected to lower bending moments under transverse loads, and the half-length heat source stack can be held together with only about one fourth the axial preload.

Table 6 shows that the use of four short RTGs instead of two long ones leads to a doubling of the mass of the RTG end sections, including the bellows, graphite pressure plates, load studs, zirconia insulators, other preload hardware, multifoil end insulation, housing ends and covers, and of the mass of the resistance thermometer, gas management assembly, and auxiliary coolant manifolds. In addition, there is also a significant increase in the mass of the canister end caps and load spreaders and of the radiator fin extensions. The total mass addition for the short-RTG option add up to 12.3 kg. But these additions are partially offset by reductions in the mass of the Belleville springs and of the RTG housing side wall totaling 5.1 kg. Thus, the use of four short RTGs leads to a net mass increase of only 7.2 kg or 6.2%.

Table 6. Mass of "250-W" RTGs Versus "125-W" RTGs

RTG MASS BREAKDOWN (kg)	TWO 250-W RTGS	FOUR 125-W RTGS	Δ
HEAT SOURCE			
GPHS MODULES (18/9)			
FUEL (PuO_2)	21.46	21.46	0
CAPSULES (Ir)	8.42	8.42	0
GRAPHITICS	22.22	22.22	0
H.S. CANISTER (Mo)			
SIDE WALLS	4.42	4.42	0
BELLOWS	0.22	0.44	0.22
END CAPS AND LOAD SPREADERS	2.90	4.64	1.74
H.S.STRUCTURAL SUPPORTS			
GRAPHITE PRESSURE PLATES	1.04	2.08	1.04
LOAD STUDS+ZIRCONIA	0.54	1.08	0.54
BELLEVILLE SPRINGS (Ti)	4.62	2.20	-2.42
OTHER PRELOAD HARDWARE	1.68	3.36	1.68
CONVERTER			
ELECTRICAL CIRCUITS			
TE ELEMENTS (576/288)	10.86	10.86	0
TE FASTENERS AND SEALS	2.18	2.40	0.22
ALUMINA INSULATORS	1.76	1.76	0.00
ELECTR. CONNECTORS +TERMINALS	0.68	0.80	0.12
MULTIFOIL INSULATION (Mo/Quartz)			
SIDES	10.52	10.52	0
ENDS	1.36	2.72	1.36
RTG HOUSING (Al)			
SIDE WALL (.090"/.060")	13.08	10.44	-2.64
END SECTION	0.94	1.88	0.94
COVERS	1.96	3.92	1.96
RESISTANCE THERMOMETER	0.60	1.20	0.60
GAS MGMT. ASSEMBLY	0.32	0.64	0.32
RADIATOR			
FINS (8/8)	4.76	5.72	1
AUXILIARY COOLANT MANIFOLDS	0.50	1.00	0.50
EMISSIVITY COATING	0.30	0.40	0.10
TOTAL MASS(kg)	**117.34**	**124.58**	**7.24**

7.1.2 Performance: The mass of the two "250-watt" RTGs was compared with that of four "125-watt" RTGs in Table 6. The temperatures, efficiencies, and outputs for the two options are compared in Table 7, both for BOM and EOM.

The table shows that the short RTGs also meet their design goal (125 watt EOM per RTG) without exceeding the 1000°C hot-junction temperature limit. It shows that the system efficiency of the short RTG is almost as high as that of the long RTG.

This was not expected, because the four short RTGs have twice as many end sections and obviously have greater heat losses from the ends of their heat source stacks. Evidently, these losses are compensated by their higher converter efficiencies, as shown in the table. Their higher converter efficiency is due to their lower cold-junction temperature (271°C versus 289°C) which results from the greater effectiveness of the axial radiator extensions in the short RTGs. It should be noted, however, that the radiator fin design has not yet been optimized for either the long or the short RTGs.

Table 7 shows that the specific power of the short RTGs is 9% lower than that of the long ones. This is primarily due to their higher mass rather than lower system efficiency. The difference in specific power between the two options is small enough to make the short RTG option a viable alternative to the baseline design, if the shorter units are indeed easier to integrate with the Rover (e.g., because the shorter RTGs are less prone to block the Rover's sensors and/or antennas). But this conclusion will have to be re-examined after the effect of mutual radiator blockage of multiple RTGs is taken into account.

An additional advantage of the short RTGs is that if one of the four should experience catastrophic failure before the end of the mission, the other three would still supply 75% of the Rover's design power, permitting continued Mars operations on a limited scale. However, it should be emphasized that this is a highly unlikely event. Of the more than thirty RTGs flown on previous space missions, none has ever experienced catastrophic failure.

Table 7. Effect of RTG Length on Performance

Number of HS Modules per RTG	18		9	
RTG Length, inches	45.9		26.3	
Nominal EOM Power per RTG, watts	250		125	
Number of RTGs on Rover	2		4	
Mission Time	BOM	EOM	BOM	EOM
Thermal Power per RTG, watt	4396	4261	2198	2131
Maximum Temperature, °C:				
Fuel Clad	1172	1152	1172	1153
H.S. Surface	1087	1065	1086	1067
Canister	1058	1037	1059	1039
TE Hot Junction	996	975	998	980
TE Cold Junction	293	289	275	271
Fin Root	264	260	247	243
Fin Tip	220	218	206	203
Efficiency, %:				
Material	7.86	7.41	8.07	7.58
Couple	7.52	7.12	7.72	7.29
Converter	6.46	6.13	6.61	6.26
System	6.32	6.01	6.32	5.96
Output of Set of RTGs:				
Current, amp	18.5	17.0	18.3	18.3
Voltage	30.0	30.0	30.2	30.2
Power, watt	556	512	556	508
Mass of Set of RTGs, kg	117.3	117.3	124.6	124.6
Specific Rower, watt/kg	4.74	4.37	4.46	4.08

7.2 MULTICOUPLE RTG

The RTG designs discussed thus far employed unicouples as their thermoelectric elements. This section discusses an alternative design based on multicouples.

7.2.1 Thermoelectric Multicouple: The standard multicouple, developed for DOE's MITG and Mod-RTG programs, is depicted in Figure 35. Its principal difference from the unicouple depicted in Figure 9 is that the unicouple has two TE legs, while the multicouple has 40 legs. These, together with its hot and cold electrodes, form 20 series-connected couples. The standard multicouple legs are only 0.3″ long, compared to the unicouple's 0.8″ leg length. This reduces the weight of the thermal insulation and of the RTG housing.

The multicouple's legs are bonded to, and insulated from, each other by 0.002″ glass layers. The heat collector, approximately 2″ square, is made of graphite. In contrast to the unicouple, the multicouple's mounting stud and power leads penetrate through the RTG housing, and electrical connections between multicouples are made on the outside of the housing. As will be seen, these differences affect the Rover RTG design.

Multicouples operating at the required hot-junction temperature (1000°C) have a much smaller data base than unicouples, which have successfully operated for periods in excess of 100,000 hours. Multicouple development was initiated in the late 1970s [17], their present design was defined in 1983 [18], and their most successful test to date (of an assembly of eight multicouples produced at GE and tested at Fairchild) ran for 6000 hours, until it was interrupted for a planned modification of the test fixture and for withdrawal of three of the multicouples for destructive examination.

Figure 35. Multicouple Cross-Section

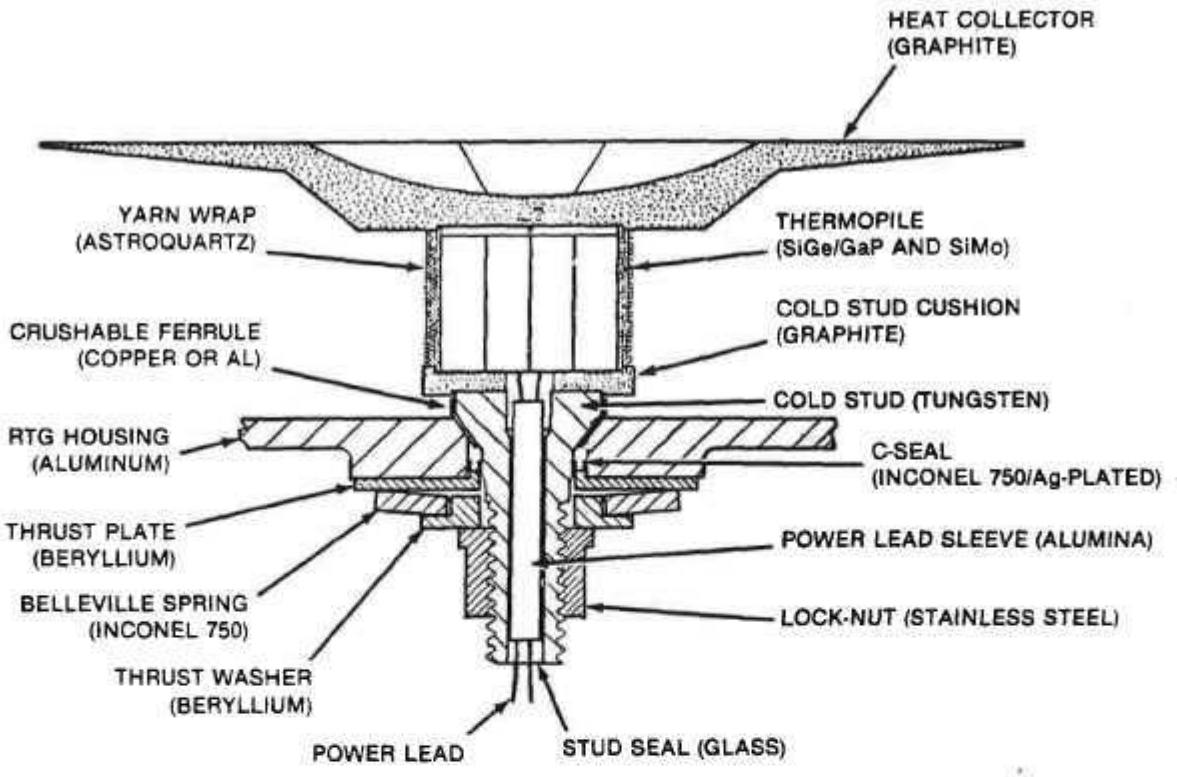

During the 6000-hour test, the six multicouples that operated with a positive bias with respect to the RTG housing exhibited very stable performance, but the two multicouples that were negatively biased exhibited unacceptable degradation rates. This negative-bias problem had been first identified more than two years earlier.

After an intensive investigation, General Electric personnel have now identified the cause of the problem. They have concluded, and a DOE-convened review panel has concurred, that the problem was not due to any inherent flaw in the multicouples, but was an artifact of avoidable impurities in the GE-furnished test assembly. Specifically, the electrical heater had released potassium impurities. Under negative bias conditions, the potassium ions migrated into the negatively biased regions of the 0.002"-thick glass layers that separate the forty legs in the multicouple, causing internal shorts within the multicouple. This explanation has been demonstrated experimentally, and will be confirmed by a full-up test of a planned new test assembly. Once the conclusions are confirmed by extended lifetests, multicouples can be considered a viable alternative to unicouples.

7.2.2 RTG Design: Horizontal and vertical cross-sections of an RTG employing standard-size multicouples are shown in Figures 36 and 37. The multicouple-RTG design depicted in those figures is generally similar to the unicouple-RTG design shown in Figure 18 and only the significant differences will be mentioned.

As in the MITG and Mod-RTG designs, there are eight multicouples per horizontal layer, and only one multicouple layer per heat source module. For a 250-watt(e) power output, the RTG has 16 heat source modules. Thus, there are 128 multicouples per RTG, or about one fifth as many thermoelectric units as in the unicouple RTG.

In the Mod-RTG the multicouple mounting holes are sealed by conical metal ferrules, but these would be inadequate for preventing inflow of the Martian atmosphere during long-term operations on Mars. Therefore, the bolt holes in the present design are hermetically sealed by eight semi-cylindrical aluminum seal covers welded to the aluminum housing hubs.

In the standard multicouple design, the leads pass through the housing wall, and are series-connected on the outside. To preserve hermeticity in the present RTG design, the series leads are passed back to the inside of the housing via insulated studs, for internal series connections between the eight multicouples in each ring.

Figure 36. Multicouple RTG, Horizontal Cross-Section

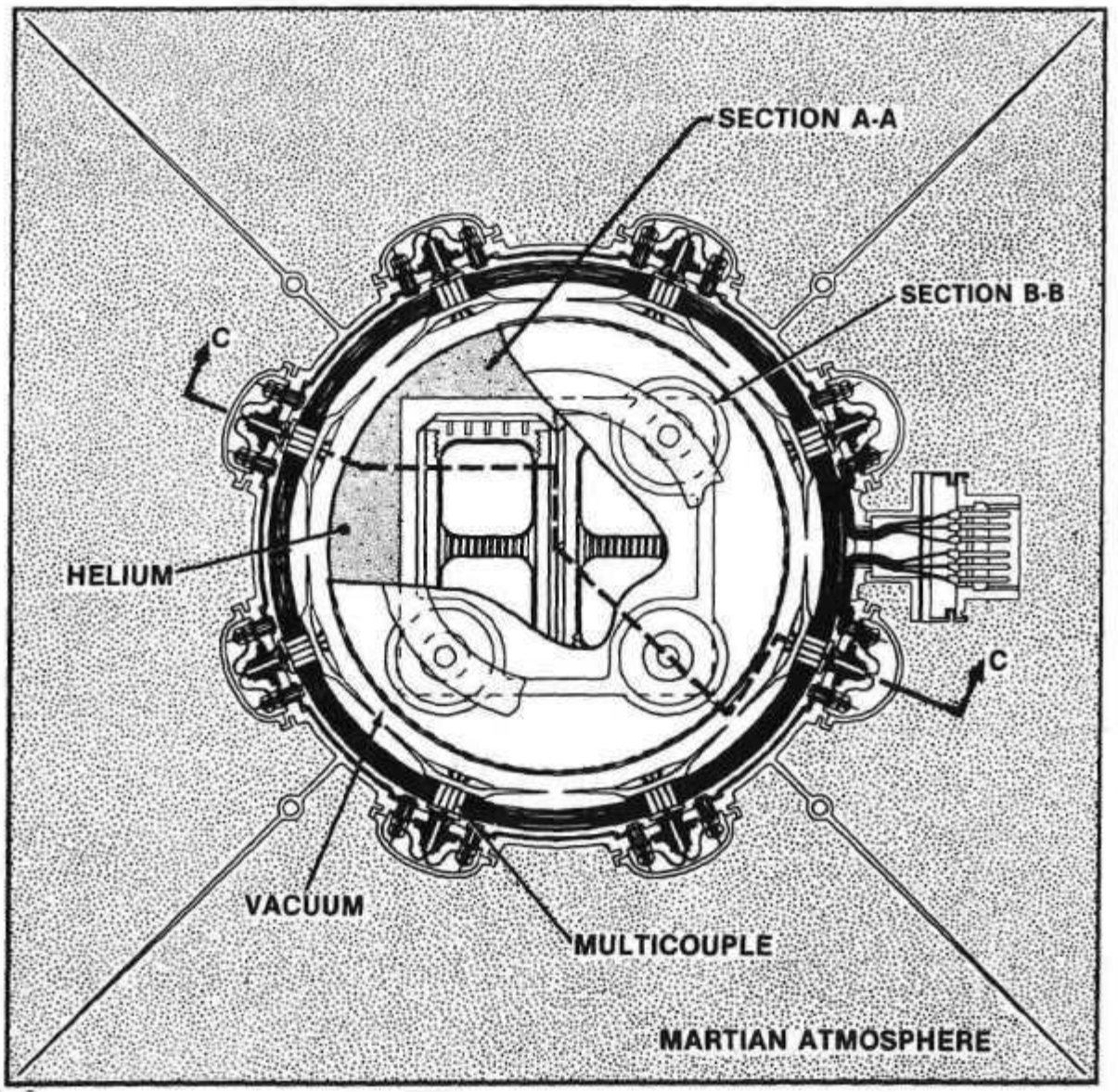

As in the Mod-RTG, the eight multicouples are embedded in a 0.3″-thick layer of thermal insulation, consisting of 60 layers of 0.0003″-thick molybdenum foils, separated from each other by zirconia spacer particles. This type of insulation is not only lighter than the standard unicouple insulation, but its lower thickness also leads to significant weight saving due to the consequent reduction in housing diameter from 9″ to 7.5″.

The option shown in Figure 36 has four radiator fins. The alternative of eight (shorter and thinner) fins was also analyzed. The analytical results showed that the two options yield very similar specific powers.

As shown in Figures 36 and 37, the series connections between the multicouples are horizontal rather than vertical. The multicouple RTG design is modular [17], because each horizontal ring produces the desired RTG voltage (30V). The 16 rings are connected in parallel. To isolate the effect of shorts-to-ground, the leads from each of the sixteen current loops are separately brought out to the power conditioning unit through a multipin terminal near the base of the RTG, as shown at the right of Figures 36 and 37.

Figure 37. Multicouple RTG, Vertical Cross-Section (C-C)

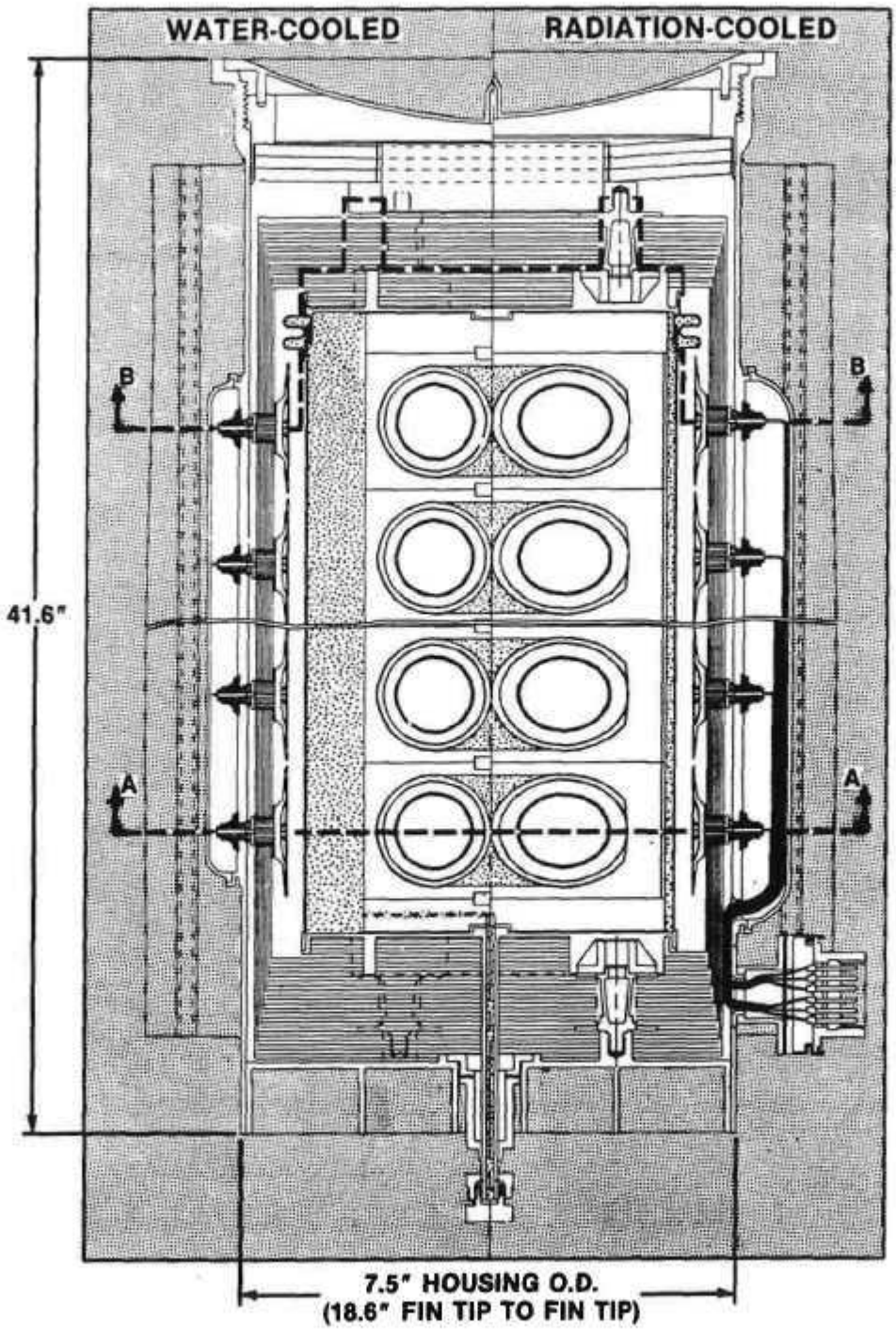

7.2.3 Mass: Table 8 presents the mass summary of the multicouple RTG depicted in Figures 36 and 37, and compares it to that of the baseline unicouple RTG. The two RTGs have the same EOM power goal, 250 watts per RTG. The unicouples and multicouples both use SiGe legs, but the n-legs of the multicouples contained a GaP additive, similar to those in all previously tested multicouples. This raises the couples' BOM figure of merit (Z) from 0.00058 K^{-1} to 0.00072 K^{-1}, and increases the BOM material efficiency from 7.86% to 8.57%. As a result, the multicouple RTG can achieve its 250-watt output goal with a lower thermal input power. Therefore, the multicouple RTG design is based on 16 rather than 18 heat source modules.

As shown in Table 8, the total mass of the multicouple RTG is 23% lower than that of the baseline RTG (45.3 kg versus 58.7 kg). One of the primary causes of that mass reduction is the smaller number of heat source modules and the resultant shorter RTG length. The shorter length not only has a direct effect on the mass of the RTG housing and the heat source canister, but also results in additional mass savings: the housing wall thickness can be reduced, because the bending moments on the cantilevered structure are lower; and the mass of the Belleville springs is reduced because the axial preload to hold the heat source stack together is lowered.

In addition to the above mass savings that result from the higher thermoelectric material efficiency, there are also significant savings deriving from the thermal insulation used in the multicouple RTG. Elimination of the quartz cloth spacers between the 60 layers of Mo foil results in direct mass savings and in significant indirect savings. The latter occur because the much thinner insulation package and shorter TE legs reduce the RTG housing diameter from 9.1" to 7.5". The table reflects the net result of all these mass changes.

Parenthetically, it should be noted that unicouples with GaP-doped N-legs may also be feasible. But these have not yet been built and tested, and their development would not be a trivial material substitution because the two types of TE elements employ substantially different hot-junction bonding methods.

Table 8. Mass of Unicouple RTG Versus Multicouple RTG

RTG MASS BREAKDOWN (kg)	UNICOUPLE RTG BASELINE DESIGN	MULTICOUPLE RTG
HEAT SOURCE		
GPHS MODULES (18/16)		
FUEL (PuO_2)	10.73	9.54
CAPSULES (Ir)	4.21	3.74
GRAPHITICS	11.11	9.88
H.S. CANISTER (Mo)		
SIDE WALLS	2.21	1.97
BELLOWS	0.11	0.10
END CAPS AND LOAD SPREADERS	1.45	1.45
H.S.STRUCTURAL SUPPORTS		
GRAPHITE PRESSURE PLATES	0.52	0.52
LOAD STUDS+ZIRCONIA	0.27	0.27
BELLEVILLE SPRINGS (Ti)	2.31	1.27
OTHER PRELOAD HARDWARE	0.84	0.53
CONVERTER		
ELECTRICAL CIRCUITS		
TE ELEMENTS (576/128)	5.43	2.09
TE FASTENERS AND SEALS	1.09	0.49
ALUMINA INSULATORS	0.88	----
ELECTR. CONNECTORS +TERMINALS	0.34	0.26
MULTIFOIL INSULATION (Mo/Quartz)		
SIDES	5.26	3.44
ENDS	0.68	0.59
RTG HOUSING (Al)		
SIDE WALL (.090"/.080")	6.54	5.20
END SECTION	0.47	0.38
COVERS	0.98	0.74
RESISTANCE THERMOMETER	0.30	0.30
GAS MGMT. ASSEMBLY	0.16	0.16
RADIATOR		
FINS (8/4)	2.38	1.93
AUXILIARY COOLANT MANIFOLDS	0.25	0.25
EMISSIVITY COATING	0.15	0.15
TOTAL MASS(kg)	58.67	45.25

7.2.4 Performance: The multicouple RTG design shown in Figures 36 and 37, with demonstrated MC performance parameters, was subjected to detailed thermal, thermoelectric, and electrical analyses, identical to those performed for the baseline (unicouple) RTG.

The results of those analyses for the two RTGs are summarized in Table 9, which compares their temperatures, efficiencies, output powers, and specific powers. Both cases are for radiative cooling with a 300°K heat sink. The unicouples employed SiGe n- and p-legs, with a BOM figure of merit (Z) of $0.00058K^{-1}$. In the case of the multicouples, the n-legs contain a GaP additive, which raises the BOM Z to $0.00072K^{-1}$. Both cases employed measured values of contact resistances for their respective TE elements.

Table 9 shows very similar temperatures for the RTGs, with two exceptions. The first is that the temperature drop from the cold junction to the fin root is much higher in the multicouple-RTG (56°C) than in the unicouple-RTG (29°C). This is due to the fact that each multicouple rejects much more heat than a unicouple, and that this heat has to flow through a greater distance to reach the nearest fins, since the MC-RTG has only four fins instead of eight.

The second difference between the two RTGs is that the root-to-tip temperature drop in the fins is appreciable greater (75°C) in the MC RTG than in the UC unit (44°C). This is due to the fins' greater length, which is necessitated by the smaller number of fins.

Table 9. Performance of Multicouple RTG Versus Unicouple RTG

Thermoelectric Elements	Unicouples		Multicouples	
Number of Elements	576		128	
Number of H.S. Modules	18		16	
RTG Length, inches	45.9		41.6	
RTG Housing Diameter, inches	9.1		7.5	
N-Leg Material	SiGe		SiGe/GaP	
Couple Figure of Merit, K^{-1}	0.00058		0.00072	
Number of Fins	8		4	
Fin Root Thickness, inch	0.060		0.100	
Fin Length, inches	3.0		5.5	
Mission Time	BOM	EOM	BOM	EOM
Thermal Power per RTG, watt	4396	4261	3907	3787
Maximum Temperature, °C:				
Fuel Clad	1172	1152	1171	1154
H.S. Surface	1087	1065	1085	1068
Canister	1058	1037	1057	1040
TE Hot Junction	996	975	1009	991
TE Cold Junction	293	289	315	309
Fin Root	264	260	259	255
Fin Tip	220	218	184	182
Efficiency, %:				
Material	7.86	7.41	8.57	8.14
Couple	7.52	7.12	8.01	7.60
Converter	6.46	6.13	7.05	6.68
System	6.32	6.01	6.76	6.42
RTG Output:				
Current, amp	9.3	8.5	9.0	8.3
Voltage	30.0	30.0	29.5	29.5
Power, watt	278	256	264	243
RTG Mass, kg	58.6	58.6	45.3	45.3
Specific Power, watt/kg	4.74	4.37	5.83	5.37

In spite of these increased temperature drops, the MC RTG shows virtually the same system efficiency as the UC RTG. This is due to the use of the GaP additive in the n-legs, which raises the figure of merit from 0.00058 K^{-1} to 0.00072 K^{-1}, and the BOM material efficiency from 7.86% to 8.57%. As shown in Table 9, the MC RTG with 16 heat source modules produces 5% less power than the UC RTG with 18 heat source modules. In fact, it falls a little below its 250-watt EOM goal.

The last two lines of Table 9 compare the masses (from Table 8) and the specific powers of the two RTGs. As can be seen, the specific power of the MC RTG is 23% higher than that of the UC RTG. This benefit must be weighed against their lower technological maturity and higher programmatic risk.

7.3 SHORT-UNICOUPLE RTG

7.3.1 Rationale: The preceding section showed that the specific power of a 250-watt RTG employing multicouples is 23% higher than one employing standard unicouples. Part of that improvement is due to the GaP additive in the multicouple's n-legs, leading to a higher figure of merit and consequently a higher system efficiency; and part is due to the multicouple's much shorter leg length (0.3" instead of 0.8"), which permits a thinner insulation package and a smaller housing diameter, with consequent mass savings.

The long-term performance stability of multicouples has not yet been adequately demonstrated, and may not be achievable in time for the projected MRSR mission schedule. Since unicouples are a much more mature technology than multicouples, the possibility of achieving a significant part of the multicouple's performance improvement in a modified unicouple RTG is of considerable interest. This may be achievable by developing short-legged unicouples with GaP-doped n-legs. The present section describes an RTG using 0.4"-long unicouples, and compares its performance to that of an RTG employing standard-length unicouples with the same thermoelectric materials.

7.3.2 Design: The design of the short-unicouple RTG is in most respects similar to the previously described baseline RTG. Only the significant differences will be mentioned. Figure 38 shows a horizontal cross-section of the RTG. The unicouples have a leg length of 0.4″ instead of 0.8″, and their heat collectors are 1.50″ x 1.46″ instead of 1.06″ x 0.90″.

The RTG cross-section is similar to that of the baseline RTG, except for:

- Much thinner thermal insulation (0.4″ instead of 0.8″), with the 60 foil layers separated by zirconia particles instead of quartz cloths
- Correspondingly smaller housing diameter (8.25″ instead of 9″)
- Twelve unicouples per ring instead of sixteen
- Six radiator fins instead of eight
- Fin height of 4″ instead of 3″, and fin root thickness of 0.080″ instead of 0.060″.

Figure 38. Short-Unicouple RTG, Horizontal Cross-Section

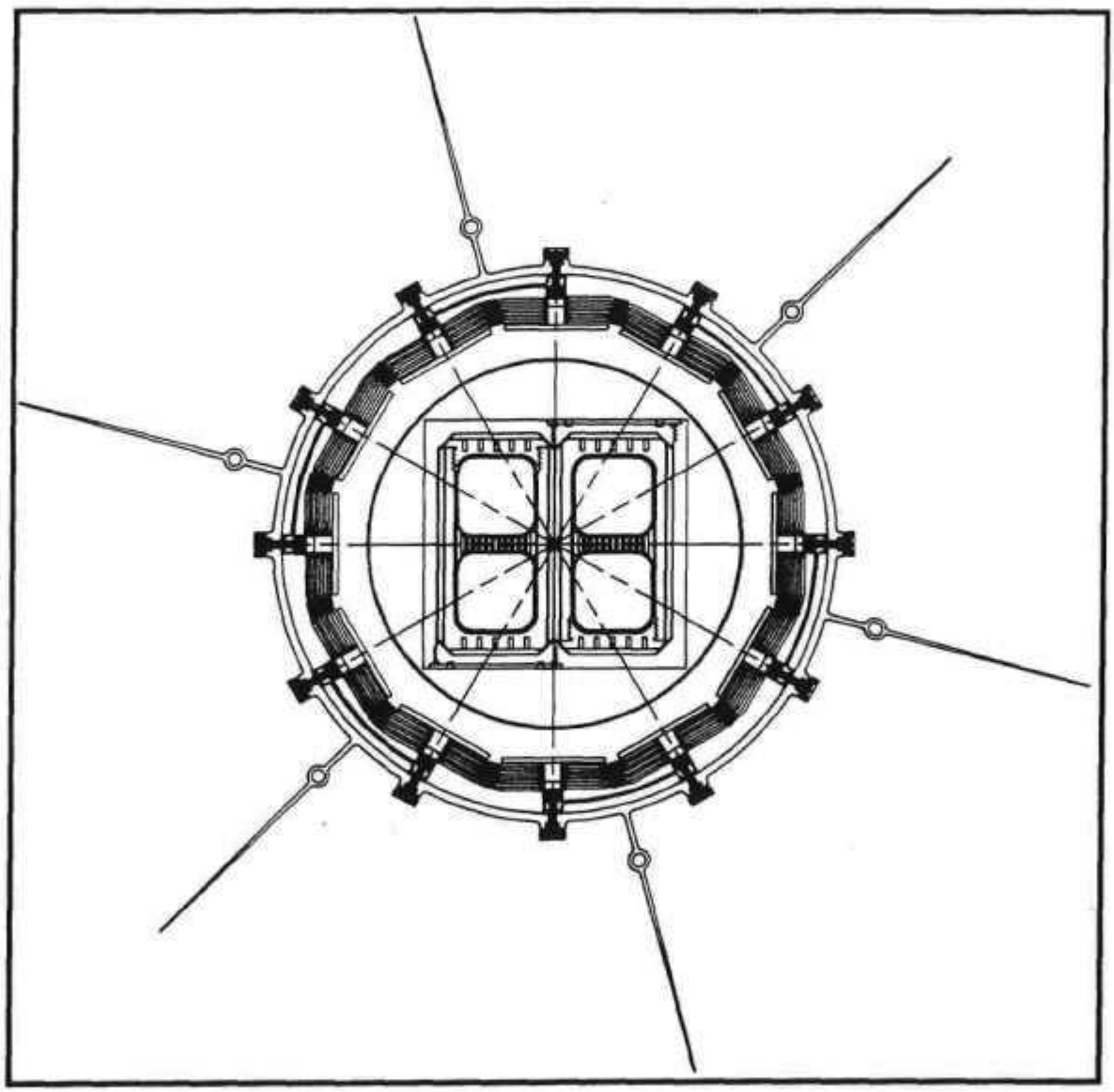

Figure 39 presents a vertical cross-section of the short-unicouple RTG. It is quite similar to the baseline RTG, except that:

- There are 16 instead of 18 heat source modules. The lower thermal power is made possible by the higher system efficiency resulting from the use of the GaP additive in the n-legs.

- There are 24 layers of 12 unicouples instead of 36 layers of 16 unicouples.

- Thus there are only half as many thermoelectric elements in the short-unicouple RTG as in the baseline RTG.

- The 288 short unicouples are arranged in a 144 x 2 matrix instead of 144 x 4 matrix used in the baseline design.

Figure 39. Short-Unicouple RTG, Vertical Cross-Section

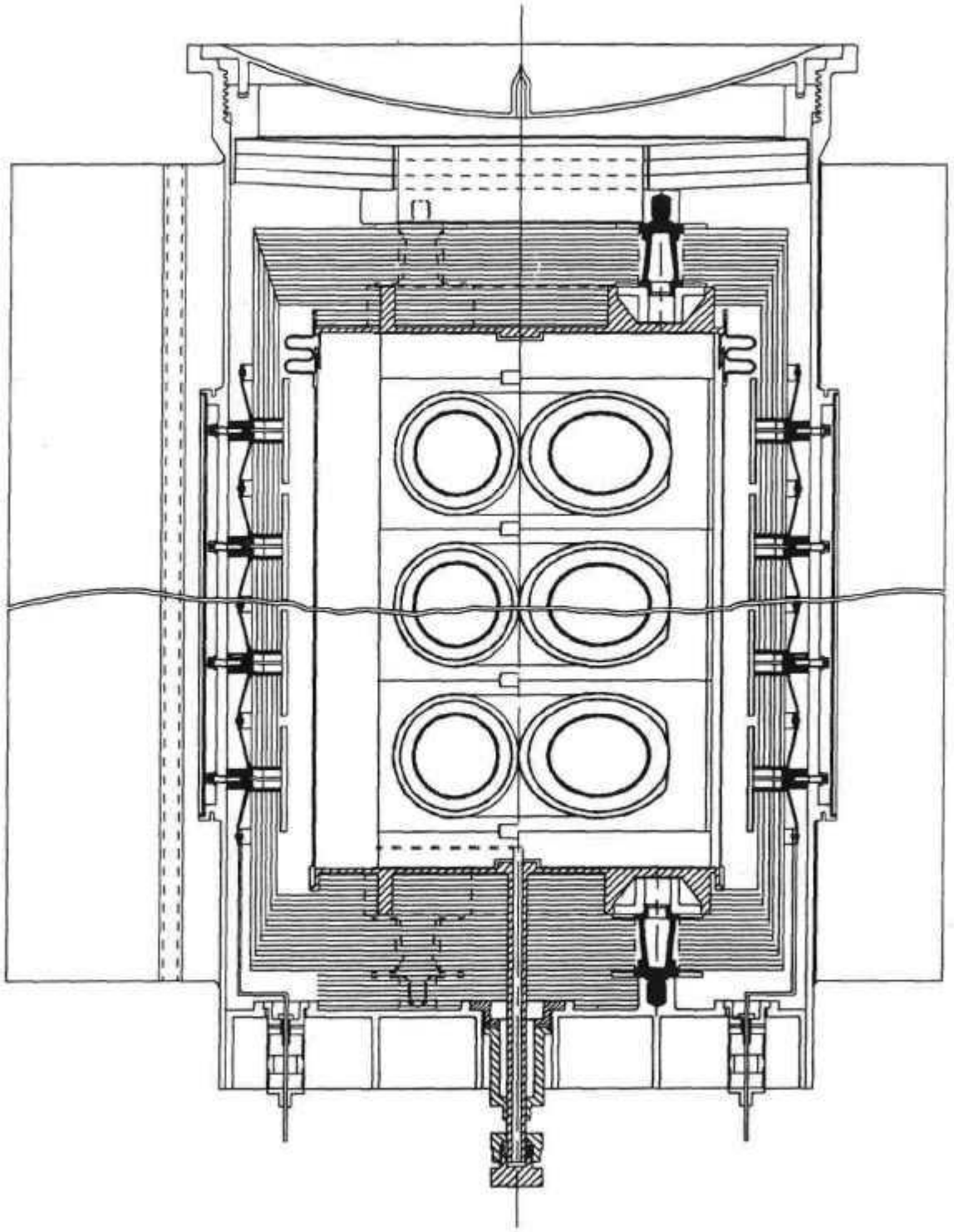

7.3.3 Mass: The mass and performance of the short-unicouple RTG were compared with those of the standard-unicouple RTG and the multicouple RTG. To isolate the design effects from the material effects, all three designs were compared for the same material properties, based on GaP-doped n-legs. The standard-unicouple RTG, and the short-unicouple RTG both had 18 heat source modules, to utilize existing thermal and electrical analysis models. They resulted in appreciably higher power outputs than 250 watts EOM, but this does not prevent comparison of the three designs on the basis of specific power.

Table 10 compares the mass breakdown of the three designs. The mass of the short-unicouple RTG is 9.5% below that of the standard-unicouple RTG. This mass saving is due to its smaller number of unicouples and to their shorter leg length, which permits a lighter insulation package and RTG housing.

Table 10. Effect of T.E. Element Geometry on RTG Mass (in kg)

THERMOELECTRIC ELEMENT (SiGe/GaP)	STANDARD UNICOUPLE	SHORT UNICOUPLE	MULTICOUPLE
HEAT SOURCE			
GPHS MODULES (18/18/16)			
FUEL (PuO_2)	10.73	10.73	9.54
CAPSULES (Ir)	4.21	4.21	3.74
GRAPHITICS	11.11	11.11	9.88
H.S. CANISTER (Mo)			
SIDE WALLS	2.21	2.21	1.97
BELLOWS	0.11	0.11	0.10
END CAPS AND LOAD SPREADERS	1.45	1.45	1.45
H.S.STRUCTURAL SUPPORTS			
GRAPHITE PRESSURE PLATES	0.52	0.52	0.52
LOAD STUDS+ZIRCONIA	0.27	0.27	0.27
BELLEVILLE SPRINGS (Ti)	2.31	2.31	1.27
OTHER PRELOAD HARDWARE	0.84	0.84	0.53
CONVERTER			
ELECTRICAL CIRCUITS			
TE ELEMENTS (576/288/128)	5.43	4.11	2.09
TE FASTENERS AND SEALS	1.09	0.65	0.49
ALUMINA INSULATORS	0.88	0.88	----
ELECTR. CONNECTORS +TERMINALS	0.34	0.34	0.26
MULTIFOIL INSULATION (Mo/Quartz)			
SIDES	5.26	2.51	3.44
ENDS	0.68	0.60	0.59
RTG HOUSING (Al)			
SIDE WALL (.090"/.090"/.080")	6.54	5.62	5.20
END SECTION	0.47	0.38	0.38
COVERS	0.98	0.98	0.74
RESISTANCE THERMOMETER	0.30	0.30	0.30
GAS MGMT. ASSEMBLY	0.16	0.16	0.16
RADIATOR			
FINS (8/8/4)	2.38	2.38	1.93
AUXILIARY COOLANT MANIFOLDS	0.25	0.25	0.25
EMISSIVITY COATING	0.15	0.15	0.15
TOTAL MASS(kg)	**58.67**	**53.07**	**45.25**

7.3.4 Performance: Table 11 compares the principal BOM performance parameters of the short-unicouple RTG with those of the standard-unicouple RTG and of the multicouple RTG. All three are based on the same thermoelectric materials (SiGe/GaP), and the two unicouple RTGs have the same thermal power. As shown, the short-unicouple RTG has somewhat longer and thicker fins, to compensate for its smaller housing diameter and smaller number of fins.

As can be seen, for the same number of heat source modules the RTG employing short unicouples is 9.4% lighter than the one employing standard-size unicouples. This mass saving comes about because the shorter unicouples permit a thinner and lighter insulation package and a smaller-diameter RTG housing.

However, Table 11 also shows that the short-unicouple RTG produces 5.0% less power than the corresponding standard-unicouple RTG. The primary reason for its lower efficiency is that by halving the couple's leg length, we necessarily double its heat flux and current density. For a given set of thermal and electrical contact resistivities, this doubles the voltage drops at the interfaces between the TE legs and the electrodes, and doubles the temperature drops through the couple's heat shunt, its electrical (alumina) insulator, and its interface with the RTG housing.

Since the mass reduction made possible by the short unicouples is to a considerable extent offset by the drop in system efficiency, the net rise in the RTG's specific power is only 5.0%, which cuts in half the incentive for undertaking the development of short unicouples.

Table 11. Comparative Performance of Short-Unicouple RTG

Thermoelectric Elements	Standard Unicouples	Short Unicouples	Multi-Couples
Number of Elements	576	312	128
Number of H.S. Modules	18	18	16
RTG Length, inches	45.9	45.9	41.6
RTG Housing Diameter, inches	9.1	8.2	7.5
RTG Housing Thickness, inches	0.09	0.09	0.08
Number of Fins	8	6	4
Fin Root Thickness, inch	0.060	0.080	0.08
Fin Length, inches	3.0	4.0	5.5
Thermal Power Per RTG, watt	4396	4396	3907
Maximum Temperature, °C:			
Fuel Clad	1173	1196	1159
H.S. Surface	1088	1114	1071
Canister	1059	1087	1041
TE Hot Junction	997	996	992
TE Cold Junction	290	312	316
Fin Root	260	257	259
Fin Tip	223	210	184
Efficiency, %:			
Material	8.72	8.47	8.41
Couple	8.28	7.89	8.02
Converter	7.04	6.69	7.15
System	6.89	6.55	6.86
RTG Output:			
Current, amp	10.09	9.60	9.10
Voltage	30.0	30.0	29.5
Power, watt	303	288	268
RTG Mass, kg	58.67	53.13	45.25
Specific Power, watt/kg	5.16	5.42	5.92

S-171.01C 08-89

8.0 EFFECT OF THERMOELECTRIC PROPERTIES ON RTG

The results thus far were all based on demonstrated thermoelectric properties of the SiGe unicouples and the SiGe/GaP multicouples. The present section examines the effect that improvements of those properties would have on the RTG designs and on their mass and performance. RTGs based on five different material models were analyzed:

8.1 MATERIALS STUDIED

1. The first is a JPL model for SiGe, with 78% Si in the hotter 85% of the TE legs and 63% Si in the cooler 15% of the leg. This is the same material model used in our baseline design analysis, and is representative of the unicouples used in the Galileo RTGs. At BOM, it yields a figure of merit of 0.000584 K^{-1} over a 1000°C-to-300°C temperature range.

2. The second material model employed is designated ITM-197. The material's thermoelectric properties are those reported by General Electric, but it has not yet been built into a couple. Its BOM figure of merit is 0.000768 K^{-1}.

3. The third material model, designated GE Hybrid, represents the materials used in the multicouples built and tested to date. It was used as the basis for our multicouple design. Its BOM figure of merit (Z) is 0.000782 K^{-1}. It has not yet been built into unicouples. Doing so would require development of new bonding techniques.

4. The fourth material model, designated SP-100, represents the thermoelectric performance parameters assumed for the SP-100 reactor system reference design. It assumes a GaP-doped n-leg (Z=0.00111) and a SiGe p-leg with an as-yet undefined additive (Z=0.00069), yielding a couple Z of 0.00085 K^{-1}. This performance level has not yet been achieved.

5. The fifth material model is designated "dream". Its composition and development pathway are not yet defined and thus far totally unproven. It was included at JPL's request, to quantify what effect a figure of merit of 0.00140 K^{-1} would have on RTG performance, if such a material could be successfully developed.

8.2 ANALYSIS

The five RTG designs were based on the same basic arrangement, i.e., the baseline design employing 16 unicouples (of 0.8″ leg length) per horizontal ring, connected four in parallel. However, the number of heat source modules, the number of unicouple layers, and the cross-sectional areas of the unicouple legs were varied to meet (or come close to) the RTG voltage and power goals. The voltage goal used was 30 volts after lead losses; and the power goal (after lead losses) was 250 W EOM or 280 W BOM. Each of the five material models employed temperature-dependent resistivities, conductivities, and Seebeck coefficients for the n- and p-legs.

8.2.1 Assumptions: The primary emphasis in the design studies and analyses was to determine the relative RTG performance for the five options, rather than their absolute values. For this reason, and in the interest of expediency, a number of approximating assumptions were made:

The axial variations of the heat flow rates, temperatures, and couple outputs were ignored. All couples were assumed to operate at the same hot-junction temperature (1000°C) and cold-junction temperature (300°C) employed in previous RTG tests. In addition, the fraction of the generated heat that flows to the thermoelectric couples was assumed to be 88%, based on the results of the more detailed and exact analysis of the baseline RTG design.

Based on the same analysis, the effect of the electrode resistances and the electrical contact resistance were accounted for by increasing the materials' resistivities by 10%; and the effect of electrical lead losses was accounted for by subtracting 6% from each couple's output voltage.

Finally, the number of thermoelectric rings per heat source module had been arbitrarily fixed at 2.0 in the baseline design (for consistency with the Galileo RTG), but was varied in each of the five comparison designs so as to maximize the conversion efficiency.

Because of these differences in analytical approach, the results of the material comparison analysis are not an exact match to those of the baseline RTG analysis. But the comparison analysis is internally consistent, and its results are a valid comparison of the relative RTG performance for the five TE materials.

8.2.2 Thermoelectric Couple Optimization: From Eq. (26), the couple's conversion efficiency η is given by

$$\eta = \frac{IV}{Q_h} = \frac{IV}{K\Delta T + IS_hT_h - I^2R/2 - I(S_hT_h - S_cT_c - S\Delta T)/2} \tag{31}$$

Solving Eq. (29) for I and inserting the results into (31), we obtain

$$\eta = \frac{V(S\Delta T - V)}{KR\Delta T + (S_hT_h + S_cT_c + S\Delta T)(S\Delta T - V)/2 - (S\Delta T - V)^2/2} \tag{32}$$

which is the general solution for the efficiency of a thermoelectric couple, before optimization of its output voltage V and of the ratio of its n- and p-leg areas. From Eqs. (19) and (20), the couple's thermal conductance K and electrical resistance R are given by

$$K = [k_n\alpha + k_p(1-\alpha)](A/L) \tag{33}$$

$$R = [\rho_n/\alpha + \rho_p/(1-\alpha)](L/A) \tag{34}$$

where α is the area fraction of the n-leg and $1-\alpha$ is the area fraction of the p-leg, and A is the combined area of the two legs. Combining these, the product KR is given by

$$KR = k_n\rho_n + k_p\rho_p + k_n\rho_p\left[\frac{\alpha}{1-\alpha}\right] + k_p\rho_n\left[\frac{1-\alpha}{\alpha}\right] \tag{35}$$

Note that for a given set of hot- and cold-junction temperatures the product KR, and therefore the efficiency η, are independent of the leg dimensions L and A. The value of α which minimizes the product KR and therefore maximizes the efficiency η is given by

$$\alpha_{opt} = \left[1 + \sqrt{(k_n/k_p)(\rho_p/\rho_n)}\right]^{-1} \tag{36}$$

Inserting this into Eq. (35), we obtain the minimum value of the product KR,

$$(KR)_{min} = \left[\sqrt{k_n\rho_n} + \sqrt{k_p\rho_p}\right]^2 \tag{37}$$

Inserting Eq. (37) into (32) gives the efficiency η' of a couple with optimized leg area fraction,

$$\eta' = \frac{(S\Delta T/V - 1)^{-1}}{\left[\frac{\sqrt{k_n\rho_n} + \sqrt{k_p\rho_p}}{S\Delta T - V}\right]^2 \Delta T + \frac{S_h T_h + S_c T_c + S\Delta T}{2(S\Delta T - V)} - \frac{1}{2}} \tag{38}$$

The preceding expression is maximized by setting the couple output voltage equal to

$$V_{opt} = S\Delta T \left[1 + \frac{1}{\sqrt{(1 + Z\overline{T})}}\right]^{-1} \tag{39}$$

where Z is the thermoelectric materials' temperature-averaged figure of merit, defined by

$$Z \equiv S^2 / \left[\sqrt{k_n\rho_n} + \sqrt{k_p\rho_p}\right]^2 \tag{40}$$

and $\overline{T}$ is an average temperature defined by

$$\overline{T} = (S_h T_h + S_c T_c)/2S \tag{41}$$

Inserting Eq. (41) into (38) gives the maximum efficiency η'' of a couple with optimized leg fraction α and optimized output voltage V,

$$\eta'' = \frac{\sqrt{(1 + Z\overline{T})}}{\frac{(\sqrt{(1 + Z\overline{T})} + 1)^2}{Z\overline{T}} \left(\frac{\overline{T}}{\Delta T}\right) + \left(\frac{1}{2} + \frac{\overline{T}}{\Delta T}\right)\left(\sqrt{(1 + Z\overline{T})} + 1\right) - \frac{1}{2}} \tag{42}$$

Eqs. (41) and (42) differ from previously published [15] forms because they include the effect of the Thomson coefficient. Note that in the special case when the temperature dependence of the Seebeck coefficient is negligible (i.e., $S_h = S_c = S$), the average temperature $\overline{T}$ from Eq. (41) reduces to the arithmetic mean temperature. Then, since the Carnot efficiency is given by

$$\eta_c \equiv \Delta T/T_h = \left[\overline{T}/\Delta T + 1/2\right]^{-1}, \tag{43}$$

the maximum efficiency η'' for that special case reduces to

$$\eta'' = \eta_c \left[1 + \frac{2 - \eta_c}{\sqrt{(1 + Z\overline{T})} - 1}\right]^{-1} \tag{44}$$

For the general case of temperature-dependent Seebeck coefficient and non-zero Thomson coefficient, Eqs. (39) through (42) show that the optimum couple voltage and maximum efficiency are functions of only the thermoelectric material properties and the operating temperatures. Figure 40 presents a semi-log plot of the voltage ratio $V_{opt}/S\Delta T$ as a function of $Z\overline{T}$, and Figure 41 presents a semi-log plot of η'' versus $Z\overline{T}$ for various values of $\overline{T}/\Delta T$. Figure 40 shows that the matched-load condition ($V=0.5\ S\Delta T$) does not yield the maximum efficiency. The greater the value of $Z\overline{T}$, the more the optimum deviates from matched load. Figure 41 shows the strong dependence of η'' on $Z\overline{T}$, which highlights the effectiveness of improvements in the material's figure of merit.

Figure 40. Effect of Figure of Merit Z and Temperature $\bar{T}$ on Optimum Load Voltage V_{opt}

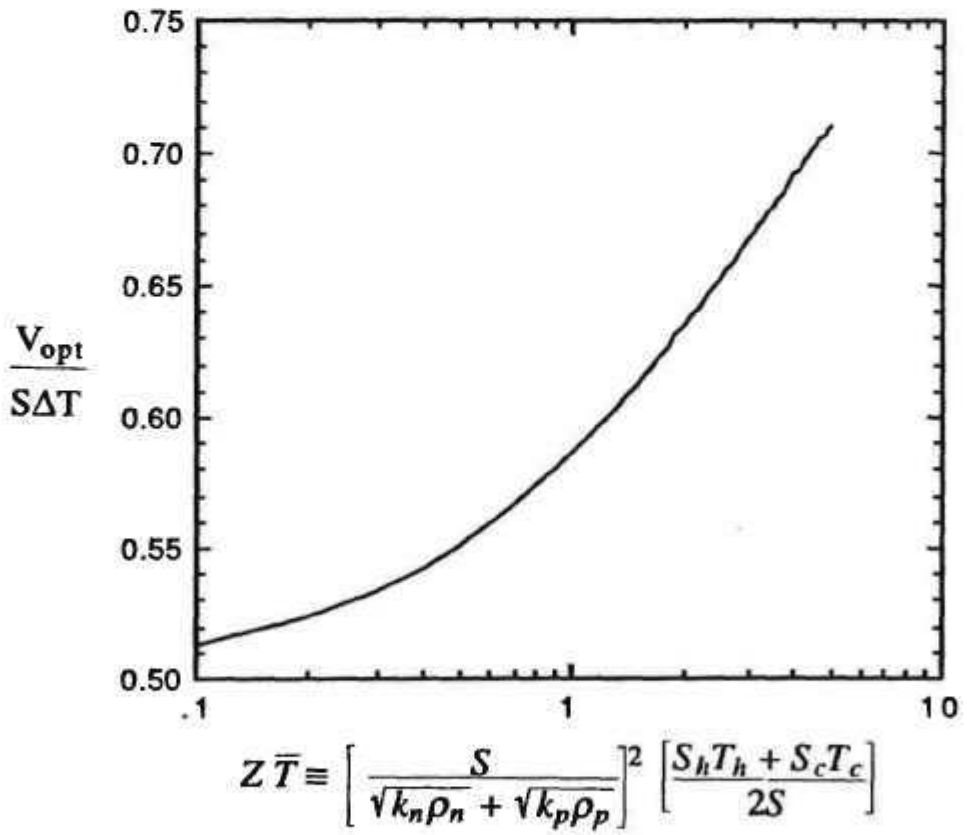

Figure 41. Effect of Figure of Merit Z and Temperature $\bar{T}$ on Maximum Couple Efficiency η''

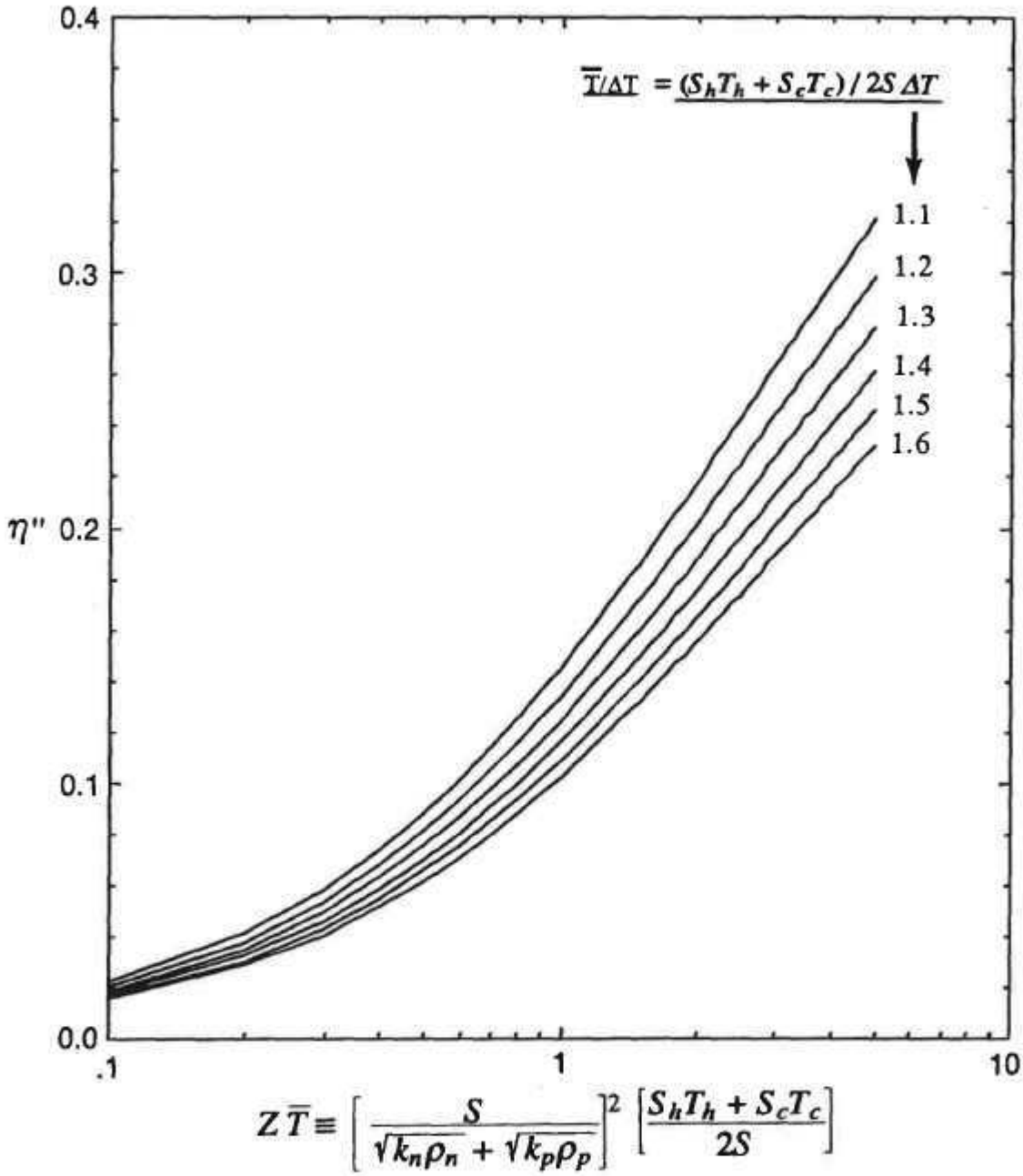

8.2.3 RTG Design Analysis: Consider now an RTG with N_m heat source modules, each having a heat generation rate Q_m. The RTG's power output P is given by

$$P = N_m Q_m \eta_t \eta'' (1 - \gamma) \quad , \tag{45}$$

where η_t is the RTG's thermal efficiency (i.e., the fraction of the generated heat delivered to the thermoelectric legs), η'' is the doubly-optimized couple efficiency given by Eq. (42), and γ is the fraction of the output voltage lost due to the electrical resistance of the inter-couple connectors and RTG terminals. The previous detailed analyses of the baseline RTG design yielded respective values of 0.88 and 0.06 for η_t and γ. To be consistent, those values were used throughout the material comparison studies.

Given a specified RTG power P, Eq. (45) can be solved for N_m, the number of heat source modules. But since N_m must be an integer, the RTG power goal can only be matched approximately. Alternatively, the power goal could be matched exactly, by deviating from the arbitrarily assumed cold-junction temperature T_c of 300°C (by adjusting the radiator fin dimensions).

The RTG has $N_p \times N_s$ thermoelectric couples, arranged in a network with N_p couples in parallel and N_s in series. For geometric reasons, N_p must of course be an integral divisor of the number of couples per ring. Given a specified RTG voltage, the number N_s of couples in series must satisfy the voltage balance

$$V_{RTG} = N_s V_{opt} (1 - \gamma) \quad , \tag{46}$$

where V_{opt} is the optimum couple voltage given by Eq. (39). Equation (46) can be solved for the integer value of N_s which comes closest to yielding the prescribed RTG voltage.

Finally, we must solve for the couple's length-to-area ratio which satisfies the RTG's heat balance

$$N_m Q_m \eta_t = N_p N_s Q_h \quad . \tag{47}$$

The heat input rate Q_h per couple is given by Eq. (21) in terms of its thermal conductance K, electrical resistance R, and current I. For the optimum leg area fraction α_{opt} (Eq. 36) and couple voltage V_{opt} (Eq. 39), the equations for K, R, and I (Eqs. 19, 20 and 29) can be reduced to

$$K = C_1(A/L) \quad , \tag{48}$$

$$R = C_2(L/A) \quad , \text{ and} \tag{49}$$

$$I = C_3(A/L) \quad , \tag{50}$$

where $$C_1 \equiv k_n \left[\frac{1 + \sqrt{(k_p/k_n)\,(\rho_p/\rho_n)}}{1 + \sqrt{(k_n/k_p)\,(\rho_n/\rho_p)}} \right] \tag{51}$$

$$C_2 \equiv \rho_n \left[1 + \sqrt{\frac{k_p \rho_p}{k_n \rho_n}} \right] \left[1 + \sqrt{\frac{k_n \rho_n}{k_p \rho_p}} \right] \quad , \tag{52}$$

and $$C_3 \equiv \frac{S \Delta T / C_2}{\sqrt{1 + Z \bar{T}} + 1} \quad . \tag{53}$$

Inserting Eqs. (47)through (50) into (21) and solving for L/A, we obtain the expression

$$L / A = \left[C_1 \Delta T + C_3 (S_h T_h + S_c T_c + S \Delta T)/2 - C_2 C_3^2/2 \right] N_p N_s / N_m Q_m \eta_t \tag{54}$$

for the required length-to-area ratio of the couples.

For each of the materials listed in Section 8.1, the preceding equations were solved for the RTG design parameters (N_m, N_p, N_s, α, and A) and for the resultant performance parameters (I, V, P, η'') and the RTG's mass and specific power. The computed results are presented in the next section.

8.3 COMPARATIVE PERFORMANCE

Comparison of the five RTG designs showed, not surprisingly, that Materials 2, 3, and 4 yielded very similar results. Therefore, only the results for Options 1, 3, and 5 are presented below. Table 11 compares their performance, and Table 12 compares their mass breakdown.

Table 12. Effect of Thermoelectric Figure of Merit on RTG Design and BOM Performance

Material:			
Material #	1	3	5
Designation	JPL 78/63	GE HYBRID	DREAM
BOM Figure Of Merit, K^{-1}	0.000584	0.000782	0.001387
RTG Design:			
Number of HS Modules	19	15	10
Thermal Power, watts	4640	3663	2442
RTG Height, inches	48.0	39.6	29.1
Number of Unicouple Rings	37	40	39
Unicouples per Ring	16	16	16
Number of Unicouples	592	640	624
Number in Parallel	4	4	4
Number in Series	148	160	156
Areas of TE Legs, cm^2	0.359	0.338	0.332
RTG Performance (BOM):			
Current, amp	9.30	9.13	9.08
Voltage	30.1	30.3	30.1
Power, watts	280	276	273
Couple Efficiency, %	7.26	9.08	13.48
System Efficiency, %	6.03	7.53	11.18
Estimated Mass, kg	61.6	50.9	37.7
Specific Power, w/kg	4.55	5.43	7.24

Comparison of columns 1 and 2 of Table 12 shows that the addition of GaP in the SiGe n-leg produces very significant efficiency increases. For the same output power, these lead to substantial reductions in fuel loading and RTG mass. But that addition would require modification of present material fabrication methods and bonding techniques, and extensive testing to demonstrate the couples' performance, reproducibility, compatibility with other RTG components at operating temperatures, and long-term performance stability.

Table 13. Effect of Thermoelectric Material on Mass of Unicouple RTG

RTG MASS BREAKDOWN (kg)	JPL 78/63 Z=0.000584	GE HYBRID Z=0.000796	DREAM Z=0.001387
HEAT SOURCE			
GPHS MODULES (19/15/10)			
FUEL (PuO_2)	11.32	8.94	5.96
CAPSULES (Ir)	4.44	3.51	2.34
GRAPHITICS	11.72	9.26	6.17
H.S. CANISTER (Mo)			
SIDE WALLS	2.23	1.84	1.23
BELLOWS	0.11	0.11	0.11
END CAPS AND LOAD SPREADERS	1.45	1.45	1.45
H.S.STRUCTURAL SUPPORTS			
GRAPHITE PRESSURE PLATES	0.52	0.52	0.52
LOAD STUDS+ZIRCONIA	0.27	0.27	0.27
BELLEVILLE SPRINGS (Ti)	2.64	1.22	0.35
OTHER PRELOAD HARDWARE	0.84	0.84	0.84
CONVERTER			
ELECTRICAL CIRCUITS			
TE ELEMENTS (592/640/624)	5.63	5.47	4.82
TE FASTENERS AND SEALS	1.12	1.21	1.18
ALUMINA INSULATORS	0.90	0.98	0.95
ELECTR. CONNECTORS+TERMINALS	0.35	0.38	0.37
MULTIFOIL INSULATION (Mo/Quartz)			
SIDES	5.53	4.43	3.62
ENDS	0.68	0.68	0.68
RTG HOUSING (Al)			
SIDE WALL (.090"/.085"/.060")	6.82	5.28	3.01
END SECTION	0.47	0.47	0.47
COVERS	0.98	0.98	0.98
RESISTANCE THERMOMETER	0.30	0.30	0.30
GAS MGMT. ASSEMBLY	0.16	0.16	0.16
RADIATOR			
FINS (8/4)	2.67	2.16	1.55
AUXILIARY COOLANT MANIFOLDS	0.25	0.25	0.25
EMISSIVITY COATING	0.15	0.15	0.15
TOTAL MASS(kg)	61.55	50.86	37.73

Comparison of columns 2 and 3 of Tables 12 and 13 shows that the hypothetical and still undefined "dream" material would result in even greater efficiency increases, and correspondingly much larger reductions in fuel loading and RTG mass. But this would require successful and timely completion of a major new development program that is still largely undefined. The authors are therefore unable to assess the ultimate success probability of such a program. But, based on their extensive experience on numerous other RTG development programs, they are convinced that a program to develop a flight RTG employing this material would not come close to meeting the JPL-envisaged MRSR schedule described in Figure 2.

Multicouples employing SiGe/GaP n-legs have already been built and tested for 6000 hours. They exhibited stable performance under positive bias, but anomalous degradation under negative bias with respect to the RTG housing. The cause of the negative-bias problem has now been identified and, if correct, should be easily avoidable. But extended lifetests are still required to demonstrate the long-term performance stability of multicouples under both positive and negative bias conditions. Such life tests are necessarily time-consuming, and may not be completable in time for the projected program schedule. But even if that were the case, Table 13 shows that the use of SiGe/GaP n-legs in RTGs, even with standard-length unicouples, would still be quite advantageous. Such unicouples have not yet been qualified, and would require significant new bond developments. But the programmatic risk of doing that seems reasonable and well justified by the potential payoff.

The above discussion pertains to this specific section. The overall results and conclusions derived from the study are summarized in the next section.

9.0 RESULTS AND CONCLUSIONS

The computed results of the various analyses are summarized below, and the resultant conclusions are listed on the next three pages.

RTG Type	Baseline RTG				Short RTG		Doped RTG	Short UC RTG	MC RTG	
TE Element	UC				UC		UC	UC	MC	
P-Leg Material	SiGe				SiGe		SiGe	SiGe	SiGe	
N-Leg Material	SiGe				SiGe		SiGe/GaP	SiGe/GaP	SiGe/GaP	
Leg Length, in	0.8				0.8		0.8	0.4	0.3	
Couples per TE Element	1				1		1	1	20	
Leg Area, sq. in.	0.0527				0.0494		0.0645	0.0627	0.0979	
TE Couple Figure of Merit, 0.001/K	0.58				0.58		0.72	0.72	0.72	
Number of H. S. Modules per RTG	18				9		18	18	16	
Number of TE Rings per RTG	36				18		36	26	16	
Number of TE Elements per Ring	16				16		16	12	8	
Number of TE Elements per RTG	576				288		576	312	128	
Number in Parallel	4				2		4	2	16	
Number in Series	144				144		144	156	8	
RTG Length, in	45.9				26.7		45.9	45.9	41.6	
RTG Housing Diameter, in	9.1				9.1		9.1	9.1	7.5	
RTG Housing Thickness, in	0.09				0.06		0.09	0.09	0.0625	
Number of Fins	8				8		8	6	4	
Fin Root Thickness, in	0.06				0.06		0.06	0.08	0.10	
Fin Length, in	3				3		3	4	5.5	
Mass Breakdown, kg										
GPHS Modules	26.05				13.03		26.05	26.05	23.16	
H. S. Canister	3.77				2.38		3.77	3.77	3.52	
H. S. Structural Support	3.94				2.18		3.94	3.94	2.59	
Electrical Circuits	7.74				3.96		7.74	5.98	2.84	
Multifoil Insulation	5.94				3.31		5.94	3.11	4.03	
RTG Housing	8.45				4.52		8.45	7.44	6.78	
Radiator	2.78				1.78		2.78	2.78	2.33	
Total Mass per RTG	58.67				31.15		58.67	53.07	45.25	
Mission Time, BOM/EOM	BOM	BOM	BOM	EOM	BOM	EOM	BOM	BOM	BOM	EOM
Thermal Power, W	4396	4396	4396	4261	2198	2131	4396	4396	3907	3787
Cooling Mode, Convective/Radiative	C	R	R	R	R	R	R	R	R	R
Martian Ground Temperature, K	-	140	300	300	300	300	300	300	300	300
Maximum Temperature, °C										
Fuel Clad	1091	1168	1175	1159	1174	1157	1173	1196	1159	1141
H. S. Surface	994	1082	1090	1073	1088	1071	1088	1114	1071	1053
Canister	959	1054	1061	1045	1060	1043	1059	1087	1041	1024
TE Hot Junction	890	991	999	984	1000	985	997	996	992	974
TE Cold Junction	156	281	291	287	278	274	290	312	316	311
Fin Root	116	252	261	258	246	242	260	257	259	256
Fin Tip	101	214	224	221	210	208	223	210	184	182
Efficiency, %										
Material	8.05	7.93	7.91	7.43	8.13	7.64	8.72	8.47	8.41	7.96
Couple	7.72	7.72	7.70	7.23	7.92	7.43	8.28	7.89	8.02	7.59
Converter	6.67	6.62	6.60	6.22	6.75	6.36	7.04	6.69	7.15	6.76
System	6.57	6.48	6.44	6.08	6.42	6.05	6.89	6.55	6.86	6.50
RTG Output										
Current, A	9.63	9.49	9.43	8.64	4.71	4.30	10.09	9.60	9.10	8.34
Voltage, V	30.0	30.0	30.0	30.0	30.0	30.0	30.0	30.0	29.5	29.5
Power, W	289	285	283	259	141	129	303	288	268	246
Specific Power, W/kg	4.93	4.86	4.82	4.41	4.53	4.14	5.16	5.42	5.92	5.44

1. The current multifoil-insulated GPHS-RTG and Mod-RTG designs can be modified to operate in an environment with an external atmosphere (e.g., Mars).

2. The helium generated by the fuel's alpha decay can be vented to the outside without intrusion of the external atmosphere into the RTG.

3. The use of novel selective vents and unproven high-capacity getters is not required.

4. The Rover RTGs can be built from standard and proven General Purpose Heat Source modules and standard SiGe unicouples or SiGe/GaP multicouples, using demonstrated thermoelectric material performance parameters.

5. The modular heat source stack in the Rover RTG is held together by axial load springs, without the use of mid-span supports.

6. The springs will support and hold the heat source together under transverse loads of 25 G in the water-cooled RTG during Earth launch and Mars entry and 15 G in the radiation-cooled RTG during subsequent Mars operations, without exceeding the allowable stresses in the springs, the heat source, or the RTG housing.

7. In case of inadvertent reentry into the Earth's atmosphere, the RTG's aluminum housing will burn off, allowing the heat source modules to separate and impact at a relatively low velocity.

8. An auxiliary cooling loop (e.g., water and antifreeze) will be required to cool the RTG while it is within the Rover's aeroshell during launch and transit to Mars.

9. The RTGs are mounted on the Rover in a vertical orientation, to avoid the buildup of wind-borne Martian sand on its heat rejection surfaces.

10. The ~250-watt baseline RTG containing 18 heat source modules and employing 576 standard unicouples has a mass of 58.7 kg, a length of 45.9 inches, a housing diameter of 9.1 inches, and a tip-to-tip radiator span of 15.2 inches.

11. At the beginning and end of the four-year mission on Mars, the baseline RTG has respective power outputs of 283 and 259 watts, system efficiencies of 6.44 and 6.08%, and specific powers of 4.82 and 4.41 watt/kg.

12. The RTG can deliver full operating power during its water-cooled cruise to Mars.

13. The power output of the radiatively cooled RTG is essentially independent of the Martian temperature.

14. The combined effect of fuel decay and thermoelectric material degradation during the four-year mission reduces the power output by 8%.

15. Rover's 500-watt power requirement can be satisfied with two 250-watt or four 125-watt RTGs, with respective lengths of 45.9 and 26.7 inches. Both sizes appear to be compatible with currently envisaged Rover designs.

16. The mass of four 125-watt RTGs is 6% higher than that of two 250-watt RTGs. This disadvantage may be offset by their greater ease of integration with the spacecraft, and by the fact that - with four independent RTGs - failure of one would still permit continuing mission operation at 75% power.

17. Basic designs have been prepared for both unicouple RTGs and multicouples RTGs. These designs apply both to current TE elements and to elements of advanced designs and materials.

18. If unicouples with SiGe/GaP legs were developed, they would raise the specific power of the RTG by 9.1% above that of the SiGe baseline design.

19. For the same thermoelectric material (SiGe/GaP) and the same thermal power, an RTG using short unicouples is 9.5% lighter than one using standard unicouples; but because of its doubled heat flux and current density and its resultant higher thermal and electrical contact losses, it produces 5.0% less power.

20. Because of their lower efficiency, short unicouples offer only a 5.0% specific-power improvement over standard-size unicouples.

21. A 250-watt RTG using standard SiGe/GaP multicouples is 23% lighter, 9.4% shorter, and 7% more efficient than the baseline RTG using standard SiGe unicouples.

22. If and when advanced thermoelectric materials with much higher figures of merit become available, the RTGs' fuel loading and mass can be significantly reduced. As a highly optimistic example, if a standard-size unicouple with a figure of merit of $0.00140K^{-1}$ were developed, it would reduce the baseline RTG's fuel loading by 46% and its mass by 37%.

The ultimate design and material selections will represent a trade-off between minimizing the RTG mass to help meet the Rover system design goals and minimizing the need for new technology to reduce the development cost and time and the programmatic risks.

10.0 REFERENCES

[1] Statement before the Committee on Energy and Natural Resources, United States Senate by Dr. Robert Rosen, Sept. 13, 1988.

[2] J.D. Bourke, J.H. Kwok, A. Friedlander, "Mars Rover Sample Return Mission." AIAA-89-0417, 27th Aerospace Science Meeting January 9-12, 1989, Reno, Nevada.

[3] J.R. Casani and M.S. Reid, "JPL and Mars Exploration." 39th Congress of the International Astronautical Federation, held in Bangalore, India, 10-14 October 1988.

[4] G.L. Bennett, J.J. Lombardo and B.J. Rock, "Development and Use of Nuclear Power Sources for Space Applications." Journal of the Astronautical Sciences, Vol. XXXIX, Dec. 1981.

[5] J.T. Rose, "Conceptual Design of the Mars Rover Sample Return System." AIAA-89-0418, 27th Aerospace Science Meeting, January 9-12, 1989, Reno, Nevada.

[6] J. Randolph, "Mars Rover Sample Return Orbiter Design Concepts." AIAA-89-0421, 27th Aerospace Science Meeting, January 9-12, 1989, Reno, Nevada.

[7] T. Gamberk, L. Rogers, "Aerocapture, Entry and Landing Systems for the Mars Rover Sample Return." AIAA-89-0422, 27th Aerospace Science Meeting, January 9-12, 1989, Reno, Nevada.

[8] D. Pivirotto, T. Penn, W.C. Dias, "Mars Rover 1988 Concepts." AIAA-89-0419, 27th Aerospace Science Meeting, January 9-12, 1989, Reno, Nevada.

[9] "Mars Rover, Phase-1 Design Data Book", edited by B.K. Muirhead, Jet Propulsion Laboratory, April 23, 1988.

[10] "Environment of Mars, 1988", Jet Propulsion Laboratory, TM100470, Oct. 1988.

[11] A. Schock, "Design Evolution and Verification of the General Purpose Heat Source." Proceedings of the 1980 Intersociety Energy Conversion Engineering Conference, Volume 2, pages 1032-1042.

[12] G. Bennett, et al, "Update to the Safety Program for the General Purpose Heat Source Radioisotope Thermoelectric Generator for the Galileo and Ulysses Missions." Transactions of the Sixth Symposium on Space Nuclear Power Systems, Albuquerque, New Mexico, 8-12 January 1989.

[13] A. Schock and A. Shostak. "Use of Modular Heat Source Stack in RTGs." Proceedings of the 1979 Intersociety Energy Conversion Engineering Conference, Boston, MA.

[14] A. Hall Jr., A. Holowenko, and H. Laughlin, "Schaum's Outline of Theory and Problems of Machine Design." New York: McGraw-Hill Book Company, 1980.

[15] A.F. Ioffe, Semiconductor Thermoelements and Thermoelectric Cooling, Infosearch, London (1957).

[16] V. Raag, Thermo Electron Corporation, Waltham, Mass., Private Communication.

[17] A. Schock, "Modular Isotopic Thermoelectric Generator." Proceedings of the 1981 Intersociety Energy Conversion Engineering Conference, Volume 1, pages 327-342.

[18] A. Schock, "Revised MITG Design, Fabrication Procedure, and Performance Predictions." Proceedings of the 1983 Intersociety Energy Conversion Engineering Conference, Volume 3.